LABORATOIRE DE MECANIQUE, MATERIAUX ET STRUCTURES

LABORATORY OF MECHANICS, MATERIALS AND STRUCTURES

Piezoelectric based structures powered by nonlinear electrical circuits: characterization, dynamical states and applications

Thesis submitted and defended in partial fulfillment of the requirements for the awards of a Doctor of Philosophy (Ph.D) degree in Physics

Specialty: Fundamental Mechanics and Complex Systems

By

MBOU SOH Guy Bertrand

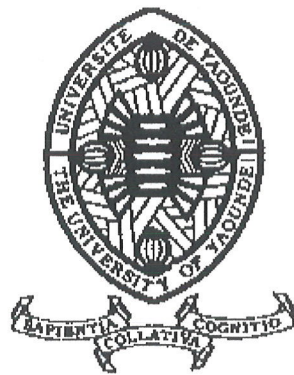Registration Number: **10W0463**

Master of Science in Physics

Under the supervision of

WOAFO Paul

Professor

© **Year 2022**

DÉPARTEMENT DE PHYSIQUE
DEPARTMENT OF PHYSICS

ATTESTATION DE CORRECTION DE LA THÈSE DE DOCTORAT/Ph.D

Nous, Professeur **NANA NBENJO Blaise Roméo** et Professeur **ESSIMBI ZOBO Bernard**, respectivement Examinateur et Président du jury de la Thèse de Doctorat/Ph.D de Monsieur **MBOU SOH Guy Bertrand**, Matricule 10W0463, préparée sous la supervision du Professeur **WOAFO Paul**, intitulée : « **PIEZOELECTRIC BASED STRUCTURES POWERED BY NONLINEAR ELECTRICAL CIRCUITS : CHARACTERIZATION, DYNAMICAL STATES AND APPLICTIONS** », soutenue le Mercredi, **06 Juillet 2022**, en vue de l'obtention du grade de Docteur/Ph.D en Physique, Spécialité **Mécanique, Matériaux et Structures**, Option **Mécanique Fondamentale et Systèmes Complexes**, attestons que toutes les corrections demandées par le jury de soutenance ont été effectuées.

En foi de quoi, la présente attestation lui est délivrée pour servir et valoir ce que de droit.

Fait à Yaoundé, le ...1 8 JUL 2022.....

Examinateur	Le Président du jury	Le Chef de Département de Physique
Pr. NANA NBENJO Blaise Roméo	Pr. ESSIMBI ZOBO Bernard	Pr. NDJAKA Jean-Marie

Dedications

- ✓ To the Lord GOD Almighty, the creator of the universe who by his will granted me the grace to complete this work.

- ✓ To my late dad SOH François, for his support and all the strength that only you knew how give me. May your soul rest in peace dad.

- ✓ To my late mother KAMDZÉ Elisabeth. May your soul rest in peace mom

Acknowledgements

At the moment where this thesis ends, it is a pleasure for me to express my deepest gratitude to all those have contributed to its realization. I thing notably to:

Professor WOAFO Paul, my supervisor for the trust, relationship, guidance and support during the years of my graduate studies. Professor, from my works of Master up to now, you have grown in me good qualities (humanistic, entrepreneurship and scientific) which, I hope, will make me a great man. Thanks one more.

The late **Dr. MBOUSSI NKOMIDIO Aïssatou**. Thank you for the welcome, advice, precision and initiation you were able to instill in us. May the land of our ancestors be light for you.

Professor NDJAKA Jean-Marie Bienvenu, Head of Department of Physics, Faculty of Science, UYI and the teaching staff of this department for their valuable teaching and their fruitful advices.

Professor KOFANE Timoléon Crépin whose impulse to nonlinear physics in Cameroon for the last three decades has been too beneficial to me.

I acknowledge the scientists for accepting to examine this thesis: the President of jury Professor **ESSIMBI ZOBO Bernard** of University of Yaoundé 1; the members of jury namely Professors **NANA NBENDJO Blaise Roméo**, Professors **DJUIDJE KENMOE Germaine**, Professor **FEWO Serge Ibraïd** of University of Yaoundé 1 and Professor **FOTSIN Hilaire Bertrand** of University of Dschang.

Dr. NWAGOUM Tuwa Peguy Roussel for his fruitful interactions and discussions during my thesis.

Centre of Research and Doctoral training unit for Physics and Applications, which gave me the opportunity to benefit for this doctoral training.

Mrs. KOUAMI Nadine for his sincerity, his advices and our informative discussions.

Professor TAKOUGANG KINGNI Sifeu, for interesting exchanges on this thesis.

Contents

List of Figures

List of Tables

List of Abbreviations

AC: **A**lternative **C**urrent

DARPA: **D**efense **A**dvanced **R**esearch **P**rojects **A**gency

DC: **D**irect **C**urrent

Etc.: **E**t **c**ætera

EXACTO: **E**xtreme **A**ccuracy **T**asked **O**rdinance

FEM: **F**inite **E**lement **M**ethod

FORTRAN: Formula Translator

H-R: **H**indmarh-**R**ose

LFG: **L**ow **F**requency **G**enerator

MATLAB: Matrix Laboratory

MEMS: **M**icro **E**lectromechanical **S**ystems

MRC: **M**axwell **R**esistive **C**apacitor

NLR: **N**onlinear **R**esistance

NLC: **N**onlinear **C**apacitor

ODEs: **O**rdinary **D**ifferential **E**quations

OP-AMP: **O**perational **A**mplifier

PDEs: **P**artial **D**ifferential **E**quations

PEH: **P**iezoelectric **E**nergy **H**arvester

PZT: **P**lomb-**Z**irconate **T**itanate

RK: **R**unge-**K**utta

Abstract

This thesis deals with the experimental and theoretical characterization of piezoelectric structures and their use as component in nonlinear electronic circuits for actuation, medicine and energy harvesting. In each case the physical systems, their detailed description and their mathematical models are discussed. The appropriate mathematical formalisms (modal approximation, Harmonic balance method, Lyapunov exponent and Routh-Hurwitz criterion) and numerical methods are used to investigate the dynamics of proposed systems. The following main results are obtained:

  ✓ An experimental frequency-impedance curve of the piezoelectric plate is obtained leading to the electric equivalent of the piezoelectric plate constituted of a capacitive branch in parallel with many RLC resonant branches. Vibration modes of the plate are used to justify qualitatively the resonant frequencies of the experimental curve. This result is confirmed by the direct numerical simulation of the coupled differential equations modeling the piezoelectric plate. Theoretical and experimental analyses show that a circuit consisting of a piezoelectric plate in series with a resistor presenting a nonlinear $I-V$ characteristics having a negative slope exhibits autonomous oscillations of the Van der Pol type.

  ✓ The dynamical behavior of a piezoelectric beam powered by two types of nonlinearity is considered: nonlinear dependence of the voltage on electrical charge and nonlinear dependence of the inductance on current. The dynamical behaviors are characterized showing jump phenomena, amplitude jump phenomena and chaotic states. One proposes a model for the production of periodic patterns of pulse oscillations. For each case, hints of applications for actuations and medical devices are discussed.

  ✓ Submitted to fluid flow, mechanical structures can undergo self-sustained oscillations. This principle is used for an energy harvester system made of micro-beams with piezoelectric layers. The dynamical behavior of the harvester is analyzed and the electric power is plotted versus the fluid velocity, fluid force coefficient, frequency and load resistance. It was found that the time variation of the voltage and current displayed periodic behavior with sharp peaks and chaotic shapes.

Keywords: *Piezoelectric plate, Characterization, self-sustained oscillator, chaos, Electric equivalent, pulse ultrasounds behavior, actuators, nebulizer, echography, piezoelectric energy harvester.*

Résumé

Cette thèse traite la caractérisation expérimentale et théorique des structures piézoélectriques et leurs utilisations comme composant dans des circuits électroniques non linéaire pour l'actionnement, la médecine et la récupération d'énergie. Dans chaque cas, les systèmes physiques, leur description détaillée et leur modèle mathématique sont présentés. Les formalismes mathématiques appropriés (approximation modale, exposant de Lyapunov et critère de Routh-Hurwitz) et des méthodes numériques sont utilisés pour étudier la dynamique des systèmes proposés. Les principaux résultats suivants sont obtenus.

✓ Expérimentalement, la caractéristique fréquence-impédance de la plaque piézoélectrique conduisant à l'équivalent électrique de la plaque piézoélectrique constituée d'une branche capacitive en parallèle avec de nombreuses branches résonantes RLC est obtenue. Les modes de vibrations de la plaque sont utilisés pour justifier qualitativement les fréquences de résonnances obtenues expérimentalement ; chacune ayant sa propre fréquence de résonance. Ce résultat est confirmé par la simulation numérique directe du modèle d'équations différentielles couplés associé à la plaque piézoélectrique. Une étude théorique et expérimentale montrant que la mise en série de la plaque piézoélectrique avec une résistance présentant une caractéristique I - V non linéaire à pente négative, exhibe des oscillations autonomes de type Van der Pol est faite.

✓ Le comportement dynamique d'une poutre piézoélectrique excitée par deux types de non-linéarité est considéré: la dépendance non linéaire de la tension à la charge électrique et la dépendance non linéaire de l'inductance au courant. Les comportements dynamiques sont caractérisés par des phénomènes de sauts d'amplitude et des états chaotiques. Un modèle pour la production des salves d'impulsions périodiques est proposé. Pour chaque cas, des indications d'applications en actionnements et médecine sont discutés.

✓ Soumises à l'écoulement des fluides, les structures mécaniques peuvent subir des oscillations auto-entretenues. Ce principe est utilisé pour un système de récupération d'énergie constitué de micro poutre à couches piézoélectriques. Le comportement dynamique du récupérateur d'énergie est analysé et la puissance électrique est tracée en fonction de la vitesse du fluide, du coefficient de force du fluide, de la fréquence et de la résistance de charge. Il est constaté que la variation temporelle de la tension et du courant présente un comportement périodique avec des pics pointus et des formes chaotiques.

Mots clés: *Plaques piézoélectriques, Caractérisation, Oscillateurs auto entretenus, chaos, Salves d'ultrasons, actionneur, nébuliseur, échographie, Récupérateur d'énergie piézoélectrique.*

General introduction

Piezoelectric materials belong to the multifunctional materials which have the ability to generate an electric potential in response to applied mechanical stress [1]. The piezoelectric effect was discovered by Curie in 1880 [2]. Since the piezoelectric effect is reversible, materials those demonstrate the direct piezoelectric effect, which is the generation of electricity upon applied mechanical stress but, also demonstrate the converse piezoelectric effect, which is the generation of stress and strain as response to electric field [3]. In 1881, Lippman showed the existence of the indirect effect [4], which was experimentally highlighted by the Curie brothers the following year [2]. In 1910, Voigt published a rigorous study of the asymmetric crystal classes and their piezoelectric properties [5]. However, there are different types of piezoelectric materials, and some representative materials include quartz and Lead-Zirconate Titanate (PZT), which are a natural crystal and a man-made ceramic, respectively. Piezoelectric plates can be used as sensors and actuators, sounds transducers, medical tools and energy harvesters [6-9]. To design system with piezoelectric component, it is necessary to select not only a kind of piezoelectric material with required parameters, but also geometrical parameters of the transducer. Selecting all parameters of system it is possible to obtain required characteristics that describe its behavior and to obtain the maximum efficiency of the system's operation. A condition that is necessary to design such kind of systems correctly is their precise description by an appropriate mathematical model that includes relations between all parameters of the system and also allows designing its characteristics, including influence of all parameters [10-13].

Silent and harmless to the body, a wide variety of ultrasounds are generated by the reverse piezoelectric effect [14]. In fact, over the past 80 years, ultrasound devices have become important diagnostic tools both for biological, chemical and physical bodies. Their potential as a leader in medical diagnostic imaging was recognized since the 1930s and 1940s, when Dussik and his brother Friederich attempted to use ultrasound to diagnose brain tumors [15]. Monitored by appropriate electrical signals, the piezoelectric beams or plates of different sizes can also be used as actuators for several technological devices such as loudspeakers, motors of different types, mirror positioners, acousto-optic modulators, inkjet printers, fuel injectors, vibration controllers, and so on. Their motion can be tuned for a single action or can lead to periodic actions (periodic actuation mechanisms). Because of this large number of applications, research investigations have been engaged in order to sort new and special motions which can be exhibited by piezoelectric beams (or plates). **One of the objectives of this thesis is to present the dynamical behavior of a piezoelectric beam powered by some special nonlinear electronic circuits.**

In this thesis, three types of electric circuits are used: an electrical circuit having nonlinear capacitance, an electronic circuit with nonlinear characteristics in the flux-current relation, and an electronic circuit mimicking a biological oscillator (the Hindmarsh-Rose oscillator). An external sinusoidal voltage source is used in the case of the first two electrical circuits and in the third case, there is no external periodic source of energy, making the system self-oscillating. The main dynamical behaviors will be linked to applications in the actuation fields and in medical fields: nebulizers [16-19] and echography analysis [20-27].

After the study of the piezoelectric beam for actuations purpose and for medical device, we use it in an energy harvester with self-sustained behavior. As showed in [28-32], a range of vibration energy harvesting devices have been proposed. Energy harvesters transform available ambient energy into electrical energy through various mechanisms [33-55]. This is an important source of energy for small electronic devices and for small batteries to enable remote operation [56]. Experiments by Simiu et al. [57], based on the Battista's work [58], showed that vibration of bridge exhibits the typical dynamic behavior of a self-excited oscillator due to a fluid-induced forcing function. The presentation given in this thesis follows an extension of this model to energy harvesting. Self-excited oscillators are used in many areas of scientific works [59-61]. Recently, Clair et al. in [35] proposed a concept for a micro power generator that uses self-excited limit cycle's oscillations of a piezoelectric beam, to harness wind energy and maintain low power consumption devices.

As indicated above, the thesis concentrates on the following objectives:

➢ **Experimental characterization of a piezoelectric plate and use of vibrations modes and parallel resonant branches in the electric equivalent model to justify the behavior of the piezoelectric plate,**

➢ **Study of a piezoelectric plate based self-excited electronic oscillator and actuator,**

➢ **Analysis of the dynamical behaviors of a piezoelectric beam powered by a nonlinear electrical circuits and self- sustained electronic oscillator and links to nebulizer and echography,**

➢ **Study of a model of self-sustained piezoelectric energy harvester under fluid flow.**

The present work is divided in three chapters.

In chapter one, one firstly gives to the readers the information on piezoelectricity and piezoelectric structures, characterization of piezoelectric structures, applications of piezoelectricity and secondly, one redefines clearly the problem solved in the thesis.

Chapter two presents the methodology for the experimental and theoretical characterization of a piezoelectric structure, the mathematical formalisms, the numerical methods and the experimental procedure based on analog circuits, used to solve the problems of this thesis.

Chapter three deals with the presentation of the main results of the thesis.

The general conclusion ends the thesis with a summary of the main results and indications of perspectives for future works.

Chapter 1: Literature review

1.1 Introduction

The goal of this chapter is to give firstly the information about piezoelectricity and piezoelectric structure, characterization of piezoelectric structures, applications of piezoelectricity and secondly, to expose the work to be carried out in this thesis. Section 1.2 is devoted to the generalities on the piezoelectricity. In section 1.3, nonlinearities in electromechanical systems are presented. Section 1.4, is devoted to the recent investigations on nonlinear piezoelectric structures. Section 1.5 will give more details on the problems to be solved in this thesis and in section 1.6 will conclude the chapter.

1.2 Generalities on the piezoelectricity

1.2.1   Definition of the piezoelectricity

Any material that develops an electric charge or polarity on the application of an external mechanical stress, or vice versa is known as a piezoelectric material. The phenomenon of generation of the electrical charges in response to an external mechanical stress is known as the direct piezoelectric effect. Conversely, the phenomenon in which mechanical deformation occurs due to the application of an electric field is known as the reverse, or indirect, piezoelectric effect.

Figure 1 illustrates both the direct and indirect piezoelectric effect. Figure 1(a) shows the poling axis in a piezoelectric material. The poling axis of a piezoelectric material determines the polarity of the material under stress. The axis is defined during a polarization step during the manufacture of the material (see subsection 1.2.2).
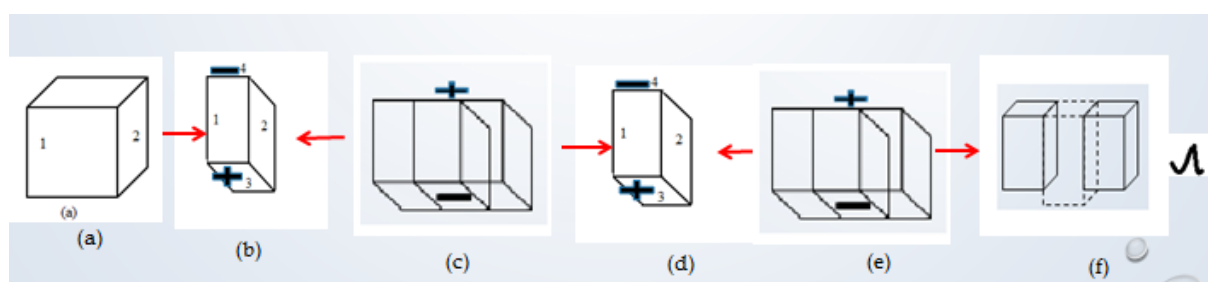
Figure 1: Example of the piezoelectric effect

As shown in Figure 1(b), if the material is compressed, a voltage of the same polarity (as the poling axis) appears between the electrodes. If stretched, a voltage of opposite polarity appears (see Figure 1(c)). Conversely, if a voltage is applied, the piezoelectric material will deform. A voltage with opposite polarity as the poling axis will cause the material to expand (shown in Figure 1(d)). A voltage with the same polarity will cause the material to compress,

as depicted in Figure 1(e). If an AC signal is applied, as shown in Figure 1(f), the material will vibrate at the same frequency as the signal.

1.2.2 Piezoelectric structures (beam, plates, circular and others)

The piezoelectric materials available in the market can be classified into two classes: crystal and ceramic. Ceramic is an artificial piezoelectric material. It is a preferred piezoelectric material because of the ease with which it can be manufactured into a variety of shapes (beam, plate, circular and others) and sizes. The most commonly produced piezoelectric ceramics are PZT, Barium Titanate and Lead Titanate. Their manufacturing cycle by solid route is illustrated in Figure 2. They do not become piezoelectric until after the final step of polarization which consists in the application of a continuous electric field of high value in order to orient the different polarization vectors in the same direction.
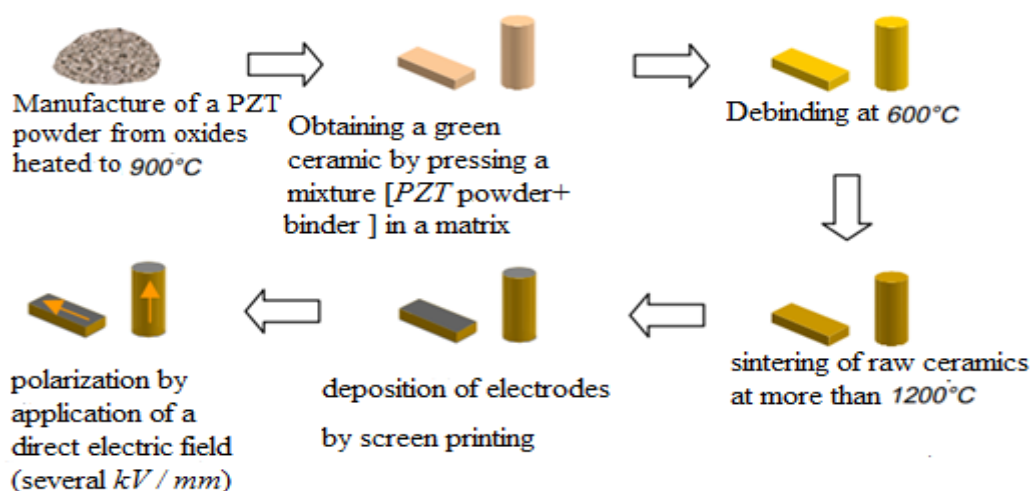
Figure 2: Manufacturing cycle of PZT ceramics by solid process [6,9]

1.2.3 Characterization of the piezoelectric structures

A powerful motivation for using equivalent circuits to characterize piezoelectric devices is that the equipment is often itself completely electrical in nature. The whole ensemble thus becomes subject to analysis or synthesis from a single perspective; etc., network theory. In this subsection, we describe a brief history of equivalents circuits.

Mechanical analogs were considered necessary in the last century for visualizing electromagnetic phenomena. The situation was reversed in 1914 when Butterworth first used an equivalent electrical circuit to represent a mechanically vibrating system. This was followed by Van Dyke's independent discovery in 1925 that the same circuit characterized the impedance behavior of a piezoelectric resonator.

The electric equivalent of the piezoelectric plate proposed by Van Dyke and recommended by the IEEE Standard on Piezoelectricity [62] is represented in Figure 3.
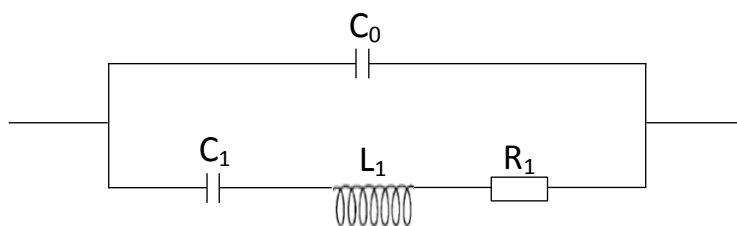
Figure 3: Van Dyke's model for a piezoelectric element, were C_0 and C_1 are the capacitances, L_1 the inductor and R_1 the resistor.

Subsequently, Mason introduced in the 1930s [63], acoustic transmission lines, mechanical ports, and piezoelectric transformers, thereby extending the circuit to encompass electromechanical conversion devices of wide generality. Today, the Mason equivalent circuit is universally used for bulk and surface acoustic wave device characterizations. It has also given rise to a variety of alternative formulations such as analog networks and systems models.

The use of equivalent electrical networks to represent mechanical systems is pervasive today, particularly with respect to the depiction of piezoelectric resonators and transducers. This is a complete reversal of the situation existing less than one hundred years ago. One has only to read the works of Maxwell [64] and Kelvin [65] to see how mechanical explanations were sought for electrical phenomena. Other analogies are treated in references [66] and [67], where their contributions have been pervasive in the area of equivalent circuits of bulk and surface wave resonators and transducers.

1.2.4 Applications of the piezoelectricity

Cell phones, diesel fuel injectors, acoustic guitar pickups, grill igniters, ultrasonic transducers, vibration sensors, certain printers, and musical greeting cards (Figure 4) all have in common, besides being electronic devices, piezoelectricity in some way.

Figure 4: Top applications of piezoelectric materials in day to day life [3,6]

1.2.3.1   *Piezoelectric Sensors in Industrial Applications*

The industrial sector often employs piezoelectric sensors for a variety of uses. Some common, uses include:

- **Pressure Sensors (Figure 4(a)):** In nearly any application requiring the measurement of dynamic pressure changes, using piezoelectric pressure sensors yields more reliable results than using conventional electromechanical pressure sensors. This is because piezoelectric devices have a high frequency response and signal conversion without requiring any bellows, diaphragm, or any type of mechanical linkage in conjunction with a strain gage or displacement sensor.

- **Sonar Equipment (Figure 4(b)):** Depth sounders and sonar equipment rely extensively on piezoelectric sensors to transmit and receive ultrasonic "pings" in the 50-200kHz range. Besides having an ideal frequency response for such applications, piezoelectric transducers have a high power density that enables large amounts of acoustic power to be transmitted from a small package. For instance, a transducer that is only 4" (100 mm) in diameter may be capable of handling power output greater than 500 W.

1.2.3.2   *Uses of Piezoelectric Actuators in Industrial Applications*

While piezoelectric sensors are highly valuable to the industrial sector, the industry also makes use of piezoelectric actuators for a variety of applications:

- **Diesel Fuel Injectors (Figure 4(c)):** In the last decade, regulations on emissions from diesel engines have become increasingly stringent. Additionally, customers continue to demand quieter engines with improved power and torque curves. In

order to meet these, engine manufacturers have resorted to using precisely timed and metered injections of fuel during the combustion process. This is the case of a single fuel injector may switch fuel flow with pressures exceeding 26,000 psi (1800 bar) on and off several times in rapid succession during a single power stroke. Such precise control of high-pressure fluid is made possible by using piezoelectric actuators controlling small valves within fuel injectors.

1.2.3.3   Piezoelectric Actuators in Consumer Electronics

Piezoelectric actuators are used in consumer electronics.

- **Piezoelectric Printers 4(d):** There are two main types of printers that use piezoelectric actuators;

  - *a dot-matrix printer :* In a piezoelectric dot matrix printer, piezoelectric actuators in the printer head move needle-like pins through a strip of ink tape (similar to a typewriter) against a piece of paper in various patterns to form characters. For most applications, the use of dot-matrix printers has been superseded by other technologies. However, a dot-matrix printer is the only printer technology capable of generating duplicate and triplicate carbon-copy printouts.

  - *Inkjet printer*: In a piezoelectric inkjet printer, piezoelectric actuators in the printer head act on small diaphragms or otherwise change the geometry of an inkwell so that ink droplets are forced out of an orifice onto paper. This is one of the dominant technologies in the printer market to date.

- **Piezoelectric Speakers:** Piezoelectric speakers are featured in virtually every application that needs to efficiently produce sound from a small electronic gadget. These types of speakers are usually inexpensive and require little power to produce relatively large sound volumes. Thus, piezoelectric speakers are often found in devices such as the following:

  - Cell phones (see Figure 4 (e))
  - Musical greeting cards (see Figure 4(f))

- **Piezoelectric Buzzers**: Piezoelectric buzzers are similar to piezoelectric speakers, but they are usually designed with lower fidelity to produce a louder volume over a narrower frequency range. Buzzers are used in a seemingly endless array of electronic devices, including:

Intruder alarm, medical device, alarms clocks (see Figure 4(g)), fire alarm, carbon monoxide detectors, exercise equipment, microwave ovens, computer motherboards, ultrasonic insect, etc.

- **Piezoelectric ignition** (see Figure 4(h))**:** piezoelectric ignition is a type of ignition that is used in portable Camping stoves, gas grills, some lighters and potato cannons. Piezoelectric ignition uses the principle of piezoelectricity, which, in short, is the electric charge that accumulates in some materials in response to high pressure. It consists of a small, spring-loaded hammer which, when a button is pressed, hits a PZT. This sudden forceful deformation produces a high voltage and subsequent electrical discharge, which ignites the gas.

1.2.3.4   *Piezoelectric Materials for the Musical Applications*

Aside from technological and industrial applications, piezoelectricity also benefits the arts. There are a variety of musical applications that use piezoelectricity.

Figure 5: Instrument Pickups[3]

- **Instrument Pickups (Figure 5):** Many acoustic-electric stringed instruments utilize piezoelectric pickups to convert acoustic vibrations to electric signals. Typically, a strip of piezoelectric material is placed between the instrument body and a structure that supports the strings. For instance, an acoustic-electric guitar usually houses its piezoelectric strip beneath the bridge and within the saddle. As the strings vibrate, the strip is agitated to generate an electric signal. Electric pickups on violins, violas, and cellos use the same concept, but the piezoelectric pickup may be clamped to the bridge or integrated within the bridge
- **Microphones:** Some microphones (such as contact microphones for percussion instruments) use piezoelectric materials to convert sound vibrations to an electrical output. These microphones generally possess high output impedances that must be matched when designing their respective pre-amplifiers.

1.3 Nonlinearities in electromechanical systems

Electromechanical systems focus on all the devices which make electrical and mechanical systems work together. The electrical components (like diodes, resistances, capacitors and inductances) will be able to have nonlinear characteristics introduced in the electrical part by the user, while in the mechanical part; the nonlinear components are connected to the functioning of the device. Our aim in this section is to give some details on nonlinear components encountered in electromechanical systems.

1.3.1 Introduced nonlinearities

The sources of nonlinearity can be introduced in several ways: In one way, the voltage of the capacitor is a nonlinear function of the instantaneous electrical charge [68] given for instance by

$$V_c(q) = \frac{1}{C_0} q + a_2 q^2 + a_3 q^3 + \cdots , \qquad (1.1)$$

where C_0 is the value of the capacitance and a_i are the nonlinear coefficients depending on the type of the capacitor in use. This is typical of nonlinear reactance components such as varactor diodes widely used in many areas of electrical engineering to design for instance parametric amplifiers, up-converters, mixers, low-power microwave oscillators, etc [69].

Secondly, the nonlinear sources can also be obtained by using a resistor with nonlinear characteristics so that the I-V curve is given as:

$$V_{NLR} = aV + bV^3 , \qquad (1.2)$$

where a and b are the coefficients depending the way the resistor is constructed. If $a \prec 0$ and $b \succ 0$ such a resistor in an electric circuit could lead to self-sustained oscillations [70, 71].

Thirdly, we also consider an electrical circuit in which the nonlinear oscillation takes place owing to the presence of nonlinear characteristics in the flux-current relation. The inductance of an inductor that contains a ferromagnetic material can be given by the following mathematical expression [72]:

$$L = \frac{\mu_0 N^2 A_L}{l_1} + \frac{B_s NA}{i} \tanh\left(\frac{\alpha Ni}{2l_1} - \frac{\sigma}{2} \right) , \qquad (1.3)$$

with $\sigma = \beta \, sign\left(\frac{di}{dt} \right)$

There are nine parameters appearing in Eq. (1.4) that are briefly presented below (for more detailed definitions, see ([73]). B_s is the saturation flux density, A and l_1 are respectively the cross sectional area and the average length of the magnetic material. N is the number of turns, μ_0 is the permeability of the free space, i is the current through the winding. Parameters α and β are function of the remanence (B_r), the coercive magnetic field (H_c) and the saturation flux density B_s, as mathematically defined below:

$$\alpha = \frac{1}{H_c} \ln\left(\frac{B_s + B_r}{B_s - B_r} \cdot \frac{B_s - \mu_0 H_c}{B_s + \mu_0 H_c} \right) \text{ and } \beta = \ln\left(\frac{B_s + B_r}{B_s - B_r} \right) \tag{1.4}$$

1.3.2 Materials and geometric nonlinearities

This type of nonlinearity generally appears in the components of the mechanical part, particularly to a spring. For hardening spring effect in mechanical problems, it is found experimentally that the stiffness is not constant but increases with the received stress. It is approximately defined by the relation:

$$K(x) = K_0 + K_1 x^2, \tag{1.5}$$

where K_0 is the is the stiffness for small stretching, x the elongation and K_1 a coefficient of nonlinearity. An example of an electromechanical device with a nonlinear spring was studied by Chedjou et al. in refs. [70, 71] and Chembo et al. in ref. [74]. Let us note that other forms of $K(x)$ can be found such as that of the soft spring.

1.3.3 Useful and unfavorable effects of the nonlinearities

The presence of nonlinearity in science can have positive interests or negative effects. Nonlinear systems exhibit surprising and complex effects that would never be anticipated by a scientist trained only in linear techniques. Prominent examples of these are bifurcation, chaos and solitons. Nonlinearity has its most profound effects on dynamical systems and we currently not have general techniques (and very few special ones) for telling whether a particular nonlinear system will exhibit the complexity of chaos, or the simplicity of order. However, nonlinear science has applications to a wide variety of fields, ranging from physics, biology, and chemistry, to engineering, economics, and medicine. For instance, we note that undesired phenomena such as chaos are now applied to problems in many fields of science and engineering. In physics, chaos has been used to refine the understanding of planetary orbits, to conceptualize quantum level processes, and to forecast the intensity of solar activity.

In engineering, chaos has been used in the building of better digital filters, and to model the structural dynamics in such structures as buckling columns. In medicine, it has been used to study cardiac arrhythmias and patterns of disease communication. In psychology it has been used to study mood fluctuations, the operation of the olfactory lobe during perception, and patterns of innovation in organizations. In economics it is being used to find patterns and develop new types of econometric models from the stock markets to variations in good prices.

Other interesting phenomena resulting of the presence of non-linear components in science is the multi-stability, which is understood as coexistence between stability and instability phenomena encounted in various branches of science. It is usually described by discussing the possible steady-state solutions of some nonlinear process having a single variable and one or more control or bifurcation parameters. In this case, the system presents the well-known hysteresis phenomena with two stable harmonic oscillations with different amplitudes, resulting generally to the presence of the cubic nonlinearity.

1.4 Recent investigations on the nonlinear piezoelectric systems

As indicated in subsection 1.3, nonlinearities in electromechanical systems can be introduced or be inherent to the structure (stretching effects, stiffness of a soft spring and boundaries conditions on the structure). The use of piezoelectric materials in various applications, including the development of actuators, energy harvesters, vibration control, among others, has been investigated by several researchers over the last few decades. In most cases, linear piezoelectricity is assumed in modeling and analysis of such systems. However, the recent literature shows that non-linear manifestations of piezoelectric materials are relevant and can modify the electromechanical behavior.

1.4.1   Actuation by piezoelectric structures with nonlinear components

Significant progress to understand the behavior of piezoelectric actuators has been achieved, in the past, by considering linear material models. However, the range of applicability of these models is rather limited to low electrical field and stress regimes. In order to predict the actuator performance beyond the linear range of operation, or to account for phenomena such as hysteresis, sub-harmonic, multi-periodic, bursting mechanical oscillations, and chaotic behaviors, it is essential to formulate methods that are able to address nonlinearities. Numerous theoretical and experimental studies of the nonlinear behavior of piezoelectric actuators have been conducted. Royston and Houston [75] employed the Maxwell Resistive Capacitor (MRC) model, along with an experimental study, to characterize the nonlinear vibratory response of 1-3 piezocomposites. Zhao and Balachandran [76] investigated

theoretically and experimentally the influence of actuator nonlinearities on the response of panel-enclosure systems. The hysteresis effect was included in the nonlinear relationship between the free strain and applied the electrical field. Sirohi and Chopra [77] conducted an experimental study to investigate the behavior of piezoelectric sheet actuators under different types of excitation and mechanical loading. Garcia et al. [78] formulated a model that extends the analysis of nonlinear piezoelectric behavior to any kind of nonlinear function.

Since piezoelectric structures are flexible and display nonlinear deformations under external static and dynamic excitations, several authors have studied analytically, as well as experimentally, different nonlinear behavior of piezoelectric actuators [79-84] such as the implementation of nonlinearity under high and low electric fields and strains, the frequency response and the dynamics of the vibration when operating in the resonant mode. Other authors have used finite element method (FEM) to model various piezoelectric material systems [85-89], developing the finite element model for static and dynamic analysis of piezoelectric composite plates, piezoelectric bimorphs as well as for stability.

1.4.2   Nonlinear piezoelectric structures for the energy harvesting

A conventional piezoelectric energy harvester (PEH) is generally designed to operate at one resonant frequency, which may lead to a narrow operating bandwidth [90-95]. In order to overcome this limitation, several strategies [95-99] have been proposed, among which exploiting nonlinear magnetic force that becomes a promising technique for implementing broadband energy harvesters. Diverse nonlinear harvesters realized by introducing magnets to the conventional PEHs have been developed, and their improved performance in the bandwidth has been validated both theoretically and experimentally [100-104]. The motivation of using nonlinear PEH extends beyond bandwidth enhancement, and it can be used to improve overall power density as well as responsiveness towards noisy or shock excitations. Furthermore, Duffing models and bistability are the most well-known nonlinear PEH. Recently, several researchers such as Ando et al. [105] proposed a nonlinear PEH that is structured by two piezoelectric cantilever beams coupled by magnets to harness vibration energy bi-directionally. In [106-107], the Duffing oscillator model has been used for many energy harvesting simulations, with the addition of electromechanical coupling for the harvesting circuit. In the context of broad-band energy harvesting, bifurcations and chaotic vibrations have been studied in several papers [108-109]. In [110], the authors have investigated the effect of combined nonlinearities from mechanical aspects (tristable harvester) and from electrical side (nonlinear switching interface consisting of a synchronous

discharge of the piezoelectric element), providing coupled nonlinearities through the electromechanical conversion. Theoretical developments, confirmed by experimental results, demonstrated that, especially in the case of highly coupled, lightly damped structures, the backward coupling yields degraded performance in terms of bandwidth. From these works, it is worth to note that chaotic vibrations are, in most cases, characterized by moderate amplitude of vibrations and simultaneously give continuous spectrum of frequency, which can be useful to increase mechanical resonator durability.

1.4.3 Piezoelectric sensors, actuators, motors and controlers

Many studies show that, when MEMSs are submitted to AC signals, through a nonlinear electrical circuit, they show very complex behaviors [111, 112]. This complexity is a consequence of nonlinearities in the mechanical and transducing parts. They also show that, these complex behaviors found applications in medicine, engineering, sensors, actuator, energy harvester and others.

1.4.3.1   Uses of the piezoelectric ultrasounds

Figure 6: Ultrasound imaging and procedures [19-22]

- **Ultrasonic welding:** Many plastics can be joined together using a process known as ultrasonic welding. This type of process requires ultrasonic waves to be transmitted to a focused area where they can cause pieces of plastic to fuse together. Frequently, piezoelectric actuators are used to accomplish this task.

- **Ultrasound imaging (Figure 6):** Piezoelectric transducers are often used in medical ultrasound equipment. Advances in equipment over the decades have enabled improved monitoring of pregnancies and facilitated minimally invasive surgical procedures.

- **Ultrasonic medical procedures** (figure 6): Some non-invasive medical procedures rely on the use of focused ultrasonic waves to break up kidney stones or destroy malignant tissue. Additionally, the advent of the harmonic scalpel has enabled surgeons to simultaneously incise and coagulate tissue during a surgical procedure without the need for cauterization. This leads to less tissue damage, less blood loss, and faster healing times.

1.4.3.2   *Uses of Piezoelectricity in actuator*

- **Stripe actuators**: Two strips of piezoelectric material may be sandwiched together in a configuration that is similar to a bimetallic strip. In this configuration, the electric input causes one strip to expand while the other strip simultaneously contracts, causing a deflection.

- **Piezoelectric relays:** Piezoelectric elements may be implemented to actuate electromechanical relays or switches. For these applications, either stripe actuators or stack actuators may be used to open and close electrical contacts. Such devices are maintenance-free and last through many cycles without noticeable wear. As an additional benefit, using piezoelectric actuators to operate electrical contacts enables fast and precise control in small packages that are either difficult or impossible to achieve with electromagnetic relays.

- **Microelectronic mechanical mystems (MEMS):** MEMS devices have become more commonplace as more integrated capabilities are required in smaller packages, such as cell phones, tablet computers, etc. The advantage of MEMS devices is that gyroscopes, accelerometers, and inertial measuring devices can be integrated into chip-sized packages. In order to accomplish such a feat, piezoelectric actuators and sensors are often used.

1.4.3.3   *Using Piezoelectricity in micro robotics*

In the field of small robotics, small power-efficient mechanical actuators and sensors are needed. With the use of piezoelectric actuators, building something as small as a robotic fly that can crawl and fly is technically feasible. This is the case of small drones of the size of

insects or birds that fly using flapping wings. They control surfaces just as birds and insects do. They are based piezoelectric actuators.

Figure 7: Robot micro air vehicles [113]

Recently, DARPA invented a caliber bullet that can change course in mid-flight. The bullet uses an optical sensor that is mounted on its nose in conjunction with a control system and moveable tail fins to steer itself toward a laser-illuminated target. Although DARPA dis not revealed much about their Extreme Accuracy Tasked Ordinance (EXACTO) bullet, the most likely means of manipulating the tail fins probably involves piezoelectric actuators.

1.4.3.4   Piezoelectric motors

One advantage of using piezoelectric materials is that their characteristics are precise and predictable. Figure 8 show an example of a piezoelectric motor. Expansion and contraction of a piezoelectric actuator can be precisely controlled as long as the supply voltage is controlled. Some motor designs take advantage of this fact by using piezoelectric elements to move a rotor or linear element in precise increments. Precision on the order of nanometers can be achieved with some piezo motor designs. Piezo motors work at a wide range of frequencies but typically work best in a low frequency range.
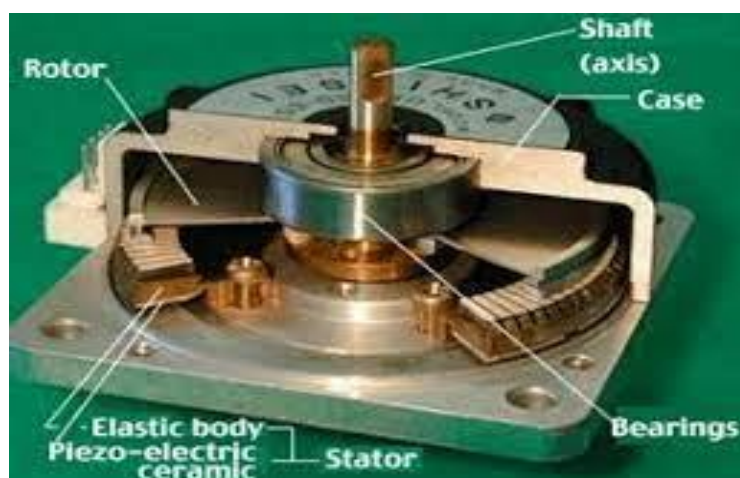
Figure 8: piezoelectric motor [113]

1.4.3.5   Vibration control using the piezoelectric structures

Different teams of researchers have been investigating ways to reduce vibrations in structures by attaching piezoelectric elements to the structure [114-121]. The principle is the following: when the structure is bent by a vibration in one direction, the vibration-reduction system responds to the bend and sends electric power to the piezoelectric element to bend in the other direction [122-125].

1.5 Problems of the thesis

As presented in section 1.2.3 above, many equivalent electrical circuit models of the piezoelectric plates have been developed based on electrical representation of the coupled electrical and mechanical systems. But most of the time, they are limited to small values of frequencies. **Little information is known when we increase the frequency range. We consider in this study a frequency range $\left[50\,\text{Hz}\,;\, 2.5 \times 10^5\,\text{Hz} \right]$. In this range of frequency, we propose an equivalent circuit having one capacitive branch associated to three parallel resonant branches. From the resonant and anti-resonant frequencies observed experimentally, the values of the electric components of each branch are obtained. We justify the existence of these many resonant branches by use the vibration mode of the plate. The second objective is to analyze the self-sustained electronic oscillator and self-sustained piezoelectric actuator.**

As mentioned above in sections 1.2.3 and 1.4.3, piezoelectric structures are used in engineering and medical tools. Because of this large numbers of applications, research investigations have been engaged in order to sort new and special motions which can be exhibited by piezoelectric beams or plates. **The third objective is to analyze the dynamical behaviors of a piezoelectric beam powered by two types of nonlinear electrical oscillators for actuation purpose, but also and possibly for the improvement of the functioning of ultrasonic nebulizers. For the fourth objective, we propose a model for the production of periodic patterns of pulse oscillations or patterns of bursting oscillations which can also find applications in the actuation engineering but also can improve the functioning of echography.**

The fifth and last objective considers a piezoelectric energy harvesting beam undergoing self-excited oscillations when the beam is submitted to the permanent action of a fluid flow.

1.6 Conclusion

In this chapter, we provided some background on piezoelectricity, piezoelectric structures and characterization of piezoelectric structures. Applications of piezoelectricity systems with nonlinearities such as energy harvesting, actuators and sensors have been presented. The problems that we will have to solve in this thesis have also been presented. The following chapter will be devoted to the methods used in the thesis to solve the problems enumerated above.

Chapter 2: Experimental, mathematical, numerical methods

2.1 Introduction

This chapter presents the methodology for the experimental characterization of a piezoelectric structure, the mathematical formalisms, the numerical methods and experimental procedure based on analog circuits, used to solve the problems of this thesis, Section 2.2 is devoted to the methodology for the experimental characterization of a piezoelectric structure. In section 2.3, the mathematical formalisms are presented. Section 2.4, is devoted to the numerical methods. Section 2.5 will present some models use in this thesis. Section 2.6 will give more details on experimental procedure based on analog circuits. In section 2.7 will conclude the chapter.

2.2 Experimental characterization of a piezoelectric plate

2.2.1 Presentation of the piezoelectric plate

The piezoelectric plate considered for this study is of the PZT type. The physical parameters associated to the PZT type are given in Table 1 [126], in which $d_{33}(m/V)$ is the piezoelectric constant, k_{33} is the electromechanical coupling factor of the material, $Y_{33}^E(Pa)$ is the Young's modulus, and $\varepsilon_{33}^T(F/m)$ is the dielectric constant.

Table 1: Parameters of the PZT specimen

Coefficients	Values	Coefficients	Values
$d_{33}(m/V)$	8.85×10^{-12}	k_{33}	0.72
$Y_{33}^E(Pa)$	169×10^9	$\varepsilon_{33}^S(F/m)$	$9,57 \times 10^{-9}$
Thickness h_p (m)	200×10^{-6}	a (mm) and b (mm)	20 and 20

2.2.2 Experimental method

The method consists to experimentally plot the frequency-impedance characteristics of the piezoelectric plate, propose an electric equivalent circuit, and finally determine the values of the electric components of the electric circuit. For this aim, the piezoelectric plate is mounted in series with a low resistance R_0 and powered by a low frequency generator (LFG) delivering a maximum voltage of $1\,V$ (Figure 9). Since the voltage delivered by the LFG is sinusoidal, we obtain for each frequency a value of the impedance given by

$$Z = \frac{U_{PZ\max}}{I_{\max}} \tag{2.1}$$

where $U_{Pz\max}$ and $I_{\max}$ are respectively the amplitude of the maximal voltage and amplitude of the maximal current.
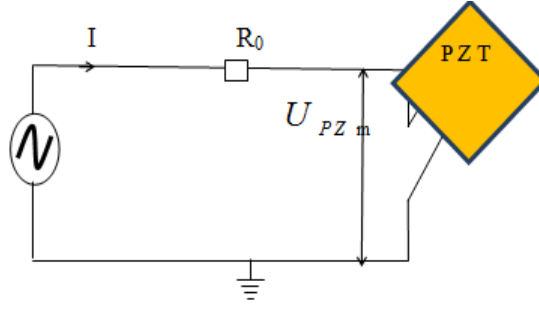
Figure 9: Experimental diagram of a piezoelectric plate in series with a resistance   and powered by a low frequency generator (LGF).

By varying the frequency of the LGF, the voltages across the resistor R_0 are taken through the oscilloscope and the PZT for each value of the frequency. The LGF being digital, the frequency of the signal delivers is read directly on its display.

2.2.3   Theoretical expression of the impedance

The impedance of the Van Dyke's circuit can be given as:

$$Z = \frac{1}{jC_0\omega}\left[\frac{1+jQ_S\left(\dfrac{\omega}{\omega_S}-\dfrac{\omega_S}{\omega}\right)}{1+jQ_P\left(\dfrac{\omega}{\omega_P}-\dfrac{\omega_P}{\omega}\right)}\right],$$ (2.2)

with, $\omega_S = \dfrac{1}{\sqrt{L_1 C_1}}$, $\omega_P = \dfrac{1}{\sqrt{L_1\left(\dfrac{C_1 \cdot C_0}{C_1 + C_0}\right)}}$, $Q_S = \dfrac{L_1\omega_S}{R_1}$, and $Q_P = \dfrac{L_1\omega_P}{R_1}$.

where ω_s is the series resonance frequency, ω_p is the parallel resonance frequency, Q_s is the series resonance quality factor and Q_p is the quality factor of parallel resonance.

2.3   Mathematical formalisms

The modeling of the linear and non-linear beam (or plate) leads to PDEs and to solve them, one needs some mathematical formalisms.

2.3.3   Modal approximation

The modal approximation is based on the Galerkin decomposition, in order to transform the system of PDEs to a system of ODEs.   The procedure consists to

approximate the solution (deflection) w by a series of time varying function $\phi_{n,m}(t)$ and linear undamped mode shape $\chi_{n,m}(x,y)$ of the form:

$$w(x,y,t) = \sum_{n=1}^{N}\sum_{m=1}^{M} \phi_{n,m}(t)\chi_{n,m}(x,y) \tag{2.3}$$

for the plate, and

$$w(x,t) = \sum_{n=1}^{N} \phi_{n}(t)\chi_{n}(x) \tag{2.4}$$

for the beam. N and M represent the number of modes retained in the solution respectively along x and y directions.

Substituting Eq. (2.3) or Eq. (2.4), multiplying by $\chi_{n,m}(x,y)$ (or $\chi_{n}(x)$ for the beam) in the PDEs of different structures and integrating over the surface of the plate (or the length of the beam), one obtains the ODEs.

2.3.4 Harmonic balance method

The harmonic balance method is an approximation method used to estimate periodic solutions of nonlinear ODEs. Consider the following differential equation:

$$\ddot{x} + x = f(\dot{x},x,t) \tag{2.5}$$

where the function f satisfies the following condition $f(\dot{x},x,t+T) = f(\dot{x},x,t)$.

The harmonic solution of equation (2.5) is expressed as follows:

$$x = A\sin(\omega t + \varphi) = A_1 \sin \omega t + A_2 \cos \omega t \tag{2.6}$$

where $A = \sqrt{A_1^2 + A_2^2}$ is the amplitude of oscillations, ω the pulsation of the sinusoidal excitation and φ the phase at the origin.

Expression (2.6) is inserted in equation 2.5 to obtain A and φ or A_1 and A_2. In this procedure, terms containing $\cos n\omega t$ and $\sin n\omega t$ with $n \neq 1$ are discarded.

2.3.5 Routh-Hurwitz criterion

The Routh-Hurwitz criterion can be defined as algebraic criterion which allows evaluating the stability of a system from the coefficients of the characteristic equation. Let us consider the following characteristic equation

$$a_0 p^n + a_1 p^{n-1} + \ldots + a_{n-1} p + a_n = 0 \tag{2.7}$$

The determination of the signs of the real parts of the roots p can be carried out by making use of the Routh-Hurwitz criterion [127,128]. Applying this criterion, we constructs firstly, a set of n determinants set up from the coefficients of the $n^{th}-$ degree characteristic equation Eq. (2.8). These determinants are given as follows

$$\Delta_1 = |a_1|, \quad \Delta_2 = \begin{vmatrix} a_1 & a_0 \\ a_3 & a_2 \end{vmatrix}, \quad \Delta_3 = \begin{vmatrix} a_1 & a_0 & 0 \\ a_3 & a_2 & a_1 \\ a_5 & a_4 & a_3 \end{vmatrix}, \quad \ldots, \quad \Delta_n = \begin{vmatrix} a_1 & a_0 & 0 & 0 & \ldots & 0 \\ a_3 & a_2 & a_1 & a_0 & \ldots & 0 \\ a_5 & a_4 & a_3 & a_2 & \ldots & 0 \\ .. & .. & .. & .. & \ldots & 0 \\ .. & .. & .. & .. & \ldots & 0 \\ 0 & 0 & 0 & 0 & \ldots & a_n \end{vmatrix} \tag{2.8}$$

The Routh-Hurwitz criterion states that the real parts of the roots are negative provided that all coefficients $a_0, a_1, \ldots, a_n$ are positive and that all the determinants are positive also. Since the bottom row of the determinant Δ_n is composed entirely of zeros, except for the last element a_n, it follows that $\Delta_n = a_n \Delta_{n-1}$. Thus, for stability it is required that both $a_n > 0$ and $\Delta_{n-1} > 0$.

2.3.6 Cardano's method

The Cardano method is used to solve a third-order polynomial equations [129]. Let us consider the following equation:

$$ax^3 + bx^2 + cx + d = 0 \tag{2.9}$$

Considering $x = z - \dfrac{b}{3a}$, we obtain the canonical equation below:

$$z^3 + pz + q = 0 \tag{2.10}$$

where $p = -\dfrac{b^2}{3a^2} + \dfrac{c}{a}$ and $q = \dfrac{b}{27a}\left(\dfrac{2b^2}{a^2} - \dfrac{9c}{c}\right) + \dfrac{d}{a}$ \tag{2.11}

According to the sign of the discriminant $\Delta = q^2 + \dfrac{4}{27} p^3$, the solutions of equations (2.11) are obtained:

- If $\Delta \succ 0$, the equation possesses one real z_0 and two complexes z_1 and z_2, all solutions of them given below:

$$\begin{cases} z_0 = u + v \\ z_1 = ju + jv \\ z_2 = j^2u + j^2v \end{cases} \tag{2.12}$$

where $j = -\dfrac{1}{2} + i\dfrac{\sqrt{3}}{2}$; $u = \sqrt[3]{\dfrac{-q+\sqrt{\Delta}}{2}}$ and $v = \sqrt[3]{\dfrac{-q-\sqrt{\Delta}}{2}}$

- If $\Delta = 0$, the equation possesses two real solutions, one simple z_0 and one double z_1.

$$z_0 = 2\sqrt[3]{\dfrac{-q}{2}} = 2\sqrt[3]{\dfrac{-p}{2}} = 3\dfrac{q}{p}$$

$$z_1 = z_2 = -\sqrt[3]{\dfrac{-q}{2}} = -\sqrt[3]{\dfrac{-p}{2}} = -\dfrac{3q}{2p} \tag{2.13}$$

- If $\Delta \prec 0$, the equation possesses three real solutions, z_0, z_1, z_2.

$$z_k = 2\sqrt{-\dfrac{p}{3}} \cos\left[\dfrac{1}{3} ar\cos\left(\dfrac{-q}{2}\sqrt{\dfrac{27}{-p^3}} + \dfrac{2k\pi}{3}\right)\right] \quad k \in \{1,2,3\} \tag{2.14}$$

This method is used to solve the third order polynomial equation, for equilibrium and instability studies.

2.4   Numerical methods

After using the modal approximation, one needs to solve numerically the ODEs and PDEs using appropriate methods.

2.4.1   Finite differences method

The modelling of a plate and beam dynamics led us to two dimensional partial differential equations which can be solved directly using the finite differences method. For the time differentiations, the forward difference formula is used and one writes

$$\dfrac{\partial w}{\partial t} = \dfrac{w_{i,j}^{k+1} - w_{i,j}^{k-1}}{2h}$$

$$\dfrac{\partial^2 w}{\partial t^2} = \dfrac{w_{i,j}^{k+1} - 2w_{i,j}^{k} + w_{i,j}^{k-1}}{h^2} \tag{2.15}$$

where k runs for time incrementation, i and j run for space increment variables x and y.

For the spatial derivatives, one uses the following formulas:

$$\frac{\partial w}{\partial x} = \frac{w_{i+1,j}^k - w_{i-1,j}^k}{2\Delta x}$$

$$\frac{\partial^2 w}{\partial x \partial y} = \frac{w_{i+1,j+1}^k - w_{i+1,j-1}^k - w_{i-1,j+1}^k + w_{i-1,j-1}^k}{4\Delta x \Delta y}$$

$$\frac{\partial^2 w}{\partial x^2} = \frac{w_{i+1,j}^k - 2w_{i,j}^k + w_{i-1,j}^k}{\left(\Delta x\right)^2}$$

$$\frac{\partial^4 w}{\partial x^4} = \frac{w_{i+2,j}^k - 4w_{i+1,j}^k + 6w_{i,j}^k - 4w_{i-1,j}^k + w_{i-2,j}^k}{\left(\Delta x\right)^4}$$

$$\frac{\partial^4 w}{\partial y^4} = \frac{w_{i,j+2}^k - 4w_{i,j+1}^k + 6w_{i,j}^k - 4w_{i,j-1}^k + w_{i,j-2}^k}{\left(\Delta y\right)^4}$$

$$\frac{\partial^4 w}{\partial x^2 \partial y^2} = \frac{w_{i+1,j+1}^k - 2w_{i,j+1}^k + w_{i-1,j+1}^k - 2\left(w_{i+1,j}^k - 2w_{i,j}^k + w_{i-1,j}^k\right) + w_{i+1,j-1}^k - 2w_{i,j-1}^k + w_{i-1,j-1}^k}{\left(\Delta y\right)^4}$$

(2.16)

where h is the time step of time, Δx and Δy are respectively the difference step along $x-$ and $y-$ directions.

2.4.2   Fourth-order Runge-Kutta method

2.4.2.1   For first-order differential equation

Runge-Kutta methods are an important family of implicit and explicit iterative methods for the approximation of solutions of ODEs. These techniques have been elaborated for the first time in 1894 by Carle Runge and have improved by Martin W. Kutta in 1901 [130,131].

Let us consider the following ODE:

$$\frac{\mathrm{d}x(t)}{\mathrm{d}t} = f\left(x(t),t\right) \quad \text{with} \quad x(t_0) = x_0 \tag{2.17}$$

where f is a function with the unknown variable $x(t)$.

The RK4 scheme for this problem is given by:

$$\begin{aligned}
x_{i+1} &\leftarrow x_i + \frac{1}{6}\left(L_1 + 2\left(L_2 + 2L_3\right) + L_4\right), \\
t &\leftarrow t + h,
\end{aligned} \tag{2.18}$$

where

$$L_1 \leftarrow h \cdot f\left(x_i, t\right),$$
$$L_2 \leftarrow h \cdot f\left(x_i + L_1/2, t + h/2\right),$$
$$L_3 \leftarrow h \cdot f\left(x_i + L_2/2, t + h/2\right),$$
$$L_4 \leftarrow h \cdot f\left(x_i + L_3, t + h\right),$$

(2.19)

2.4.2.2 *For m-order differential equation*

In the case of m-order differential equation, we have:

$$\begin{cases} \dfrac{d^m y}{dt^m} = f_m\left(t, y, \dfrac{dy}{dt}, \dfrac{d^2 y}{dt^2}, \dfrac{d^{m-1} y}{dt^{m-1}}\right) \\ \dfrac{d^k y}{dt^k}\left(t_0\right) = y_0^{(k)} \end{cases},$$

(2.20)

With successive variables change, the equation (2.20) can be written under the following form:

$$\begin{cases} \dfrac{d^0 y}{dt^0} = u_0 = y = f_0\left(t, u_0, u_1, u_{2\ldots}, u_{m-1}\right) \\[2mm] \dfrac{dy}{dt} = \dfrac{du_0}{dt} = u_1 = f_1\left(t, u_0, u_1, u_{2\ldots}, u_{m-1}\right) \\[2mm] \dfrac{d^2 y}{dt^2} = \dfrac{du_1}{dt} = u_2 = f_2\left(t, u_0, u_1, u_{2\ldots}, u_{m-1}\right) \\[2mm] \vdots \\[2mm] \dfrac{d^{m-1} y}{dt^{m-1}} = \dfrac{du_{m-2}}{dt} = u_{m-1} = f_{m-1}\left(t, u_0, u_1, u_{2\ldots}, u_{m-1}\right) \\[2mm] \dfrac{d^m y}{dt^m} = \dfrac{du_{m-1}}{dt} = f_m\left(t, u_0, u_1, u_{2\ldots}, u_{m-1}\right) \\[2mm] \dfrac{d^k y}{dt^k}\left(t_0\right) = u_k\left(t_0\right) = y_0^{(k)} k \in \{1, 2, 3, \cdots, m-1\} \end{cases}$$

(2.21)

With this general vectorial form, iterations can be performed to determine all the values of y and its derivative at different time separated by the time step h using:

$$u_k\left(t + h\right) \leftarrow u_k\left(t\right) + \frac{1}{6}\left(L_1^k + 2\left(L_2^k + L_3^k\right) + L_4^k\right)$$

(2.22)

where

$$L_1^k = hf_k\left[t, u_0(t), u_1(t), \ldots, u_{m-1}(t)\right];$$

$$L_2^k = hf_k\left[t+\frac{h}{2}, u_0(t)+\frac{L_1^0}{2}, u_1(t)+\frac{L_1^1}{2}, \ldots, u_{m-1}(t)+\frac{L_1^{m-1}}{2}\right];$$

$$L_3^k = hf_k\left[t+\frac{h}{2}, u_0(t)+\frac{L_2^0}{2}, u_1(t)+\frac{L_2^1}{2}, \ldots, u_{m-1}(t)+\frac{L_2^{m-1}}{2}\right];$$

$$L_4^k = hf_k\left[t+\frac{h}{2}, u_0(t)+\frac{L_3^0}{2}, u_1(t)+\frac{L_3^1}{2}, \ldots, u_{m-1}(t)+\frac{L_3^{m-1}}{2}\right].$$

$$(2.23)$$

This generalized form can also serve to solve numerically first-order coupled ODEs.

2.4.3 Numerical tools for the characterization of the dynamical states of non-linear systems

Many numerical tools such as times series, phase portraits, Poincare section and bifurcation diagrams are usually used to analyze the dynamical states of nonlinear systems. In this section, we present brief information on the numerical tools which are used for characterizing different dynamical states of nonlinear dynamics of plates in the different study cases considered in this thesis.

2.4.3.1 Phase portrait

The phase portrait of a dynamical system is a geometric representation of their trajectories in the phase plane: a coordinate plane with axes being the values of the two state variables of dynamical system. Phase portraits reveal information such as whether an attractor or a limit cycle is observed for the chosen parameter value. However, the distinction between the quasi-periodicity and chaos phenomena is the drawback of this numerical tool. To solve this problem, the most reliable numerical tool is the bifurcation diagram with the Lyapunov exponent.

2.4.3.2 Bifurcation diagrams

A bifurcation is a phenomenon in which, the properties of a dynamical system changes qualitatively when a control parameter of the system is varied. In order to plot the bifurcation diagram of continuous dynamical systems, a set of consecutive maxima of variable representing the attractor must be obtained or a periodic capture of the variable after each period when the period is known. In the bifurcation phenomena, attractors may appear, disappear or be replaced by another one. Bifurcation diagrams help us to visualize these transitions. Thus, one can identify the fixed points, periodic orbits, or chaotic attractors. One can also identify various routes to chaos taken by dynamical systems. The most common are: the period doubling route, the quasi-periodic route and intermittency route

2.4.3.3   Lyapunov exponent

The bifurcation diagram is accompanied by the variation of the Lyapunov exponent's spectra or that of the largest Lyapunov exponent. To calculate the largest Lyapunov exponent we must consider a small derivation from the process $x(t)$ for example noted by δx, which satisfies the equation $\delta \dot{x} = J(x)$. J is a Jacobian matrix of the dynamic equation with respect of the state variable $x(t)$. Then the largest Lyapunov exponent is calculated as:

$$Lya = \lim_{t \to +\infty} \frac{1}{t} \log\left(\|\delta x\|\right) \tag{2.24}$$

2.5   Some models use in this thesis

2.5.1   Model for the vibrations modes of the plate

2.5.1.1 Physical model and equation

Because of the difficulty of the values of all the parameters of the piezoelectric plate, the development that follows will only tackle the question of giving a qualitative explanation of the many resonant branches in the electric equivalent of the piezoelectric plate. We consider an amorph piezoelectric plate as presented in Figure 19. It is constituted of a *PZT* layer perfectly bonded to a substructure layer. A resistive load R_0 is connected to the plate. The system is excited by a low frequency generator that delivers a maximum voltage of *1 V* as in the previous section.
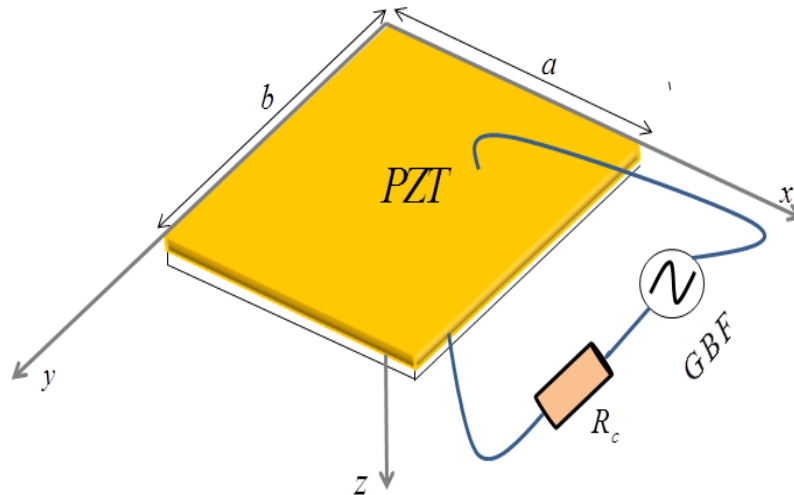
Figure 10: Presentation of the piezoelectric plate under a sinusoidal excitation.

In reference [126], one established that the plate deflection, the voltage and current in the piezoelectric plate are described by the following set of partial differential equations

$$\begin{cases} \rho^1 \dfrac{\partial^2 w}{\partial t^2} + \lambda \dfrac{\partial w}{\partial t} + D\left(\dfrac{\partial^4 w}{\partial x^4} + 2\dfrac{\partial^4 w}{\partial x^2 \partial y^2} + \dfrac{\partial^4 w}{\partial y^4}\right) + D_p\left(\dfrac{\partial^4 w}{\partial x^4} + 2(\alpha+\gamma)\dfrac{\partial^4 w}{\partial x^2 \partial y^2} + \dfrac{\partial^4 w}{\partial y^4}\right) = -\vartheta v(t) \times \\[2mm] \left[\left(\dfrac{d\delta(x)}{dx} - \dfrac{d\delta(x-a)}{dx}\right)\left(H(y) - H(y-b)\right) + \left(H(x) - H(x-a)\right)\left(\dfrac{d\delta(y)}{dy} - \dfrac{d\delta(y-b)}{dy}\right)\right] \\[3mm] \dfrac{dv(t)}{dt} + \eta v(t) + \varsigma \displaystyle\int_0^b \int_0^a \left(\dfrac{\partial^3 w}{\partial x^2 \partial t} + \dfrac{\partial^3 w}{\partial y^2 \partial t}\right) dx\, dy = -u_0 \sin \omega t \\[3mm] i(t) = -e_{31} h_{pc} \displaystyle\int_0^b \int_0^a \left(\dfrac{\partial^3 w}{\partial x^2 \partial t} + \dfrac{\partial^3 w}{\partial y^2 \partial t}\right) dx\, dy - \dfrac{\varepsilon_{33}^s ab}{h_p} \dfrac{dv(t)}{dt} \end{cases} \quad (2.25)$$

where w is the deflection, $\rho^1 = (\rho h + \rho_p h_p)$ (ρ being the density of the thin plate of thickness h, and ρ_p the density of the *PZT* with thickness h_p), λ is the damping coefficient for mechanical vibration. The other coefficients are defined as follows:

$$D = \frac{E_s h^3}{12(1-\upsilon^2)}, \quad D_p = \frac{c_{11}^E (8h_b^3 - h^3)}{24}, \quad c_{11}^E = \frac{s_{11}^E}{\left(s_{11}^E + s_{12}^E\right)\left(s_{11}^E - s_{12}^E\right)}, \quad \vartheta = \frac{e_{31}(4h_b^2 - h^2)}{8h_p}$$

$$\alpha = \frac{-s_{12}^E}{s_{11}^E}, \quad \gamma = \frac{C_p}{D_p}, \quad \eta = \frac{h_p}{R_0 \varepsilon_{33}^s ab}, \quad \varsigma = \frac{h_p e_{31} h_{pc}}{\varepsilon_{33}^s ab}, \quad e_{31} = \frac{d_{31}}{S_{11}^E + S_{12}^E}$$

S_{ij}^E are elastic compliances at constant electric field and ε_{ij}^T are dielectric coefficients at constants stress. E_s is the Young's modulus and ν the Poisson ratio. a and b are the lengths of the plate. $\delta(x)$ and H(x) are respectively the Dirac delta function and the Heaviside function.

The boundaries conditions are given as:

$$\begin{aligned} w(0,x,t) &= w(a,x,t) = 0; \quad \frac{\partial w^2(0,y,t)}{\partial x^2} = \frac{\partial w^2(a,y,t)}{\partial x^2} = 0 \\[2mm] w(x,0,t) &= w(x,b,t) = 0; \quad \frac{\partial w^2(x,0,t)}{\partial y^2} = \frac{\partial w^2(x,b,t)}{\partial y^2} = 0 \end{aligned} \quad (2.26)$$

Which express that the displacement and flexural moment vanish at the boundaries of the plate.

The values of other parameters of the piezoelectric system used in this paper are presented in Table 4 [126,132].

Table 4: Geometric, material and electro-mechanical parameters of the substructure and of the piezoelectric layer.

Coefficients	Values	Coefficients	Values
Length a (mm)	20	Y_{33}^{E} (Pa)	$4,9 \times 10^{10}$
Width b (mm)	20	ε_{33}^{T} (nF/m)	$16,02$
Thickness h (μm)	20	c_{11}^{E} (GPa)	69.5
Damping λ (Ns/m)	400	c_{12}^{E} (GPa)	24.5
E^{S} (N/m^{2})	169×10^{9}	c_{66}^{E} (GPa)	22.6
Poisson's ratio υ_{s}	0.3	e_{31} (C/m^{2})	-16
Density ρ_{S} (kg/m^{3})	4500	ε_{33}^{S} (nF/m^{2})	9.57
Density ρ_{p} (kg/m^{3})	7800	d_{31}	-190×10^{-12}

2.5.1.2 Modal equation

With the boundary conditions and making use of the Galerkin decomposition method, we set the transversal deflection of the plate in the following form.

$$w(x,\ y,\ t) = \sum_{n=1}^{\infty} \sum_{m=1}^{\infty} r_{n,m}(t) \sin\left(\frac{n\pi}{a} x\right) \sin\left(\frac{m\pi}{b} y\right) \qquad (2.27)$$

If $\phi_{n,m}(\tau)$ are the amplitudes of the $(n,\ m)$ modes. Substituting Eq. (2.27) into Eq. (2.25) and by means of the Galerkin's method, one obtains

$$\begin{cases} \ddot{\varphi}_{n,m}(\tau) + \lambda_{0}\dot{\varphi}_{n,m}(\tau) + c\varphi_{n,m}(\tau) = \vartheta_{0}v_{r} \\ \dot{v}_{r}(\tau) + \eta_{0}v_{r}(\tau) = E_{0}\sin\Omega\tau - \varsigma_{0}\dot{\varphi}_{n,m}(\tau) \\ i_{r}(\tau) = c_{1}\dot{v}_{r}(\tau) + c_{2}\dot{\varphi}_{n,m}(\tau) \end{cases} \qquad (2.28)$$

$$\text{With}\begin{cases} \varphi_{n,m} = \dfrac{r_{n,m}}{h_p}, \tau = \dfrac{t}{T_{nm}}, \ v(t) = v_0 v_r(\tau), \ T_{nm}^2 = \dfrac{(\rho h + \rho_p h_p)}{D\left[\left(\dfrac{n\pi}{a}\right)^2 + \left(\dfrac{m\pi}{b}\right)^2\right]^2}, \\[4mm] \lambda_{0_{nm}} = \dfrac{\lambda T}{(\rho h + \rho_p h_p)}; c_{nm} = (1 + D_{p0_{nm}}), \ \vartheta_{0_{nm}} = \dfrac{-8T_{nm}^2(a^2+b^2)v_0}{(\rho h + \rho_p h_p)h_p a^2 b^2}\vartheta, \\[4mm] \varsigma_0 = \dfrac{-4(a^2+b^2)h_p}{abv_0}\varsigma, \ E_{0_{nm}} = \dfrac{-T_{nm}u_0}{v_0}; \Omega = \omega T_{nm}, \ c_{1nm} = \dfrac{-ab\varepsilon_{33}^s v_0}{i_0 h_p T_{nm}}, \\[4mm] c_{2nm} = \dfrac{4e_{31}h_p h_{pc}(a^2+b^2)}{i_0 ab}, \\[4mm] D_{p0_{nm}} = \dfrac{T_{nm}^2 D_p}{(\rho h + \rho_p h_p)}\left[\left(\dfrac{n\pi}{a}\right)^4 + 2(\alpha+\gamma)\left(\dfrac{\pi nm}{ab}\right)^2 + \left(\dfrac{m\pi}{b}\right)^4\right] \end{cases} \tag{2.29}$$

$T(n,m)$ is the natural period of vibration to the substructure.

2.5.1.3 Analytical treatment

The differential Eq. (2.27) can be solved analytically by making use of the harmonic balance method for which one writes

$$\begin{cases} \varphi = A_1(n,m)\cos\Omega\tau + A_2(n,m)\sin\Omega\tau \\ v_r = B_1(n,m)\cos\Omega\tau + B_2(n,m)\sin\Omega\tau \\ i_r = D_1(n,m)\cos\Omega\tau + D_2(n,m)\sin\Omega\tau \end{cases} \tag{2.30}$$

Inserting Eqs. (2.30) into Eqs. (2.27), equating the coefficients $\sin\Omega\tau$ and $\cos\Omega\tau$, show that the amplitude φ, v_r and i_r obeys to the followings linear algebraic equation

$$\begin{cases} A_1(n,m) = \dfrac{1}{\left[(c-\Omega^2+\gamma_1)^2 + (\lambda_0\Omega+\gamma_2)^2\right]}\left[-\gamma_3(c-\Omega^2+\gamma_1) + \gamma_4(\lambda_0\Omega+\gamma_2)\right] \\[4mm] A_2(n,m) = \dfrac{1}{\left[(c-\Omega^2+\gamma_1)^2 + (\lambda_0\Omega+\gamma_2)^2\right]}\left[\gamma_4(c-\Omega^2+\gamma_1) - \gamma_3(\lambda_0\Omega+\gamma_2)\right] \end{cases} \tag{2.31a}$$

with $\gamma_1 = \dfrac{\vartheta_0\Omega^2 E_0}{\Omega^2+\eta_0^2}$, $\gamma_2 = \dfrac{\vartheta_0\Omega\varsigma_0\eta_0}{\Omega^2+\eta_0^2}$, $\gamma_3 = \dfrac{\vartheta_0\Omega E_0}{\Omega^2+\eta_0^2}$, $\gamma_4 = \dfrac{\vartheta_0\varsigma_0\eta_0}{\Omega^2+\eta_0^2}$.

$$\begin{cases} B_1(n,m) = \dfrac{-E_0(\Omega + g_4)}{\left[(\Omega + g_1)(\Omega + g_4) + (E_0 + g_3)(\eta_0 + g_2)\right]} \\[4mm] B_2(n,m) = \dfrac{E_0(E_0 + g_3)}{\left[(\Omega + g_4)(\Omega + g_1) + (\eta_0 + g_3)(\eta_0 + g_2)\right]} \end{cases} \tag{2.31b}$$

With
$$g_1 = \frac{\vartheta_0 \varsigma_0 \Omega (1 - \Omega^2)}{\left[(c - \Omega^2)^2 + (\lambda_0 \Omega)^2\right]}, \; g_2 = \frac{\lambda_0 \vartheta_0 \varsigma_0 \Omega^2}{\left[(c - \Omega^2)^2 + (\lambda_0 \Omega)^2\right]},$$

$$g_3 = \frac{\lambda_0 \vartheta_0 \varsigma_0 \Omega^2}{\left[(c - \Omega^2)^2 + (\lambda_0 \Omega)^2\right]}, \; \sqrt{\;} g_4 = \frac{\vartheta_0 \varsigma_0 \Omega (1 - \Omega^2)}{\left[(c - \Omega^2)^2 + (\lambda_0 \Omega)^2\right]}$$

$$\begin{cases} D_1(n,m) = \left\{ \begin{aligned} & c_1\left(\dfrac{E_0(E_0 + g_3)}{\left[(\Omega + g_4)(\Omega + g_1) + (\eta_0 + g_3)(\eta_0 + g_2)\right]}\right) + \\ & c_2\left(\dfrac{1}{\left[(c - \Omega^2 + \gamma_1)^2 + (\lambda_0 \Omega + \gamma_2)^2\right]}\left[\begin{matrix}\gamma_4(c - \Omega^2 + \gamma_1) - \\ \gamma_3(\lambda_0 \Omega + \gamma_2)\end{matrix}\right]\right) \end{aligned} \right\}\Omega \\[10mm] D_2(n,m) = -\left\{ \begin{aligned} & c_1\left(\dfrac{-E_0(\Omega + g_4)}{\left[(\Omega + g_1)(\Omega + g_4) + (E_0 + g_3)(\eta_0 + g_2)\right]}\right) + \\ & c_2\left(\dfrac{1}{\left[(c - \Omega^2 + \gamma_1)^2 + (\lambda_0 \Omega + \gamma_2)^2\right]}\left[\begin{matrix}-\gamma_3(c - \Omega^2 + \gamma_1) + \\ \gamma_4(\lambda_0 \Omega + \gamma_2)\end{matrix}\right]\right) \end{aligned} \right\}\Omega \end{cases} \tag{2.32}$$

2.5.1.4 Finite difference scheme

By applying the central spatial and temporal discretization with space and temporal steps adequately chosen to avoid numerical instability. Consequently, (2.27) become:

$$\begin{cases} w_{i,j}^{(k+1)} = (1/A_0)\left(-B_0 w_{i,j}^{(k-1)} + 2w_{i,j}^{(k)} - B_1\left(20 w_{i,j}^{(k)} - 8\left(w_{i+1,j}^{(k)} + w_{i-1,j}^{(k)} + w_{i,j+1}^{(k)} + w_{i,j-1}^{(k)}\right)\right.\right. \\ \left.+ w_{i+2,j}^{(k)} + w_{i-2,j}^{(k)} + w_{i,j+2}^{(k)} + w_{i,j-2}^{(k)} + 2\left(w_{i+1,j+1}^{(k)} + w_{i+1,j-1}^{(k)} + w_{i-1,j+1}^{(k)} + w_{i-1,j-1}^{(k)}\right)\right) + \\ p_0\left(w_{i+1,j}^{(k)} - 2w_{i,j}^{(k)} + w_{i-1,j}^{(k)}\right) - A_1((12 + (\alpha + \gamma))w_{i,j}^{(k)} - \\ 4(1 + \alpha + \gamma)\left(w_{i+1,j}^{(k)} + w_{i-1,j}^{(k)} + w_{i,j+1}^{(k)} + w_{i,j-1}^{(k)}\right) + 2(\alpha + \gamma) \\ \times\left(w_{i+1,j+1}^{(k)} + w_{i+1,j-1}^{(k)} + w_{i-1,j+1}^{(k)} + w_{i-1,j-1}^{(k)}\right) + w_{i+2,j}^{(k)} + w_{i-2,j}^{(k)} + w_{i,j+2}^{(k)} + w_{i,j-2}^{(k)}) - \vartheta_1 v^{(k)}\right) \\ v^{(k+1)} = (1 - \eta_0 dt)v^{(k)} - \zeta_0 \text{tr} - u_1 \sin(\omega_0 t) \\ i^{(k)} = \vartheta_2 \text{tr} - \vartheta_3(v^{(k+1)} - v^{(k)}) \end{cases} \tag{2.33}$$

where, $A_0 = \dfrac{(1 + \lambda_1 dt)}{2}; B_0 = \dfrac{(1 - \lambda_1 dt)}{2}; A_1 = \dfrac{D_{P0} dt^2}{dx^4}; B_1 = \dfrac{dt^2}{(G dx^4)};$

$$\vartheta_0 = \frac{\vartheta dt^2}{(\rho h + \rho h_p)(dx\omega_n)^2}; \eta = \frac{h_p}{\varepsilon_{33}abR_l}; \xi = \frac{h_p e_{31} h_{pc}}{\varepsilon_{33}ab};$$

$$\eta_0 = \frac{\eta dt}{\omega_n}; \xi_0 = \frac{\xi}{8}; u_1 = \frac{u_0 dt}{\omega_n}; \vartheta_2 = \frac{-e_{31} h_{pc}\omega_n}{8dt}; \vartheta_3 = \frac{\varepsilon_{33}ab\omega_n}{h_p dt}$$

$$f(i,j) = w_{i+1,j}^{(k+1)} - 2w_{i,j}^{(k+1)} + w_{i-1,j}^{(k+1)} - \left(w_{i+1,j}^{(k-1)} - 2w_{i,j}^{(k-1)} + w_{i-1,j}^{(k-1)}\right)$$

$$g(i,j) = w_{i,j+1}^{(k+1)} - 2w_{i,j}^{(k+1)} + w_{i,j-1}^{(k+1)} - \left(w_{i,j+1}^{(k-1)} - 2w_{i,j}^{(k-1)} + w_{i,j-1}^{(k-1)}\right)$$

$$\mathrm{tr} = \frac{1}{8d\tau}\left\{\begin{array}{l} f(i_0,j_0)+f(i_0,j_m)+f(i_n,j_0)+f(i_n,j_m)+4\sum_{i=1}^{n}\sum_{j=1}^{m}f(i,j) \\[2mm] 2\sum_{j=1}^{m}\left[f(i_0,j)+f(i_n,j)\right]+2\sum_{i=1}^{n}\left[f(i,j_0)+f(i,j_m)\right] \\[2mm] g(i_0,j_0)+g(i_0,j_m)+g(i_n,j_0)+g(i_n,j_m)+4\sum_{i=1}^{n}\sum_{j=1}^{m}g(i,j) \\[2mm] 2\sum_{j=1}^{m}\left[g(i_0,j)+g(i_n,j)\right]+2\sum_{i=1}^{n}\left[g(i,j_0)+g(i,j_m)\right] \end{array}\right\}$$

The boundary conditions are given as follows:

$$w_{1,j}^{(k)} = 0 \; ; \; w_{n+2,j}^{(k)} = -w_{n,j}^{(k)} \; ; \; w_{i,1}^{(k)} = 0 \; ; \; w_{i,m+2}^{(k)} = -w_{i,m}^{(k)}. \tag{2.34}$$

2.5.2 Model for the self-sustained actuator of the plate

The self-sustained piezoelectric actuator has the same structure as in Figure 20. But, the resistance and external generator is replaced by a nonlinear resistor which is the one used to generate Van der Pol type oscillations (see Figure 11). The idea here is to transform the electric part so that it behaves like a Van der Pol oscillator. To achieve this, we add a coil in parallel to the nonlinear resistance (NLR). It is expected that the system will lead to self-sustained electrical oscillations and mechanical vibrations. We first consider the electric signature with a theoretical and experimental study and then the analysis of the mechanical vibration is conducted theoretically using the partial differential equations of the system.
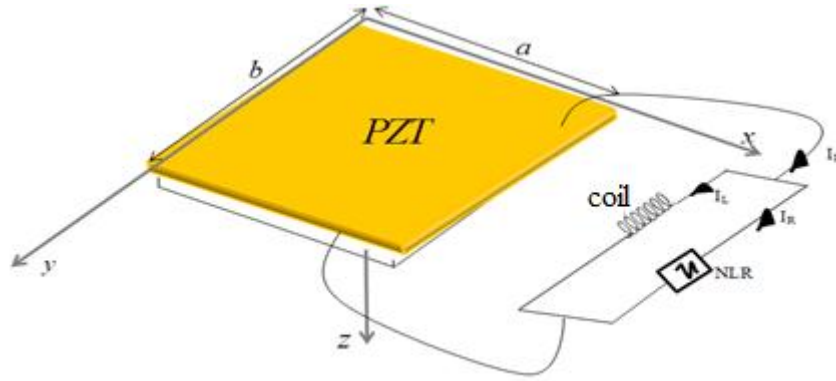
Figure 11: Presentation of the piezoelectric plate in parallel with a coil and a non-linear resistance

Considering Figure 11, and applying the Kirchhoff's laws, one can write

$$I_p = I_L + I_R \tag{2.35}$$

With

$$I_p = i(t) = -\int_0^b \int_0^a \left\{ e_{31} h_{pc} \left(\frac{\partial^3 w}{\partial x^2 \partial t} + \frac{\partial^3 w}{\partial y^2 \partial t} \right) \right\} dx dy - \frac{\varepsilon_{33}^s ab}{h_p} \frac{dV(t)}{dt}, \quad I_{NLR} = a_0 V + b_0 V^3 \text{ and}$$

$$I_L = \frac{1}{L} \int V dt .$$

The above relations lead to the following differential equation satisfied by the voltage across the piezoelectric plate:

$$\frac{\varepsilon_{33}^s ab}{h_p} \frac{d^2 V(t)}{dt^2} + (a_0 + b_0 V^2) \frac{dV}{dt} + \frac{1}{L} V + \int_0^b \int_0^a \left\{ e_{31} h_{pc} \left(\frac{\partial^2 w}{\partial x^2} \frac{\partial^2 w}{\partial t^2} + \frac{\partial^2 w}{\partial y^2} \frac{\partial^2 w}{\partial t^2} \right) \right\} dx dy = 0 \tag{2.36}$$

Hence the self-sustained piezoelectric plate equations are in the following form:

$$\begin{cases} \rho^1 \frac{\partial^2 w}{\partial t^2} + \lambda \frac{\partial w}{\partial t} + D\left(\frac{\partial^4 w}{\partial x^4} + 2\frac{\partial^4 w}{\partial x^2 \partial y^2} + \frac{\partial^4 w}{\partial y^4} \right) + D_p \left(\begin{array}{c} \frac{\partial^4 w}{\partial x^4} + \\ 2(\alpha + \gamma)\frac{\partial^4 w}{\partial x^2 \partial y^2} + \\ \frac{\partial^4 w}{\partial y^4} \end{array} \right) = \\ \quad -\vartheta V(t) \left[\begin{array}{c} \left(\frac{d\delta(x)}{dx} - \frac{d\delta(x-a)}{dx} \right) (H(y) - H(y-b)) + \\ (H(x) - H(x-a))\left(\frac{d\delta(y)}{dy} - \frac{d\delta(y-b)}{dy} \right) \end{array} \right] \\ \frac{\varepsilon_{33}^s ab}{h_p} \frac{d^2 V(t)}{dt^2} + (a_0 + b_0 V^2)\frac{dV}{dt} + \frac{1}{L}V + \int_0^b \int_0^a \left\{ e_{31} h_{pc} \left(\frac{\partial^4 w}{\partial x^2 \partial t^2} + \frac{\partial^4 w}{\partial y^2 \partial t^2} \right) \right\} dx dy = 0 \end{cases} \tag{2.37}$$

Substituting Eq. (3.4) into Eq. (3.28) and by means of the Galerkin's method, we obtain the following dimensionless differential equations:

$$\begin{cases} \ddot{\varphi}_{n,m}(\tau) + \lambda_0 \dot{\varphi}_{n,m}(\tau) + c\varphi_{n,m}(\tau) = \vartheta_1 S \\ \ddot{S}(\tau) + \varepsilon_0(1 - S^2)\dot{S}(\tau) + \omega_{\acute{e}}^2 S(\tau) + \vartheta_2 \ddot{\varphi}_{n,m}(\tau) = 0 \end{cases} \tag{2.38}$$

with
$$\varphi = \frac{r}{h_p}, \ \tau = \frac{t}{T_v}, \ T_v^2 = \frac{\varepsilon_{33}^s abL}{h_p}, \ V = v_0 S, \ D_{0nm} = \frac{T_v^2 D}{(\rho h + \rho_p h_p)}\left[\left(\frac{n\pi}{a}\right)^2 + \left(\frac{m\pi}{b}\right)^2\right]^2$$

$$\lambda_0 = \frac{\lambda T_v}{(\rho h + \rho_p h_p)}, \ c = (D_{0nm} + D_{p0nm}), \ \vartheta_0 = \frac{-8T_v^2(a^2 + b^2)v_0}{(\rho h + \rho_p h_p)h_p a^2 b^2}\vartheta, \ S = S_0\sqrt{\frac{-3b_0}{a_0}}V$$

$$\varepsilon_0 = \frac{T_v h_p a_0}{\varepsilon_{33}^s ab}, \ \vartheta_2 = \frac{-4h_p e_{31} h_{pc}(a^2 + b^2)S_0}{\varepsilon_{33}^s a^2 b^2}\sqrt{\frac{-3b_0}{a_0}}, \ \vartheta_1 = \frac{1}{S_0}\sqrt{\frac{-a_0}{3b_0}}\vartheta_{0n,m},$$

$$D_{p0_{nm}} = \frac{T_v^2 D_p}{(\rho h + \rho_p h_p)}\left[\left(\frac{n\pi}{a}\right)^4 + 2(\alpha + \gamma)\left(\frac{\pi nm}{ab}\right)^2 + \left(\frac{m\pi}{b}\right)^4\right].$$

where T_v is the proper period of the self-sustained electrical part.

It can be shown that the only equilibrium point $(0,0,0,0)$ from Eqs.2.38 is unconditionally unstable.

2.6 Experimental procedure based on analog circuits

2.6.1 Principle of analog simulation

The elementary operations of the analog simulation are direct consequences of physics laws [132]. Among these elementary operations, we have: summation, multiplication, integration and derivation. To design these operations, one needs to combine the basic electrical components such as resistors, capacitors, inductances and diodes with operational amplifier and analog multiplier.

✓ **Operations using Op-Amps**
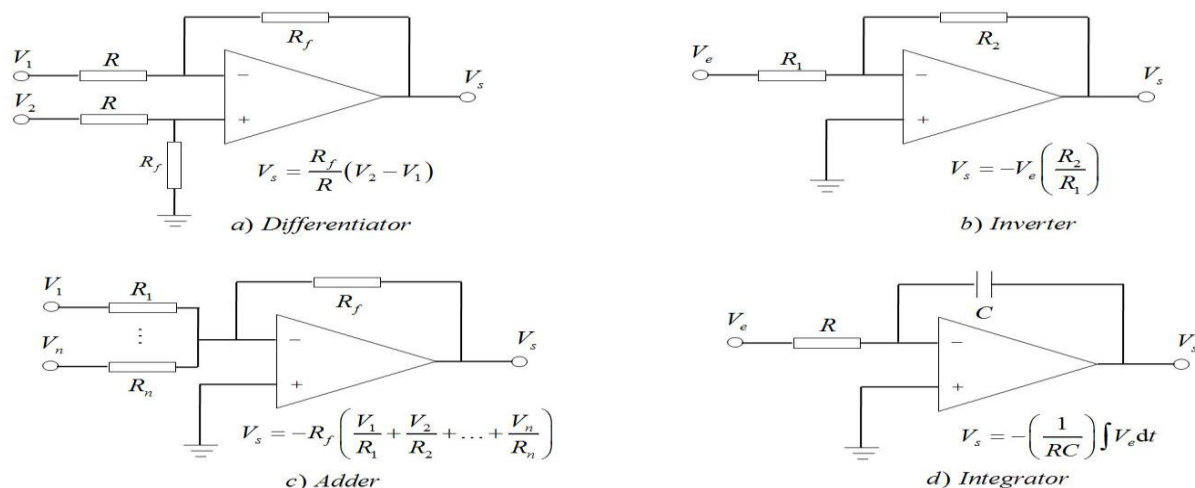
Figure 12: Some basic linear operations with Op-Amp.

✓ **Analog multipliers**

An analog multiplier is a device which takes two analog signals and produces an output which is their product. Such circuits can be used to implement the polynomial nonlinear functions. In the trade, one can find different types of analog multipliers. However, the most used is the AD633 analog device. The functional block diagram of AD633 is represented in Figure 11

(a)   (b)
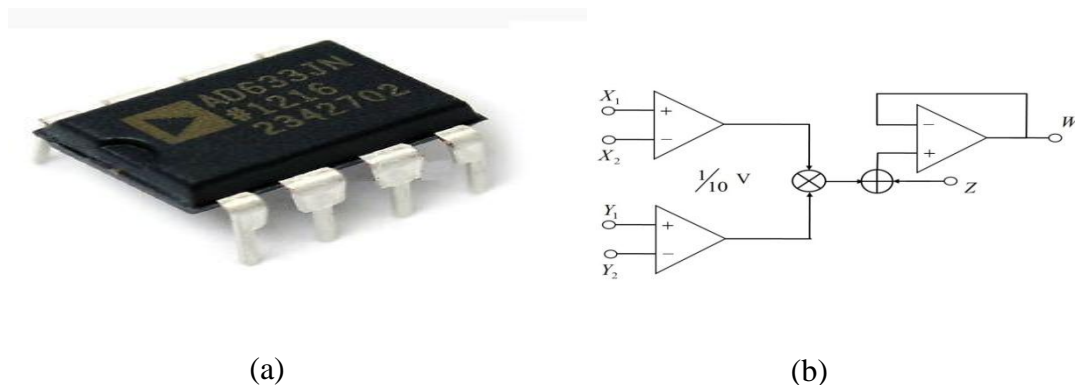
Figure 13: (a) Example of analog multiplier AD633JN and (b) electrical equivalent of the analog multiplier.

The multiplication of the voltage differences $(X_1 - X_2)$ and $(Y_1 - Y_2)$ over 10 Volts is added to the voltage Z and the sum is supplied through the output voltage W. The relation below gives its transfer function:

$$W = \frac{(X_1 - X_2)(Y_1 - Y_2)}{10} + Z$$

(2.39)

2.6.2   Electronics component and equipment

To design electronically the mathematical operations (addition, subtraction, derivatives, integrals and multiplications), one needs to combine the basic electrical components such as resistors, capacitors and inductances with operational amplifiers and analog multipliers.

2.6.2.2 Electronics components

The Operational Amplifier (Op-Amp) is an integrated circuit which amplifies an input through a very high gain. The Op-Amp contains several transistors. An operational amplifier has two input terminals used for polarization. It has also two inputs which are the non-inverting and inverting inputs. Figure 14(a) presents an example of operational amplifier. Finally it has one terminal output used to obtain the output signal (see figure 14(b)).

(a)   (b)
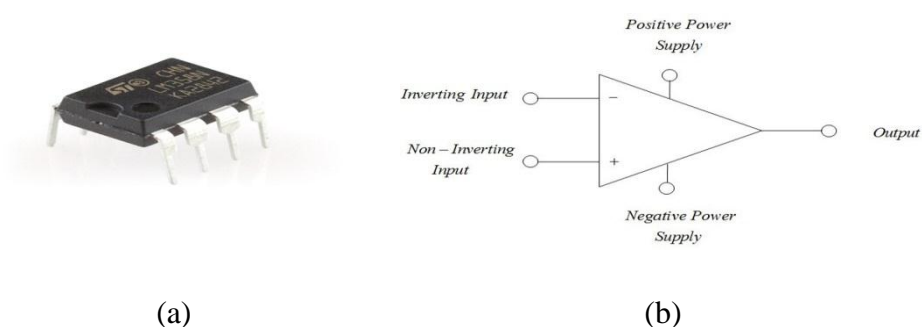
Figure 14: (a) Operational amplifier component and (b) electrical equivalent of the operational amplifier.

Other electronic components that we can have and generally linked to the Op-Amp are resistors and capacitors (see Figure 15).
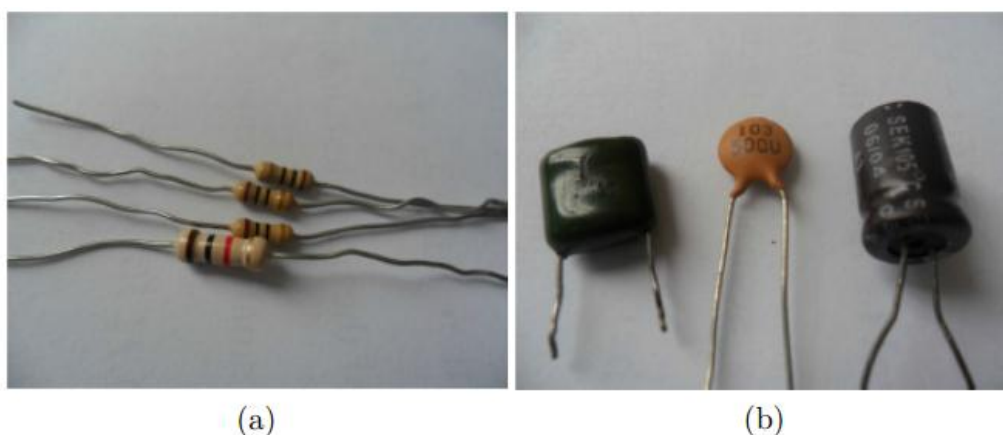
Figure 15: (a) Resistors and (b) Capacitors

2.6.2.3   Electronic equipment

Some measuring equipment will be necessary for the accomplishment of the experimental work.

a- Generators

A LFG of type Voltcraft (08112875), with a maximal frequency of 2 MHz sweep and 10 V for the voltage (see Figure 16(a)) and allowing to power our circuits.

b- Oscilloscopes

A Rigol oscilloscope of type DS1102E, of bandwidth 100 MHz (see Figure 16(b)) and allowing the visualization of oscillator electrical signals and electrical voltage across the piezoelectric plate.

c- Multimeters

An industrial Multimeter of type EXTECH (140508148) (figure 16 (c)) was used to measure the values of the components and to do the continuity test of our circuits.

d- Stabilized DC power

A stabilized DC power supply (PS2303) with two variable outputs (0-30 V) and a fixed output of 12 V (see Figure 16(d)), is used to bias the electronic components (Opamps and multipliers)

(a)

(b)

(c)

(d)

Figure 16: Some additional materials used: (a) LGF generator;; (b) Rigol oscilloscope; (c) Industrial MultiMeters; (d) DC power supply.

2.7   Conclusion

The aim of this chapter was to present the methods used in this thesis: the experimental characterization of a piezoelectric structures, mathematical formalisms, numerical methods and experimental procedure based on analog circuits. In the first part, methodology for the experimental characterization of piezoelectric structures and the modal approximation, Cardano's method and the Routh-Hurwitz criterion were presented. Then the numerical methods for the simulation of ODEs and PDEs were presented. Finally, we presented the analog electronic components, necessary for the construction of the different types of oscillators. All of these methods will be used in Chapter 3 which is devoted to the presentation of the main results of this thesis.

Chapter 3: Results and discussion

3.1 Introduction

This chapter deals with the presentation of the main results of the thesis. In section 3.2, the electrical characterization of piezoelectric plate is presented. Section 3.3 is devoted to the piezoelectric plate based self-excited oscillator. Section 3.4 is devoted to dynamical states of piezoelectric beam with nonlinear electric components and applications. In section 3.5, bursting like oscillations by a piezoelectric beam and applications is presented. Section 3.6 is devoted to the analysis of Self-sustained energy harvesting from micro beam under fluid flow. In section 3.7 will conclude the chapter.

3.2 Electrical characterization of piezoelectric plate

3.2.1 Frequency-impedance characteristics of a piezoelectric plate

As indicated in chapter 2 (figure 8), a piezoelectric plate has been placed in a circuit containing in series a resistor and a low frequency generator. Using a voltage of $1\,V$, we have varied the frequency of the LFG and measured the impedance of the piezoelectric plate. Figure 17 presents the variation of the impedance versus the frequency. One can observe anti-resonances (points where the impedance is relatively minimal) and resonances (points where the impedance is relatively maximal). More precisely three anti-resonances appear at 82 kHz, 115 kHz and 215 kHz while the three resonances appear at 95 kHz, 120 kHz and 235 kHz.
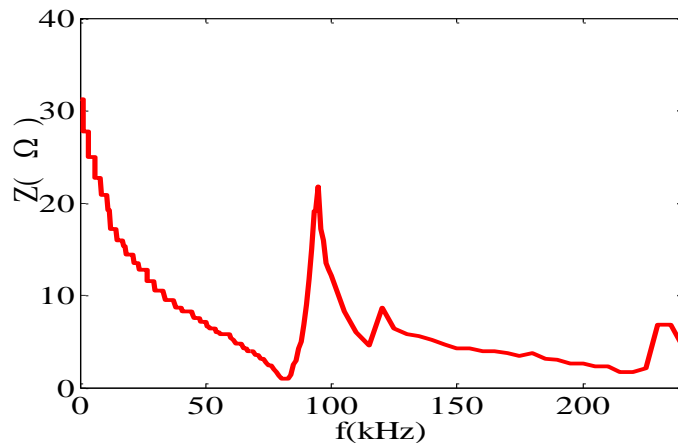
Figure 17: Experimental evolution of the impedance of the piezoelectric part as a function of frequency

3.2.2 Equivalent electric model of the piezoelectric plate

3.2.2.1 The Van Dyke model

As it known from the IEEE standard on piezoelectricity, the equivalent circuit of a piezoelectric plate is given in figure 3.

Considering this figure, equation 1.5 can be rewritten as:

$$|Z| = \frac{1}{2\pi \cdot C_0 \cdot f} \left[\frac{1 + Q_S^2 \left(\dfrac{f}{f_S} - \dfrac{f_S}{f} \right)^2}{1 + Q_P^2 \left(\dfrac{f}{f_P} - \dfrac{f_P}{f} \right)^2} \right]^{\frac{1}{2}} . \tag{3.1}$$

where,

- f_s correspond to a series resonance frequency for amplitude corresponding to the frequency at which the impedance Z at the terminals of the piezoelectric plate is at its first minimum Z_{min1},

- f_P correspond to a parallel resonance frequency corresponding to the frequency at which impedance Z at the terminals of the piezoelectric plate is at its first maximum Z_{max1},

From these values and the corresponding values of the impedance, one can determine the values of C_0, R_1 and C_1. At f_{s1}, $Z_{min1} = R_1$, while at f_{p1}, $Z = Z_{max1}$.

Thus after some simplification, one can write:

$$Z_{max1} = \frac{1}{2\pi C_0 f_{P1}} \left[1 + Q_{S1}^2 \left(\frac{f_{P1}}{f_{S1}} - \frac{f_{S1}}{f_{P1}} \right)^2 \right]^{\frac{1}{2}} \tag{3.2}$$

Since both quality factors are generally very large, it is possible to simplify the expression of Z_{max1} supposing:

$$Q_S \left(\frac{f_{P1}}{f_{S1}} - \frac{f_{S1}}{f_{P1}} \right) \gg 1 .$$

This leads to:

$$Z_{max1} = \frac{Q_{S1}}{2\pi C_0 f_{P1}} \left(\frac{f_{P1}}{f_{S1}} - \frac{f_{S1}}{f_{P1}} \right) . \tag{3.3}$$

Considering the fact that $Z_{min1} = R_1$ and taking into account the equality $(\frac{f_{p1}^2}{f_{s1}^2} - 1) f_{s1} f_{p1} = f_{P1}^2 (\frac{f_{P1}}{f_{S1}} - \frac{f_{S1}}{f_{P1}})$,

it appears that

$$Z_{max1} = \frac{1}{4\pi^2 Z_{min1} C_0^2 f_{P1}^2} . \tag{3.4}$$

Consequently,

$$
\begin{cases}
C_0 = \dfrac{1}{2\pi f_{P1}\sqrt{Z_{max1} \cdot Z_{min1}}} \\[3mm]
C_1 = \dfrac{\left(\dfrac{f_{P1}^{\;2}}{f_{S1}^{\;2}} - 1\right)}{2\pi f_{P1}\sqrt{Z_{max1} \cdot Z_{min1}}} \\[3mm]
L_1 = \dfrac{f_{P1}}{f_{P1}^{\;2} - f_{S1}^{\;2}} \cdot \dfrac{\sqrt{Z_{max1} \cdot Z_{min1}}}{2\pi}
\end{cases}
\qquad .
\tag{3.5}
$$

From the analysis conducted and considering the experimental curve of Figure 17, one arrives at the Table 3 which presents the calculated values of the electric components of the Van Dyke circuit.

Table 3: Parameter values of the electrical model equivalent at two branches

Electric component	C_0	R_1	L_1	C_1
Value	358.92 nF	1.00 Ω	30.70 μH	122.82 nF

From the values of Table 3, the real value of the Van Dyke's circuit impedance can be expressed in terms of frequency. Its frequency variation is then superposed to the one obtained experimentally (curve in blue in Figure 18).
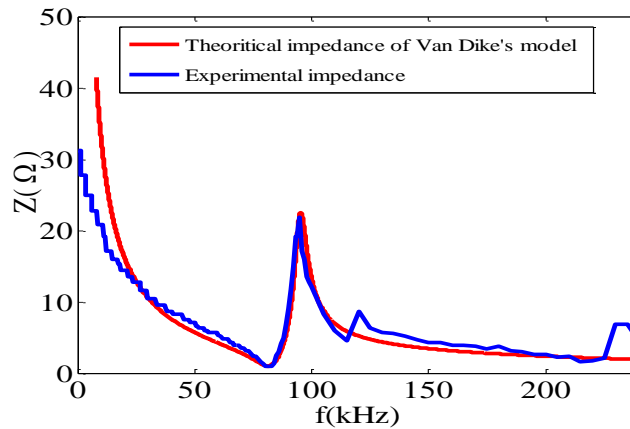
Figure 18: Superposition of the two impedances: Van Dyke's circuit impedance in red and the experimental curve in blue.

we observes a good agreement between the theoretical impedance and the one obtained experimentally for frequencies below the first resonance. Indeed, a perfect frequency

agreement between the two curves at the first anti-resonance at the frequency f_{S1} = 82 kHz and at the first resonance at the frequency f_{P1} = 96 kHz. But after the first resonance, the impedance from the Van Dyke's model decreases in a monotonous manner while the experimental result presents other resonances and anti-resonances. This might be explained by the fact that at large frequencies, the Van Dyke's model is limited in explaining the equivalent circuit of the piezoelectric plate.

3.2.2.2 Three parallel branches model

By adding a third RLC resonant branch, the equivalent model is presented in Figure 19
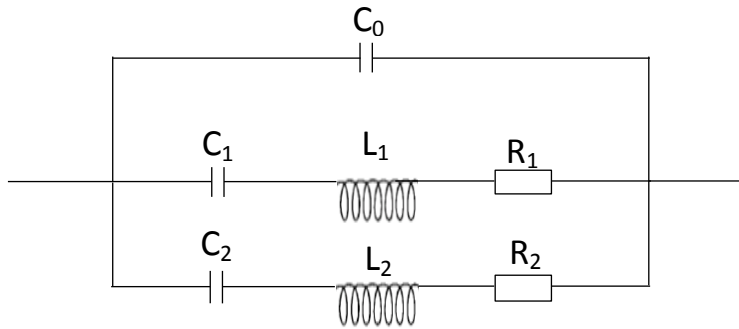
Figure 19: Electric equivalent model of piezoelectric plate with three branches.

The impedance of this equivalent circuit with three branches is given by the following expression:

$$|z'| = \frac{\left((R_1 R_2 - (L_1\omega - \frac{1}{C_1\omega})(L_2\omega - \frac{1}{C_2\omega}))^2 + (R_1(L_1\omega - \frac{1}{C_1\omega}) + R_2(L_2\omega - \frac{1}{C_2\omega}))^2 \right)^{\frac{1}{2}}}{\left[\begin{array}{l} (R_1 + R_2 - C_0\omega(R_1(L_2\omega - \frac{1}{C_2\omega}) + R_2(L_1\omega - \frac{1}{C_1\omega})))^2 + (-\frac{1}{\omega}(\frac{1}{C_1} + \frac{1}{C_2}) + \\ (\omega(L_1 + L_2) + C_0\omega(R_1 R_2 - (L_1\omega - \frac{1}{C_1\omega})(L_2\omega - \frac{1}{C_2\omega})))^2 \end{array} \right]^{\frac{1}{2}}} \quad (3.6)$$

Using some mathematical transformations and physics considerations (**see Appendix 1**), this model leads to the values of the electric components which are listed in Table 4.

Table 4: Parameters values of the new electric equivalent model of the piezoelectric plate

Electric component	$C_0(nF)$	$R_1(\Omega)$	$L_1(\mu H)$	$C_1(nF)$	$R_2(\Omega)$	$L_2(\mu H)$	$C_2(nF)$
Value	358.92	1.00	30.70	122.82	4.40	100.13	19.13

With the values in Table 3, we evaluate the shape of the impedance given in Eq. (3.6) versus the frequency and we superpose to the experimental curve. This appears in Figure 18.

And one notes the more accurate agreement for frequencies above the first resonant frequency.
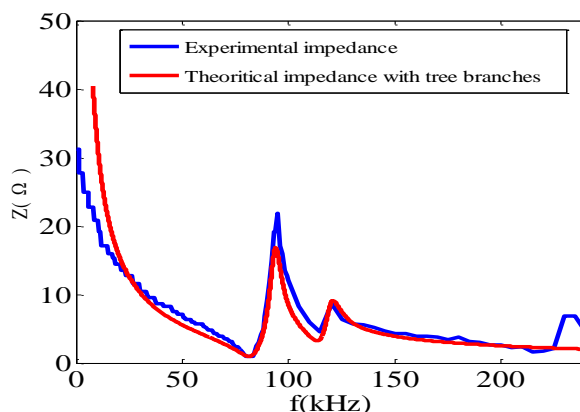
Figure 20: Impedance of the new equivalent model in red and the experimental results in blue.

But, despite this agreement, it is remarkable that there is a resonance in the experimental curve which is not explained by the new model. It is expected that the adding of new resonant branch will be more accurate.

3.2.2.3 Generalization

A generalization can be proposed as in Figure 21 where the number of branches depends on the frequencies range.
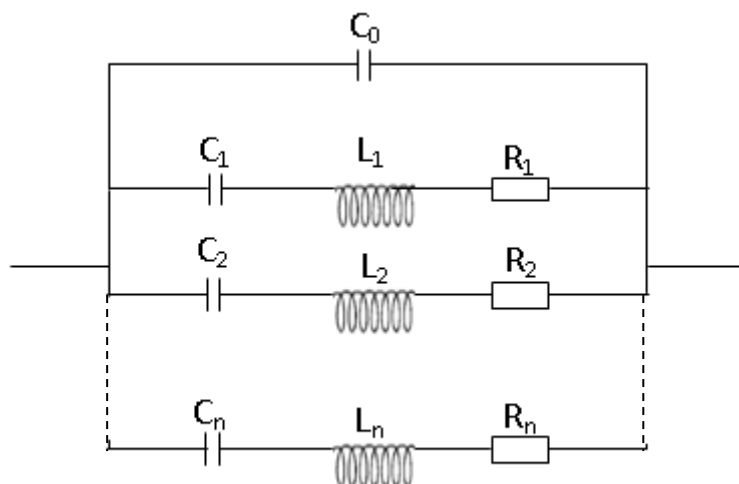
Figure 21: Generalized equivalent model with i parallel branches.

The model constituted of several *RLC* branches can be understood if one has in mind that submitting the piezoelectric plate to a sinusoidal electrical voltage will, as the results of the

reverse piezoelectric effects, create vibrations in the plate. These vibrations can be described by a 2-dimensional partial differential equation which can be converted into a set of modal differential equations. Each of these modal differential equations has its own resonant frequency [125].

Consequently the coupling with the electric part of the piezoelectric plate will lead to resonant states equivalent to electric resonant branches. The section below qualitatively confirms what is indicated here.

3.2.3 Vibrations modes justification of the impedance variation

To determine the impedance characteristics, we take n and m varying from 1 to 3 and write

$$r(x,y,t) = \sum_{n=1}^{3}\sum_{m=1}^{3} \varphi_{nm} \sin(\frac{n\pi x}{a})\sin(\frac{n\pi y}{b})$$ (3.7)

We stay at the center of the piezoelectric plate $\left(\frac{a}{2};\frac{b}{2};\tau\right)$. Witch would amount to writing Eq.(3.14) in the form :

$$\begin{aligned}
r\left(\frac{a}{2},\frac{b}{2},\tau\right) &= \varphi_{11}(t) - 2\times\varphi_{13}(t) + \varphi_{33}(t) \\
&= A_1(1,1)\cos\Omega\tau + A_2(1,1)\sin\Omega\tau - 2\times A_1(1,3)\cos\Omega\tau - \\
&\quad 2\times A_2(1,3)\sin\Omega\tau + A_1(3,3)\cos\Omega\tau + A_2(3,3)\sin\Omega\tau
\end{aligned}$$ (3.8)

And therefore

$$\begin{aligned}
v_r &= \left[B_1(1,1) + B_1(1,3) + B_1(3,1) + +B_1(3,3)\right]\cos\Omega\tau + \\
&\quad \left[B_2(1,1) + B_2(1,3)) + B_2(3,1) + B_2(3,3)\right]\sin\Omega\tau
\end{aligned}$$ (3.9)

$$\begin{aligned}
i_r &= \left[D_1(1,1) + D_1(1,3) + D_1(3,1) + D_1(3,3)\right]\cos\Omega\tau + \\
&\quad \left[D_2(1,1) + D_2(1,3) + D_2(3,1) + D_2(3,3)\right]\sin\Omega\tau
\end{aligned}$$ (3.10)

One gets the impedance for nine vibration modes defined by

$$Z(\Omega) = \frac{B}{D}$$ (3.11)

Where

$$B(\Omega) = \sqrt{\left[B_1(1,1) + B_1(1,3) + B_1(3,1) + B_1(3,3)\right]^2 + \left[B_2(1,1) + B_2(1,3) + B_2(3,1) + B_2(3,3)\right]^2}$$ (3.12)

$$D(\Omega) = \sqrt{\begin{array}{l}\left[D_1(1,1) + D_1(1,3) + D_1(3,1) + D_1(3,3)\right]^2 + \\ \left[D_2(1,1) + D_2(1,3) + D_2(3,1) + D_2(3,3)\right]^2\end{array}} \qquad (3.13)$$

Plotting this expression versus the frequency, one obtains Figures 20 which gives the frequency-impedance characteristics of the piezoelectric structure presented in Figure 8a.

From Figure 22 we can observe the phenomenon of anti-resonance and resonance of impedance characteristics as we observed experimentally. The appearance of a peak of resonance and anti-resonance is related to the mode of vibration chosen. More precisely, we have resonances at the frequencies, $17.94\,\text{kHz}$, $101.7\,\text{kHz}$, and $144.1\,\text{kHz}$. And for anti-resonances, $15.88\,\text{kHz}$, $99.73\,\text{kHz}$, $103.4\,\text{kHz}$, $143.3\,\text{Hz}$ and $145.2\,\text{kHz}$. Thus, the figure 22 explains that the resonant branches of the electric equivalent model of the piezoelectric plate are due to the vibration modes of the piezoelectric plate. To end this section, we mention that the intent here was only to have a qualitative agreement between the results obtained experimentally and those obtained from the modal approach of the plate dynamics.
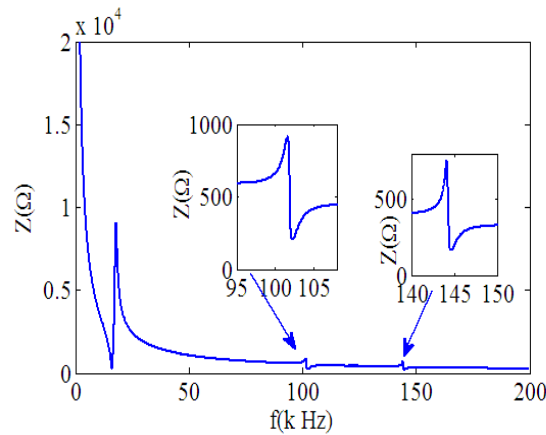
Figure 22: The frequency-impedance characteristics obtained from the vibration modes approach

In order to validate the proposed model, a direct numerical simulation of partial differential equation Eq (2.25) is explored using the method of lines [134-135]. The central finite difference formula is applied to discretize the nonlinear differential equation with the appropriate space step dx.

3.2.3.1 Numerical simulation of the PDEs

For obtaining a numerical solution of Eqs (2.25), we use the finite difference scheme [136-137] by applying the central spatial and temporal discretization with space and temporal steps adequately chosen to avoid numerical instability.
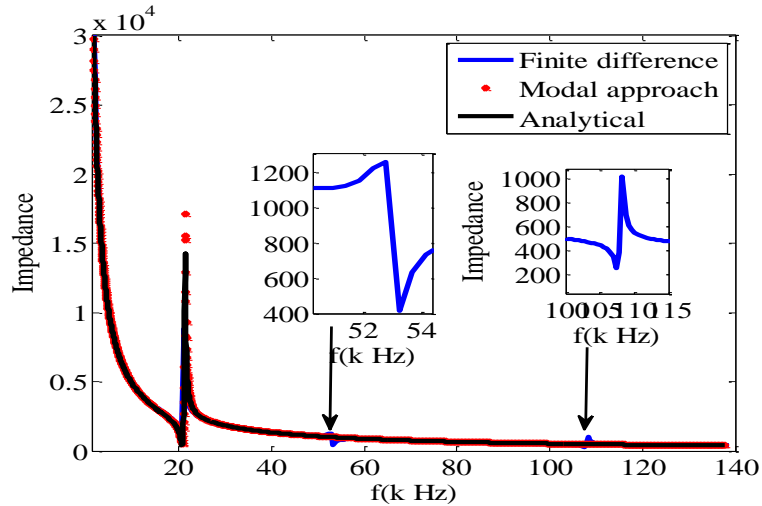
Figure 23: The frequency-impedance characteristics obtained from the vibration modes approach: in blue the finite difference method, in red the modal approach and in black the analytical method.

In Figure 23 we have plotted the evolution of the amplitude of impedance in function of the excitation frequency. There is a fairly good agreement of first pic with simulation of modal equation, analytical approach and simulation of partial differential equation. But when the frequency is increased, one observes the appearance of other pic when the full partial differential equation is simulated numerically using the finite difference scheme as described above.

3.3 Piezoelectric plate based self-excited oscillator

As indicated in the introduction, one of the applications of piezoelectric plates is the development of an electronic oscillator or its corresponding actuator with periodic deformation (lengthening or shortening). These oscillators may be set into motion because of an external periodic voltage. However, thanks to some special electronic components, self-sustained oscillations can take place. This section considers such self-sustained oscillations having the piezoelectric plate as one component of the circuit.

3.3.2 Electrical equivalent and self-sustained oscillations

The corresponding electronic circuit is presented in Figure 24 and is constituted of three parallel branches. The first one is an electronic setup behaving as a nonlinear resistor having

both positive and negative slopes. This is the usual electronic setup of nonlinear resistor used in Van der Pol oscillators. Its $I - V$ characteristics is given by the following equation

$$i = a_0 V + b_0 V^3 \qquad (3.14)$$

with $a_0 \prec 0$ and $b_0 \succ 0$.
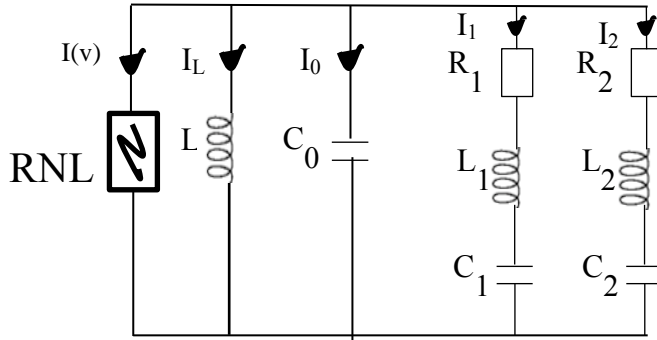
Figure 24: Electronic circuit of a piezoelectric plate based self-sustained oscillator.

The second branch is made of a coil with inductance L. Moreover, the third branch is just the piezoelectric plate represented by its electric equivalent circuit.

By applying Kirchhoff's laws in Figure 24 and after some mathematical transformations, it is found that the circuit is described by the following set of differential equations.

$$\begin{cases} \ddot{x} - (A - Bx^2)\dot{x} + x + D_1\dot{x}_1 + D_2\dot{x}_2 + E_1 x_1 + E_2 x_2 = 0 \\ \ddot{x}_1 + \theta_1\dot{x}_1 + \omega_1^2 x_1 - \beta x = 0 \\ \ddot{x}_2 + \theta_2\dot{x}_2 + \omega_2^2 x_2 - \gamma x = 0 \end{cases} \qquad (3.15)$$

Where the dot over a variable is the derivative with respect to the dimensionless time $\tau = \omega_0 t$ (t being the time), $x = \dfrac{V}{V_0}, x_1 = \dfrac{V_1}{V_0}, x_2 = \dfrac{V_2}{V_0}$. V, V_1 and V_2 are respectively the voltages across the capacitors C_0, C_1 and C_2. The coefficients in equation (3.17) are given by

$$\omega_0^2 = \frac{1}{C_0}(\frac{1}{L} + \frac{1}{L_1} + \frac{1}{L_2}); A = \frac{a}{C_0\omega_0}; B = \frac{3bV_0^2}{C_0\omega_0}; D_1 = \frac{R_1 C_1}{L_1 C_0\omega_0}; D_2 = \frac{R_2 C_2}{L_2 C_0\omega_0};$$

$$E_1 = \frac{1}{L_1 C_0\omega_0^2}; E_2 = \frac{1}{L_2 C_0\omega_0^2}; \theta_1 = \frac{R_1}{L_1\omega_0}; \omega_1^2 = \frac{1}{L_1 C_1\omega_0^2}; \qquad (3.16)$$

$$\beta_1 = \frac{1}{L_1 C_1\omega_0^2}; \theta_2 = \frac{R_2}{L_2\omega_{0b}}; \omega_2^2 = \frac{1}{L_2 C_2\omega_0^2}; \beta_2 = \frac{1}{L_2 C_2\omega_0^2}.$$

The only equilibrium point from equation (3.15) is $(0,0,0,0,0,0)$. The characteristics equation obtained from this equilibrium point is

$$a_0 \lambda^6 + a_1 \lambda^5 + a_2 \lambda^4 + a_3 \lambda^3 + a_4 \lambda^2 + a_5 \lambda + a_6 = 0 \quad . \tag{3.17}$$

Where the coefficients a_i are given below

$$
\begin{aligned}
a_0 &= 1 \\
a_1 &= \theta_1 + \theta_2 - A \\
a_2 &= -A(\theta_1 + \theta_2) + \theta_1 \theta_2 + \omega_1^2 + \omega_2^2 + 1 \\
a_3 &= -A(\theta_1 \theta_2 + \omega_1^2 + \omega_2^2) + \theta_1 \omega_2^2 + \theta_2 \omega_1^2 - \alpha_1 \beta - E_2 \gamma + \theta_1 + \theta_2 \\
a_4 &= -\gamma_b(E_2 + \theta_1 D_2) + \omega_2^2(\omega_1^2 - A\theta_1 + 1) + \theta_2(\theta_1 - A\omega_1^2) - \beta(\theta_2 D_1 + E_1) \\
a_5 &= -\gamma(\theta_1 E_2 + D_2 \omega_1^2) - \omega_2^2(A\omega_1^2 + D_1 \beta - \theta_1) + \theta_2(\omega_1^2 - E_1 \beta) \\
a_6 &= -E_1 \beta \omega_2^2 - E_2 \gamma \omega_1^2 + \omega_1^2 \omega_2^2
\end{aligned}
\tag{3.18}
$$

Using the Routh-Hurwitz criterion [126,127], it can be demonstrated that this single equilibrium point is unconditionally unstable. From the numerical simulation, it is found that any trajectory starting at the neighborhood of this point leads to a limit cycle whose shape depends on the values of the system parameters (e.g; on the value of A). For instance, Figure 24 presents the temporal signal and the phase portrait for x, obtained for two values of A.

	Temporal evolution by use equivalent electrical circuit	Temporal evolution by use laws of plate theory	Phase portrait with equivalent electrical circuit
$A = 0.1$			
$A = 1.74$			
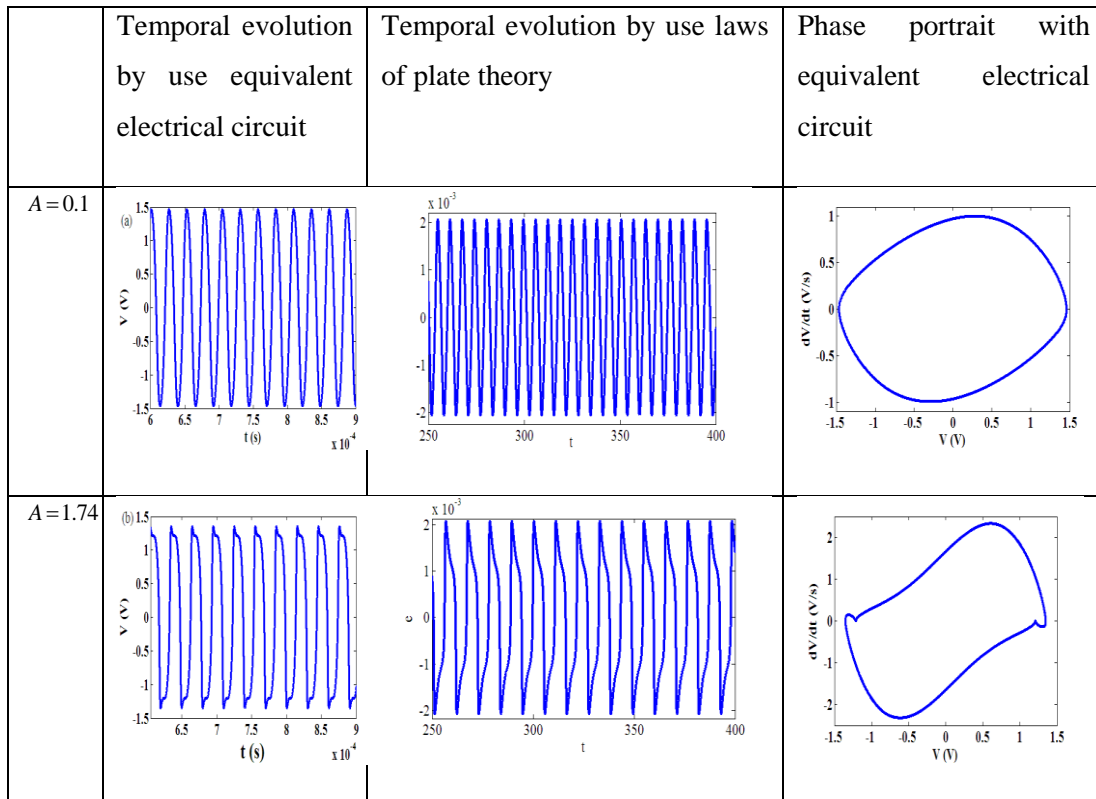
Figure 25: Time traces and phase portrait of the voltage x across the piezoelectric plate for

two values of A for $\omega_0^2 = 4.31 \times 10^5$; $B = 0.00077$; $D_1 = 0.0258$; $D_2 = 0.00542$; $E_1 = 0.48644$; $E_2 = 0.1493$; $\theta_1 = 0.075$; $\theta_2 = 0.1018$; $\beta_1 = 1.192$; $\omega_1 = 1.192$; $\omega_2 = 1.673$ and $\beta_2 = 1.673$.

To verify the theoretical results, we have conducted an experimental test with electronic circuit presented in Figure 26.

3.3.3 Experimental signature of the self-sustained oscillations

The circuit is constituted of three parallel branches: nonlinear resistance block, coil of inductance L and the piezoelectric plate.
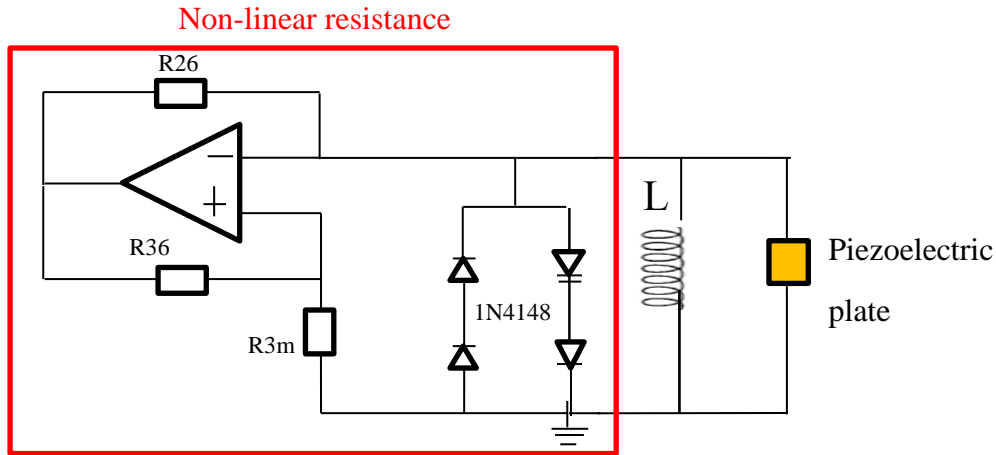
Figure 26: Self-sustained electronic oscillator made of a piezoelectric plate

From Figure 26, it is found that the coefficients a_0 and b_0 in Eq. (3.19) are approximated by the following expressions derived from the diode I-V characteristics [138].

$$a_0 = -\left[\frac{R_{36}}{R_{3m}R_{26}} - \frac{2i_0}{nV_0} \right] \text{ and } b_0 = \frac{i_0}{3V_0^3 n^3} \tag{3.20}$$

where $i_0 = 100 \ \mu A$, is the reverse saturation current in nonlinear resistance and $V_0 = 26 \ mV$, is the thermal tension. For a_0 to be positive, the following condition should be satisfied

$$R_{36} > \frac{2 \cdot i_0 \cdot R_{3m} \cdot R_{26}}{nV_0} \tag{3.19}$$

From the expression of A Eq. (3.16) and that of the coefficient a_0 above, one notes that A can be varied experimentally by adjusting the values of the resistances R_{26}, R_{36} and R_{3m}. However, we choose to fix $R_{26} = 64 \ \Omega$, $R_{3m} = 641 \ \Omega$, and vary only R_{36}. Figure 27 presents the experimental time traces of the voltage across the piezoelectric plate. As found in the

theoretical results in Figure 27, the voltage temporal shape moves from the well-known periodic sinusoidal oscillations to shapes close to relaxation oscillations when A or R_{36} increases. At the same time, it is found that the frequency is a decreasing function of A.
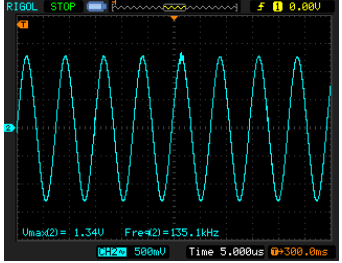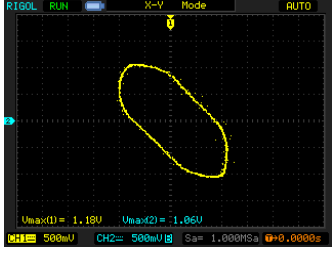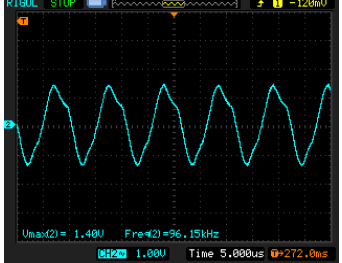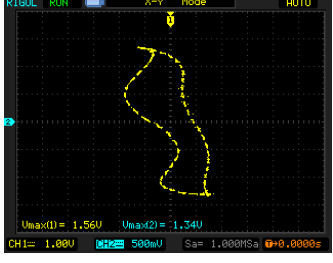
R_{36} ou A	Temporal variation of the voltage across the piezoelectric plate	Phase portrait
$R_{36} = 4150\ \Omega$ $A = 0.1$		
$R_{36} = 9150\ \Omega$ $A = 1.74$		

Figure 27: Time plot and phase portrait of the voltage across the piezoelectric plate

3.3.4 Results from the partial differential equations model

3.3.4.1 Numerical results

Eq. (2.37) has been solved numerically and the time traces of the mechanical vibration are presented in Figure 28. It is found that the electrical signal presents the classical sinusoidal shape for $\varepsilon_0=0.1$ (not shown) while the mechanical vibration has a shape similar to that of mixed modes oscillations where one finds high frequency small amplitude oscillations superimposed on low frequency high amplitude oscillations. By increasing the parameter of the VdP oscillator in order to subject the piezoelectric plate to relaxation oscillations ($\varepsilon_0=4$), Figure 28 shows that the mechanical arm still exhibits mixed mode oscillations, but with larger amplitudes.
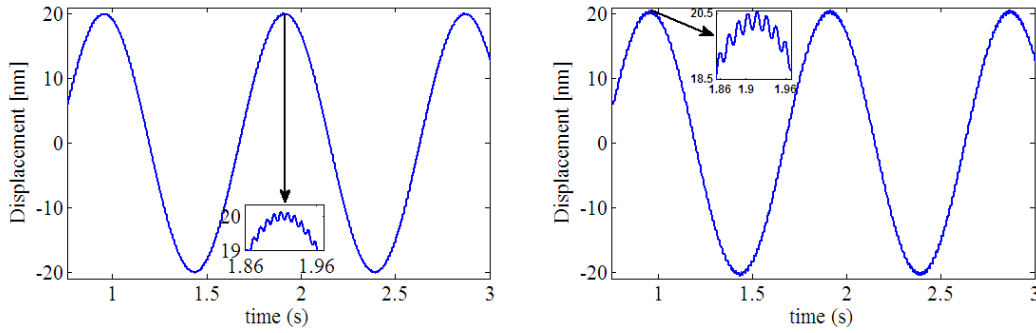
Figure 28: Temporal evolution of the plate deflection for   (left curve) and for $\varepsilon_0 = 4$ (right curve) with an inductance coil $41\ \mu H$.

3.4 Dynamical states of piezoelectric beam with nonlinear electric components and applications

3.4.2 Piezoelectric beam powered by a circuit with a nonlinear capacitance for production of periodic and chaotic ultrasounds

In this subsection, nonlinear dependence of the voltage on electrical charge is use to constitute a circuit for powered a piezoelectric beam.

3.4.2.1 Physical structure and its equations

Consider an Euler–Bernoulli mechanical beam of width $b = 50 \times 10^{-5}$ m, thickness $h_s = 5 \times 10^{-5} m$, length $l = 300 \times 10^{-5}$ m, density $\rho = 7165$ kg/m^3, bending stiffness $E_s I$ (where $E_S = 129 \times 10^9$ Pa and $I = 5.21 \times 10^{-18}$ m^4) and the viscosity $\lambda = 400$ Ns/m (see Figure 29). Using the laws of mechanics, the equation of motion of the beam is given by

$$\rho h_s b \frac{\partial^2 w}{\partial t^2} + \lambda \frac{\partial w}{\partial t} + E_s I \frac{\partial^4 w}{\partial X^4} = 0 \tag{3.20}$$

Now, consider Figure 29 which is a simply uniform composite Euler–Bernoulli beam consisting of a PZT layer of thickness $h_p = 200 \times 10^{-6}$ m, Young modulus $E_p = 66 \times 10^9$ Pa density $\rho_p = 7800$ kg/m^3.

The beam is also connected to an electrical circuit through the electrodes, which bracket the PZT layer. The electrodes are assumed to be perfectly conductive and they cover the entire surface of the PZT at the bottom and at the top so that the electric field is uniform over the length of the beam. Subjected to an external electric field whose direction is that of the

polarization of the PZT, it lengthens. If the direction of the external electric field is reversed, it becomes shorter. Once associated with a deformable structure, the whole flexes because the substructure which is associated with PZT can neither lengthen nor shorten. The nonlinear electrical circuit consists of a resistive load in series with an inductance, a capacitor with nonlinear capacitance and an external applied voltage ($U(t) = u_0 \sin \omega t$).
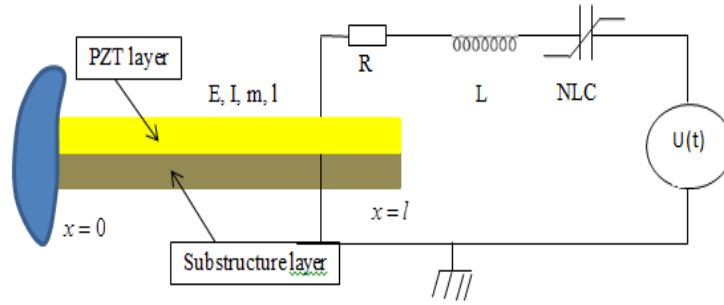
Figure 29: Piezoelectric cantilever system connected to a nonlinear electric circuit.

The voltage charge characteristics of the NLC satisfies the following

$$V_C(q) = \alpha q + \beta q^3 \tag{3.21}$$

where α and β are positive parameters.

Using mechanics and electricity laws, the piezoelectric cantilever beam connected to nonlinear circuit is described by the following set of differential equations (**see Appendix 2**)

$$
\begin{cases}
\rho_{total} b \dfrac{\partial^2 w}{\partial t^2} + \lambda \dfrac{\partial w}{\partial t} + E'I \dfrac{\partial^4 w}{\partial X^4} - \dfrac{\vartheta}{C_p}\left(\dfrac{d\delta(X)}{dX} - \dfrac{d\delta(X-l)}{dX} \right) q = 0 \\[4mm]
L \dfrac{d^2 q}{dt^2} + R \dfrac{dq}{dt} + \dfrac{q}{C_0} + b_3 q^3 + \dfrac{\varepsilon_{33}^s}{\varepsilon_0 C_p} q - \dfrac{d_{31} E_p h_{pc} h_p}{\varepsilon_0} \dfrac{\partial^2 w}{\partial X^2} = u_0 \sin \omega t
\end{cases}
\tag{3.22}
$$

with the following boundaries conditions $w(0,t) = \dfrac{\partial w(0,t)}{\partial X} = \dfrac{\partial^2 w(l,0)}{\partial X^2} = \dfrac{\partial^3 w(l,0)}{\partial X^3} = 0$

In order to put the equations in a dimensionless form, we use the following quantities:

$$w(X,t) = h_{sp} y(x,\tau), \quad \chi = \dfrac{q}{q_0}, \quad \tau = \dfrac{t}{T_n}, \quad \mathrm{x} = \dfrac{X}{l},$$

where $h_{sp} = h_s + h_p$ and $T_n = k_n^2 \sqrt{\dfrac{l^4 \rho_{total}}{E'I}}$, the undamped natural period of the nth mode.

The system of equations in dimensionless form is thus as follows:

$$\begin{cases} \dfrac{\partial^2 y}{\partial \tau^2} + \alpha_1 \dfrac{\partial y}{\partial \tau} + \alpha_{22} \dfrac{\partial^4 y}{\partial x^4} + \alpha_{33} \left(\dfrac{d\delta(x)}{dx} - \dfrac{d\delta(x-1)}{dx} \right) \chi(\tau) = 0 \\[4mm] \dfrac{d^2 \chi}{d\tau^2} + b_1 \dfrac{d\chi}{d\tau} + b_2 \chi + b_3 \chi^3 + b_{44} \dfrac{\partial^2 y}{\partial x^2} = E \sin \omega\tau \end{cases}$$ (3.23)

with the associated dimensionless boundary conditions

$$y(0,\tau) = \frac{\partial y(0,\tau)}{\partial x} = \frac{\partial^2 y(1,0)}{\partial x^2} = \frac{\partial^3 y(1,0)}{\partial x^3} = 0.$$

The dimensionless parameters appearing in Eqs. (3.33) are defined as follows:

$$\alpha_{33} = \frac{-\vartheta q_0}{C_p}; b_1 = \frac{TR}{L}; b_2 = \frac{T^2}{L}\left(\frac{1}{C_0} + \frac{\varepsilon_{33}^s}{C_p h_p} \right); b_3 = \frac{T^2 \beta}{L}; b_{44} = -\frac{T^2 d_{31} E_p h_{pc} h_{sp} h_p}{q_0 L l^2 \varepsilon_0}; E_\varsigma = \frac{T^2 u_0}{q_0 L}$$

3.4.2.2 Modal equation analysis

Assuming that the beam response is composed or an infinite number of oscillation modes, the displacement y can be decomposed in

$$y(x,\tau) = \sum_{n=0} \Theta_n(\tau) \varphi_n(x)$$ (3.24)

where $\Theta_n(\tau)$ is the time-dependent modal-displacement for the mode n and $\varphi_n(x)$ is the position dependent modal shape. Substituting Eq. (3.24) in the associated beam equation $\dfrac{\partial^2 y}{\partial \tau^2} + \dfrac{\partial^4 y}{\partial x^4} = 0$ and taking in to account the boundary conditions, one obtains for the nth mode the followings expression [141]:

$$\varphi_n(x) = C_n \left[\cosh \Upsilon_n x - \cos \Upsilon_n x - \sigma_n (\sinh \Upsilon_n x - \sin \Upsilon_n x) \right]$$ (3.25)

Where Υ_n is the dimensionless frequency numbers obtained from the characteristic equation given by

$$1 + \cos \Upsilon \cosh \Upsilon = 0$$ (3.26)

And σ_r is expressed as

$$\sigma_r = \frac{\sinh \Upsilon_r - \sin \Upsilon_r}{\cosh \Upsilon_r - \cos \Upsilon_r}$$ (3.27)

Substituting Eq. (3.24) in to the first equation of system (3.22), multiplying by $\varphi_n(x)$, integrating over the length of the beam and using the optionality of eigen functions, we get the following set of linear ordinary differential equations

$$\frac{d^2\Theta_n}{d\tau^2} + \alpha_1 \frac{d\Theta_n}{d\tau} + \alpha_2\Theta_n + \alpha_3\chi(\tau) = 0 \qquad (3.28)$$

Considering the second equation of the system, multiplying by $\varphi_n(x)$, integrating over the length of the beam, we obtain

$$\frac{d^2\chi}{d\tau^2} + b_1 \frac{d\chi}{d\tau} + b_2\chi + b_3\chi^3 + b_4\Theta_n = E\sin\Omega\tau \qquad (3.29)$$

Consequently, the modal equations of the PZT beam deflection are described by the following set of coupled differential equations

$$\begin{cases} \dfrac{d^2\Theta_n}{d\tau^2} + \alpha_1 \dfrac{d\Theta_n}{d\tau} + \alpha_2\Theta_n + \alpha_3\chi(\tau) = 0 \\ \dfrac{d^2\chi}{d\tau^2} + b_1 \dfrac{d\chi}{d\tau} + b_2\chi + b_3\chi^3 + b_4\Theta_n = E\sin\Omega\tau \end{cases} \qquad (3.30)$$

with $\alpha_2 = \alpha_{22}I_1$; $\alpha_3 = \alpha_{33}I_2$ and $b_4 = b_{44}I_3$,

where $I_1 = \dfrac{\displaystyle\int_0^1 \varphi_n(x)\dfrac{d^4\varphi_n(x)}{dx^4}dx}{\displaystyle\int_0^1 \varphi_n^2(x)dx}$; $I_2 = \dfrac{\displaystyle\int_0^1 \varphi_n(x)\left(\dfrac{d\delta(x)}{dx} - \dfrac{d\delta(x-1)}{dx}\right)dx}{\displaystyle\int_0^1 \varphi_n^2(x)dx}$; $I_3 = \dfrac{\displaystyle\int_0^1 \dfrac{d^2\varphi_n(x)}{dx^2}dx}{\displaystyle\int_0^1 \varphi_n(x)dx}$.

In references [142-143], the authors compared the result obtained from a finite difference simulation of the partial differential equations similar to Eqs. (3.23) to those from the one-mode approximation in the case of self-sustained electromechanical system with clamped-free cantilever arm and the conclusive remark was that the fundamental mode is able to capture all the essential behavior of the system effectively and accurately for some selected frequency range. For this reason, in our analysis, we consider only the fundamental mode of vibration, assuming that, higher modes have negligible effects on the system response.

3.4.2.3 Dynamical behaviors and actuation purpose

The values of other parameters of the piezoelectric system used in this thesis are presented in Table 5 [144].

Table 5: Geometric, material and electro-mechanical parameters of the substructure and of the piezoelectric layer.

Coefficients	Values	Coefficients	Values
$\varepsilon_{33}^{S}(\text{nF/m}^2)$	9.57	$R(\Omega)$	500
$L(mH)$	50	$C_0(nF)$	15

a- Oscillation states

Eqs. (3.23) present in the absence of the input voltage $U(t)$, a single stationary point $(\Theta = 0, \ \chi = 0, \ \dfrac{d\Theta}{d\tau} = 0, \ \dfrac{d\chi}{d\tau} = 0)$ which is stable. The presence of the sinusoidal input gives rise to oscillatory steady-states that can be approximated by using the harmonic balance method [34] of the form $\Theta(\tau) = B\sin(\Omega\tau - \varphi_1)$ and $\chi(\tau) = A\sin(\Omega\tau - \varphi_2)$. By replacing these relations in to Eqs. (3.43), equating the sine and cosine terms separately to find the amplitudes A and B, we obtain the following equations:

$$a_1 A^6 + a_2 A^4 + a_3 A^2 - GE = 0 \qquad (3.31)$$

$$B^2 = \frac{a_3^2}{G} A^2 \qquad (3.32)$$

The coefficients a_i and G are given as:

$$a_1 = \frac{9}{16} b_3^2 \left[\left(1 - \Omega^2\right)^2 + \alpha_1 \Omega^2 \right]$$

$$a_2 = \begin{bmatrix} \frac{3}{2} b_3 \left(1 - \Omega^2\right)^2 (b_2 - \Omega^2) - \frac{3}{2} b_3 \left(1 - \Omega^2\right)^2 + (\alpha_1\Omega^2 b_1 + \alpha_3 b_4) + \frac{3}{2} b_3 (\alpha_1\Omega)^2 \left(b_2 - \Omega^2\right) + \\ \frac{3}{2} \Omega b_1 \left(1 - \Omega^2\right) - \alpha_3 b_4 \alpha_1 \Omega b_3 \end{bmatrix} \qquad (3.33)$$

$$a_3 = \begin{bmatrix} \left(1 - \Omega^2\right)^2 (b_2 - \Omega^2)^2 - 2b_3 \left(1 - \Omega^2\right)(b_2 - \Omega^2)(\alpha_1\Omega^2 b_1 + \alpha_3 b_4) + (\alpha_1\Omega^2 b_1 + \alpha_3 b_4)^2 + \\ (\alpha_1\Omega)^2 \left(b_2 - \Omega^2\right)^2 + 2\Omega b_1 \left(1 - \Omega^2\right) - \alpha_3 b_4 \alpha_1 \Omega\left(b_2 - \Omega^2\right) + \left[\Omega b_1 \left(1 - \Omega^2\right) - \alpha_3 b_4\right]^2 \end{bmatrix}$$

$$G = \left[\left(1 - \Omega^2\right)^2 + \left(a_1\Omega\right)^2 \right]$$

Figure 30 presents the frequency curves of A and B obtained analytically (Eq. 3.33) and numerically by solving Eq. (3.30) using the fourth order Runge-Kutta algorithm. One observes the anti-resonance peak in the electrical part and resonance peak in the mechanical part at $\Omega = 3.95\ \text{MHz}$. We can also see that, in the electrical part, two resonance peaks appear at $\Omega = 3.16\ \text{MHz}$ and $\Omega = 4.93\ \text{MHz}$.
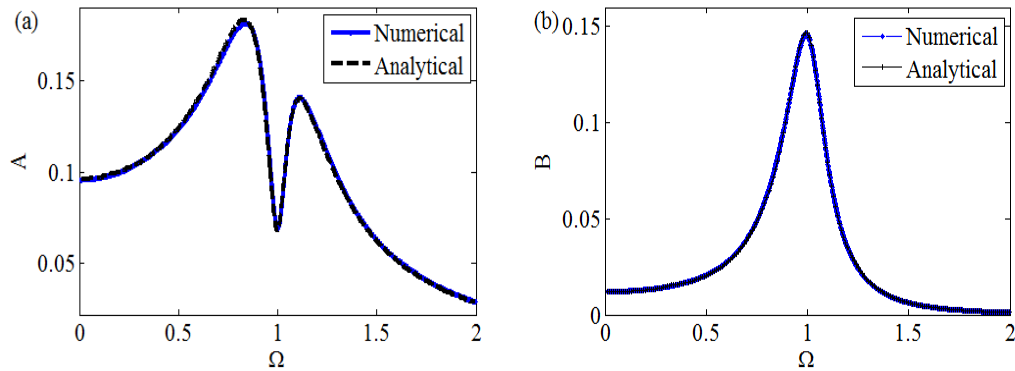
Figure 30: Amplitudes of electrical part (a) and mechanical part (b) as function of the normalized frequency. Curve of harmonic balance approximation (black) and curves from the direct numerical simulation of modal's equations (blue).

b- Chaotic behavior

The aim here is to use the Runge Kutta algorithm to solve numerically the dimensionless differential Eqs. (3.33) and mark the regions where the system appears periodic and chaotic. The bifurcation and Lyapunov exponent diagrams are used.

In Figure 31, the bifurcation diagram is plotted in the term of dimensionless deflection Θ, dimensionless electrical charge χ and the control parameter is the dimensionless voltage E.
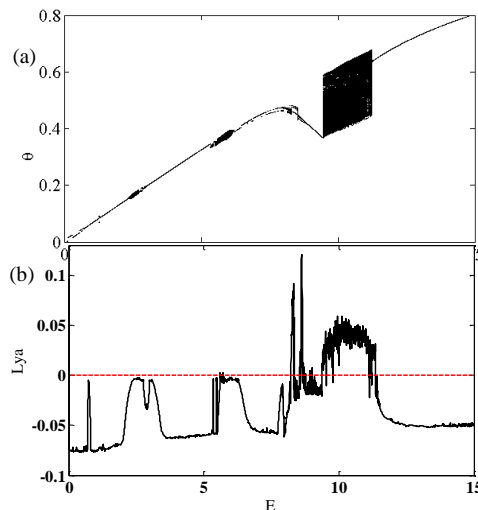
Figure 31: Bifurcation diagram (a) and Lyapunov exponent (b) against with the parameter of table 5.

As E increases, from $E \in \{[0; 2.397[\cup]3.057; 5.592[\cup]8.612; 9.392[\cup]11.36; 15.00]\}$, the structure oscillates and generates periodic ultrasounds. For $E \in \{]2.397; 3.057[\cup]5.592; 6.265[\}$, these ultrasounds are multi-periodic. However, when $E = 8.315$, $E = 8.665$ and $E \in [9.392; 11.36]$, chaotic ultrasounds appear.

3.4.3 Electromechanical device with a ferro resonant inductor

The aim of this subsection is to analyze the dynamics of a piezoelectric beam powered by a RLC series circuit with a ferromagnetic core inductor.

3.4.3.1 Electromechanical equations

Figure 32 presents the system under study. r is the resistance of the inductor and R is an additional resistor needed both to reduce the amplitude of current through the inductor.
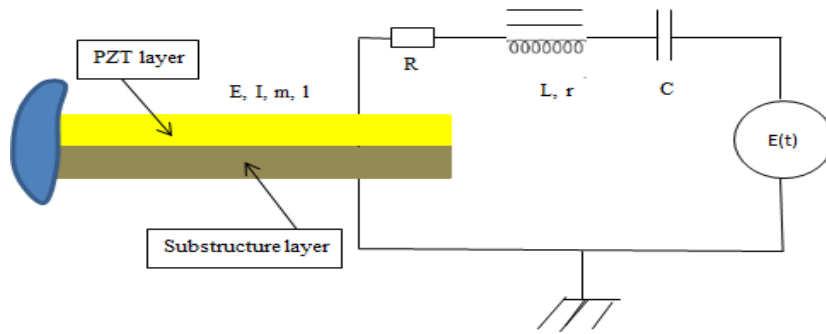
Figure 32: System with ferromagnetic core inductor.

The inductance of an inductor that contains a ferromagnetic material is given by the following mathematical expression [143]

$$L = \frac{\mu_0 N^2 A_L}{l_1} + \frac{B_s NA}{i} \tanh\left(\frac{\alpha Ni}{2l_1} - \frac{\sigma}{2}\right) \tag{3.34}$$

with $\sigma = \beta \, sign\left(\dfrac{di}{dt}\right)$

There are nine parameters appearing in Eq. (3.45) that are briefly presented below (for more detailed definitions, see [144]). B_s is the saturation flux density, A and l_1 are respectively the cross sectional area and the average length of the magnetic material. N is the number of turns, μ_0 is the permeability of the free space, i is the current through the winding.

Parameters α and β are function of the remanence (B_r), the coercive magnetic field (H_c) and the saturation flux density B_s, as mathematically defined below:

$$\alpha = \frac{1}{H_c}\ln\left(\frac{B_s + B_r}{B_s - B_r} \cdot \frac{B_s - \mu_0 H_c}{B_s + \mu_0 H_c}\right) \text{ and } \beta = \ln\left(\frac{B_s + B_r}{B_s - B_r}\right) \tag{3.35}$$

Proceeding as in the preceding section, equations (18) are obtained.

$$\begin{cases} \dfrac{d^2\Theta}{d\tau^2} + \alpha_1\dfrac{d\Theta}{d\tau} + \alpha_2\Theta + \alpha_4 z(\tau) = 0 \\[2mm] \left[(1-\xi) + \dfrac{2\xi}{1+\cosh(\chi - \sigma)}\right]\dfrac{d\chi}{d\tau} + \beta_1\chi + \beta_2 z + \beta_3\Theta = E_{B_s}\sin\Omega\tau \\[2mm] \dfrac{dz}{d\tau} = \gamma\chi \end{cases} \tag{3.36}$$

With
$$I_0 = \frac{l_1}{\alpha N}; L_0 = \frac{\mu_0 N^2 A}{l_1}\left(1 + \frac{B_s\alpha}{\mu_0}\right); \xi = \frac{B_s\alpha}{\mu_0 + B_s\alpha}; \alpha_4 = \frac{-\alpha_{33}u_0 C}{C_p}; \beta_1 = \frac{T_s R}{L_0};$$
$$\beta_2 = \frac{T_s}{L_0 I_0}\left(1 + \frac{\varepsilon_{33}^S C}{\varepsilon_0 C_p}\right); \beta_3 = \frac{T_s b_3}{L_0 I_0}; E_B = \frac{T_s E_0}{L_0 I_0}; \gamma = \frac{T_s I_0}{C}; \chi = \frac{i}{I_0}$$

3.4.3.2 Dynamical behavior of the device

The values of other parameters of the system used in this subsection are presented in Table 6 [143,144].

Table 6: The values of parameters use in this subsection.

Coef. Values	Values	Coef.	Values	Coef.	Values	Coef.
ε_{33}^S(nF/m^2) $R(\Omega)$	$r(\Omega)$	4.0	$A_1(mm^2)$	176.76	$H_c(A/m)$	100
$L(mH)$	50	N	1000	$l_1(cm)$	24	$B_r(mT)$	54

In reference [143], it was demonstrated that the parameter σ has no significant effect on the behavior of the circuit. Thus, to simplify the analysis during this investigation, the parameter

σ is now neglected. Knowing that, $1+\cosh(\chi)=2\cosh^2\left(\dfrac{\chi}{2}\right)$ and $\cosh^2\left(\dfrac{\chi}{2}\right)-\sinh^2\left(\dfrac{\chi}{2}\right)=1$, Eqs. (3.36) can be written as:

$$\begin{cases} \dfrac{d^2\Theta}{d\tau^2}+\alpha_1\dfrac{d\Theta}{d\tau}+\alpha_2\Theta+\alpha_4 z=0 \\[2mm] \left[1-\xi\tanh^2\left(\dfrac{\chi}{2}\right)\right]\dfrac{d\chi}{d\tau}+\beta_1\chi+\beta_2 z+\beta_3\Theta=E_{B_s}\sin\Omega\tau \\[2mm] \dfrac{dz}{d\tau}=\gamma\chi \end{cases} \tag{3.37}$$

Using the harmonic balance method as before, it is found that the amplitudes A, B and C of the current flowing through the circuit, mechanical deflection of the PZT and the electric voltage trough the capacitor respectively satisfy the following set of nonlinear algebraic equations:

$$a_1 A^{10}+a_2 A^8+a_3 A^6+a_4 A^4+a_5 A^2-GE_{B_s}=0 \tag{3.38}$$

$$B^2=\frac{\alpha_4^2\xi^2}{\Omega^2 G}A^2 \tag{3.39}$$

where coefficients a_i and G are given as:

$$a_1=\frac{\Omega^2\xi^2}{144}\left(\Omega^4-4\Omega^3+\Omega^2\alpha_1^2+6\Omega^2-4\Omega+1\right); a_2=\frac{\Omega^2\xi^2}{24}\left(-\Omega^4+4\Omega^3-\Omega^2\alpha_1^2-6\Omega^2+4\Omega-1\right)$$

$$a_3=\frac{\Omega\xi}{16}\begin{bmatrix}\dfrac{8}{3}\Omega^5+\xi\Omega^5-4\xi\Omega^4-(32/3)\Omega^4+6\xi\Omega^3+16\Omega^3+\alpha_1^2\xi\Omega^3-\dfrac{8}{3}\gamma\beta_2\Omega^3+\dfrac{8}{3}\alpha_1^2\Omega^3-4\xi\Omega^2-\dfrac{32}{3}\Omega^2 \\[2mm] -16\gamma\beta_3\Omega+\xi\Omega-\dfrac{8}{3}\alpha_1^2\gamma\beta_2\Omega+\dfrac{8}{3}\xi\Omega+\dfrac{32}{3}\gamma\beta_2+\dfrac{8}{3}\alpha_1\beta_3-\dfrac{8}{3}\xi\gamma\beta_2+\dfrac{32}{3}\gamma\beta_2\end{bmatrix}$$

$$a_4=\frac{1}{2}\begin{bmatrix}-\xi\Omega^6+2\xi\Omega^5-3\xi\Omega^4-\alpha_1^2\xi\Omega^4+\xi\gamma\beta_2\Omega^4-2\xi\gamma\beta_2\Omega^3+4\xi\Omega^3-\xi\Omega^2+\alpha_1^2\xi\gamma\beta_2\Omega^2+6\xi\gamma\beta_2\Omega^2-\alpha_1\xi\beta_3\Omega \\[2mm] -4\gamma\beta_2+\xi\gamma\beta_2\end{bmatrix} \tag{3.40}$$

$$a_5=\begin{bmatrix}\Omega^6-4\Omega^5+2\xi\Omega^5+\xi\gamma\beta_2\Omega^4+\alpha_1^2\Omega^4-2\gamma\beta_2\Omega^4+\beta_1^2\Omega^4+6\Omega^4-4\beta_1^2\Omega^3-4\Omega^3+8\gamma\beta_2\Omega^3+\beta_2^2\beta^2\Omega^2 \\[2mm] +6\beta_1^2\Omega^2+\alpha_1^2\beta_1^2\Omega^2-12\gamma\beta_2\Omega^2+\Omega^2-2\alpha_1^2\beta_2\Omega^2+8\gamma\beta_2\Omega-4\beta_1^2\Omega-4\beta_2^2\gamma^2\Omega+2\beta_1\beta_3\Omega+2\alpha_1\beta_3\Omega \\[2mm] +\dfrac{\beta_2^2\gamma^2}{\Omega^2}-\dfrac{4\beta_2^2\xi^2}{\Omega}-4\beta_1\beta_3+\dfrac{\beta_3^2}{\Omega^2}-\dfrac{2\alpha_1\beta_2\beta_3\xi}{\Omega}+\dfrac{2\beta_1\beta_3}{\Omega}+6\beta_2^2\xi^2-2\gamma\beta_2+\alpha_1^2\beta_2^2\xi^2+\beta_1^2-4\gamma\beta_2\end{bmatrix}$$

$$G=\left[\left(1-\Omega^2\right)^2+\left(\alpha_1\Omega\right)^2\right]$$

Figure 33 depicts the variations of A and B when the frequency varies. One observes the appearance of hysteresis and jump phenomena at frequency close to $\Omega=1$ (or in dimensions to $3.40\ MHz$).
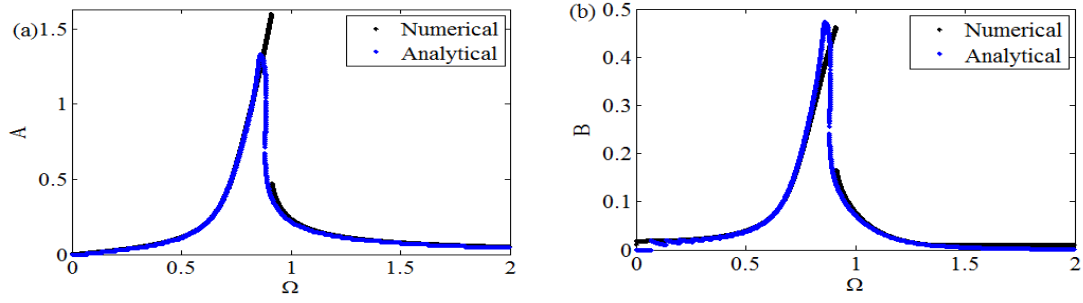
Figure 33: Amplitudes of electrical part (a) and mechanical part (b) as function of normalized frequency. Curve of harmonic balance approximation (Blue) and curves from the direct numerical simulation of modal equations (black) for $B_s = 130 \; mT$ and $E_{B_s} = 8.86 \times 10^{-2}$

The bifurcation diagrams versus the saturation parameter, the amplitude and the frequency of the external excitation are plotted in Figure 34. One observes chaos oscillations for $\{B_s \in [0.01; 0.11] \cup [0.16; 0.46] \cup [0.54; 1.23]\}$ with $E_{B_s} = 0.5$ and $\Omega = 0.51$; for $E_{B_s} \in \{[0.09; 0.29] \cup [0.36; 0.39] \cup [0.42; 0.59] \cup [0.858; 1] \cup [1.31; 3]\}$ with $B_s = 130 \; mT$ and $\Omega = 0.151$ and for $\Omega \in \{[0.049; 0.189] \cup [0.301; 0.63] \cup [0.83; 0.91]\}$ with $E_{B_S} = 0.5$ and $B_s = 130 \; mT$
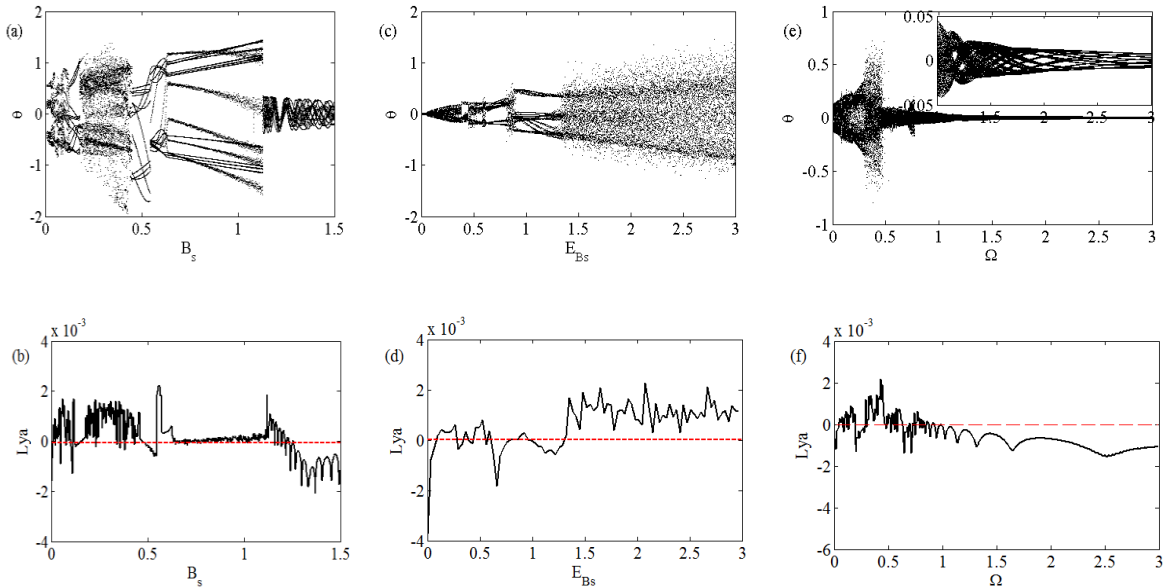
Figure 34: Bifurcation diagram (a) and Lyapunov exponent (b) against B_s (saturation parameter) for $E_{B_S} = 0.5$ and $\Omega = 0.51$; bifurcation diagram (c), Lyapunov exponent (d) against E_{B_s} for $B_s = 130 \; mT$ and $\Omega = 0.51$; bifurcation diagram (e) and Lyapunov exponent (f) against Ω for $E_{B_S} = 0.5$ and $B_s = 130 \; mT$ with the parameter of table 6.

3.4.3.3 Applications

a- *Periodic and chaotic actuation*

The field of application of periodic and chaotic actuators extends over mass production applications. Indeed, when ultrasounds are generated as conventional sinusoidal signals, they constituted the basic signals for periodic actuators like sound transmitters, ultrasonic power transducers and sensors, bending actuators for textile machines, ink print heads, beam benders in valves, in braille displays, in optical systems and newly as monolithic multilayer actuators for automotive injection system. The chaotic actuators offer efficient and rapid mixing and sieving processes [145-147].

b- Nebulizers

The nebulizer consists of an ultrasonic source (piezoelectric crystal) [148] and a tank containing the liquid to be nebulized (Figure 36). Nebulized aerosols can be designed for oral inhalation to the lungs, nasal inhalation to the upper respiratory tract, or both though the use of sized face masks. The piezoelectric crystal vibrates in the frequency range 1 to 4 MHz thanks to an alternating electric field produced by an electronic oscillator [149]. We have sketched in Figure 35 how the nebulizer structure looks like.
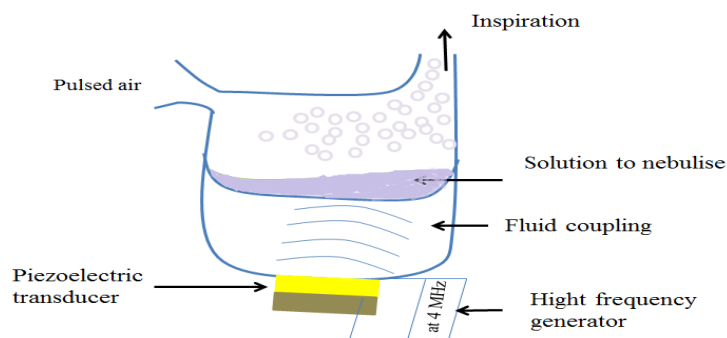
Figure 35: Schematic representation of the ultrasonic nebulizer.

The device operates almost silently; the deformed crystal transmits the vibrations to the liquid to be nebulized via a liquid coupling. The drug is deposited in a hemispherical cup partially submerged in a water tank placed above the crystal: the water serves as a transmission fluid. During the operation, a liquid fountain forms in the nebulization tank, like a geyser. Large droplets are emitted at the top while fine particles are at the bottom. Pressure waves follow one another closely and generate gas bubbles in the liquid (of the order of μm diameter) which implodes on the surface and are then inhaled by the patient.

The results presented in section 2.2 are interesting since the piezoelectric beam generates vibration in the frequency range $1-4\ MHz$. When the vibrations are periodic as obtained by the harmonic balance method, one observes a periodic nebulization of the drug.

As it has been shown in recent years, the chaotic vibration offers efficient and rapid mixing and sieving processes [145-147]. It is expected that in the ranges of parameters (frequency, amplitude of the external excitation and saturation coefficient) where one observes chaotic vibrations of the piezoelectric beam, the nebulization process will take less time. This needs to be verified experimentally. This is important for patient receiving a nebulization treatment.

3.5 *Bursting like oscillations by a piezoelectric beam and applications*

3.5.2 Generating bursting like oscillations in the piezoelectric beam

In recent years, the question of making mechanical arms vibrate in a pulse-like and bursting-like manners has been considered using magnetic and capacitive coupling [149,150]. These electrical sources were made of electrical circuit mimicking the behavior of biological and chemical oscillators. In this section, the electric signals are generated by an electronic circuit inspired by the Hindmarsh-Rose oscillator (H-R) [149,150]. This biological oscillator is described by the following set of three coupled differential equations [151]:

$$\begin{cases} \dfrac{dV_x}{dt} = -V_x^3 + 3V_x^2 + V_y + I - V_z \\[2mm] \dfrac{dV_y}{dt} = 1 - 5V_x^2 - V_y \\[2mm] \dfrac{dV_z}{dt} = \zeta_r (S_r (V_x - V_{x0}) - V_z) \end{cases} \qquad (3.41)$$

where V_x represents the membrane potential of a neuron, V_y the fast current through the membrane, V_z the slow current and I the applied external current. This phenomenological neuron model, which has been proposed by H-R, is one of the most interesting neuron models used for studying the neuronal activities. The main parameter which modulates the response of the H-R oscillator is the applied DC current I whose variation leads the system to exhibit several dynamical behaviors such a bursting oscillations with several pulses staring at $I = 1.5$. The number of pulses in each bursting package increases with I [149,151].

To make the piezoelectric beam generated bursting packages, we use the structure presented in Figure 36 in which the piezoelectric beam is submitted to electrical signals generated by the an electronic oscillator circuit for the H-R equations.
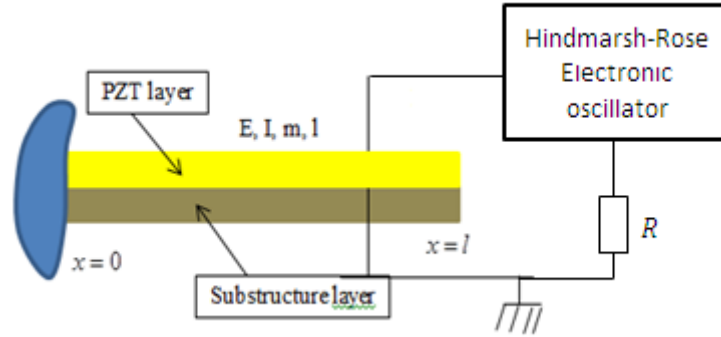
Figure 36: Self-sustained electromechanical system

Knowing that the PZT is in series with the load resistance R, we obtain the following coupled equations constituted of one partial differential equations and four first order differential equations:

$$
\begin{cases}
\rho_{total} b \dfrac{\partial^2 w}{\partial t^2} + \lambda \dfrac{\partial w}{\partial t} + E^{'} I \dfrac{\partial^4 w}{\partial X^4} + \vartheta \left(\dfrac{d\delta(X)}{dX} - \dfrac{d\delta(X-l)}{dX} \right) v(t) = 0 \\[3mm]
RC_p \dfrac{dv(t)}{dt} - \varepsilon_{33}^S \dfrac{v(t)}{\varepsilon_0} + \dfrac{d_{31} E_p h_{pc} h_p}{\varepsilon_0} \dfrac{\partial^2 w}{\partial X^2} = V_x \\[3mm]
\dfrac{dV_x}{dt} = -V_x^3 + 3V_x^2 + V_y + I - V_z \\[3mm]
\dfrac{dV_y}{dt} = 1 - 5V_x^2 - V_y \\[3mm]
\dfrac{dV_z}{dt} = \zeta_r (S_r(V_x - V_{x0}) - V_z)
\end{cases}
\tag{3.42}
$$

After dimensionless reduction and use of the modal approach and simplification, it is found that the one mode approximation of the device presented in Figure 38 is described by the following set of differential equations:

$$\begin{cases} \dfrac{d^2Y(\tau)}{d\tau^2} + a_1 \dfrac{dY(\tau)}{d\tau} + Y(\tau) + a_3 e(\tau) = 0 \\[2mm] \dfrac{de(\tau)}{d\tau} + b_1 e(\tau) + b_2 Y(\tau) = b_3 v_X \\[2mm] \dfrac{dv_X}{d\tau} = T(-v_X^3 + 3v_X^2 + v_Y + I_b - v_Z) \\[2mm] \dfrac{dv_Y}{d\tau} = T(1 - 5v_X^2 - v_Y) \\[2mm] \dfrac{dv_Y}{d\tau} = T(\zeta_r (S_r(v_X - v_{X0}) - v_Z)) \end{cases} \qquad (3.43)$$

with the following parameters :

$$a_1 = \frac{T\lambda}{\rho_{total}}; a_{22} = \frac{E'IT^2}{\rho_{total}l^4}; a_{33} = \frac{T^2 v_0 \vartheta}{l^2 \rho_{total} h_{sp}} \; ; \quad b_1 = \frac{-T\varepsilon_{33}^S}{RC_p h_p}; b_{22} = \frac{-T d_{31} E_p h_{pc} h_{sp}}{l^2 RC_p}; b_3 = \frac{T\varepsilon_0 u_0}{h_p RC_p v_0} \; ;$$

$$a_3 = a_{33}I_2; \quad b_2 = b_{22}I_3 \; ; \; a_{22}I_1 = 1.$$

where I_1, I_2 and I_3 are given after equation (3.23).

The values of other parameters of the system used in this section are presented in Table 7 [138].

Table 7: Geometric, material and electro-mechanical parameters of the substructure and of the piezoelectric layer.

Coefficients	Values	Coefficients	Values
ε_0(F/m)	9885×10^{-12}	ζ_r	2.1×10^{-3}
v_{x0}	-1.6	S_r	4

The set of Eqs. (3.53) is solved numerically using the fourth order Runge-Kutta method. The control parameter is the bias current I which is varied to find regions where the piezoelectric beam exhibits bursting-like behaviors. Figure 37 presents the voltage v_x and the deflection Y versus time for two values of the control parameter. It is found that the bursting patterns (Fig. 37(a)) of the Hindmarsh-Rose oscillator are transferred to the piezoelectric beam (Fig. 37(b)).
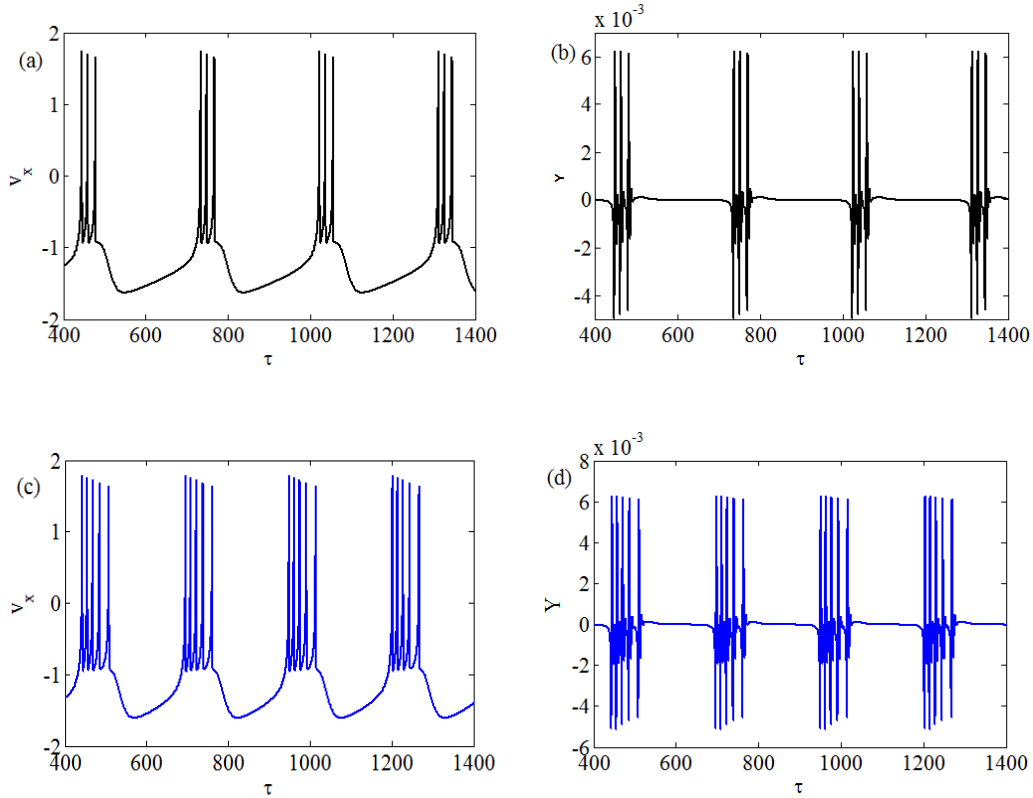
Figure 37: Time variation of the actuator response for two values of I_b: in black $I_b = 1.5$ and blue $I_b = 2.0$ (with de parameter of table 7).

Looking at Figure 37 where for $I_b = 2.0$ (Figure 37(c) and 37(d)) the frequency of the wave increases and the length of the burst increases (6 peaks or oscillations for the blue curve) compared to the dynamics for $I_b = 1.5$ (Figure 37(a) and 3.37(b), black curves) which presents 3 peaks.

Now, let t_1 the period of appearance of the wave for $I_b = 2.0$ (Figure 38(a) and 38(b)) and t_2 for the wave of $I_b = 2.5$ (Figure 38(c) and 38(d)). After calculation, we get $t_1 = 12.7$ and $t_2 = 11.0$. Consequently, the frequency of the wave for $I_b = 2.5$ (Figure 38(d)) is greater than the frequency of the wave for $I_b = 2.0$ (Figure 38(b)). Now let us call by T_1, the length of the wave with $I_b = 2.0$ and by T_2, the length for the wave with $I_b = 2.5$. We finds $T_1 = 77$ and $T_2 = 107$. That is to say $T_2 \succ T_1$. In accordance with the principle of ultrasound generation, the red burst (Figure 38(d)) is longer than the blue (Figure 38(b)). Therefore, with the device

presented in Figure 38, increasing the parameter I_b, the frequency of vibration of the waves is not only increased but also their lengths (length of the burst).
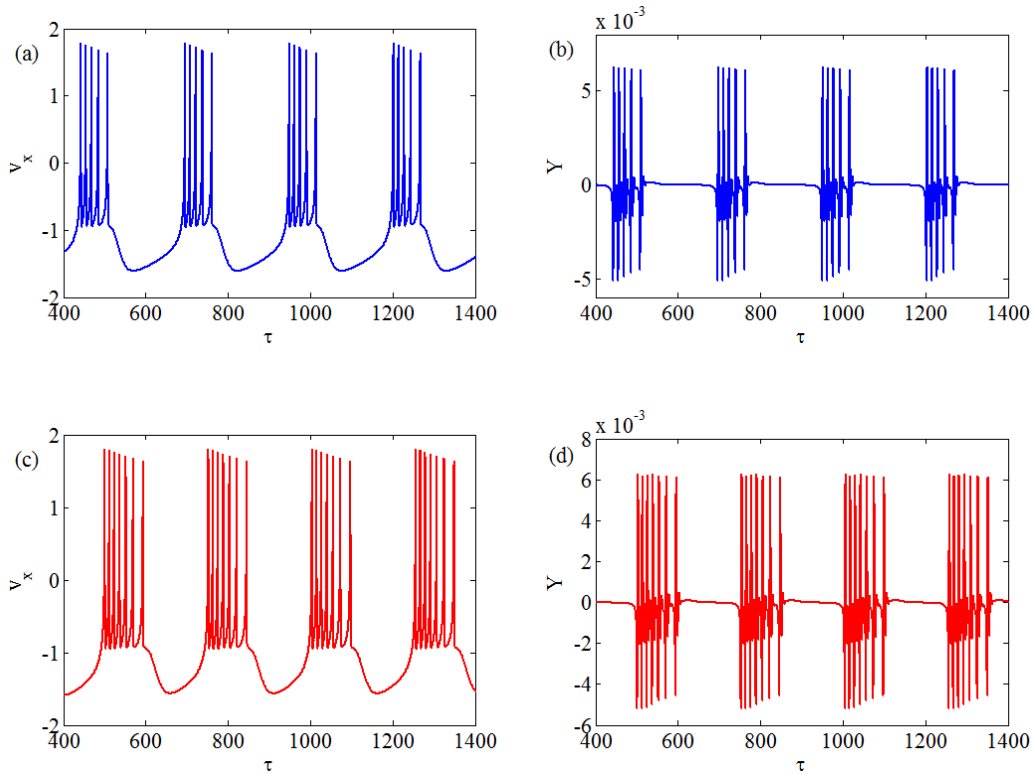
Figure 38: Actuator response for two values of: In blue for $I_b = 2.0$ and in red $I_b = 2.5$ (with the parameters of Table 6).

3.5.3 Applications

3.5.3.1 Bursting like actuators

This type of oscillations can find applications in automation engineering where one wants the mechanical part to act for a very short time and return to its rest state. This can also give some hints in bio-engineering of the cardiovascular system as the electromechanics of the heart exhibits bursting phenomena.

3.5.3.2 Applications for echography

From the literature review, we have presented in Figure 41 a schematic view of how signals are delivered for echography analysis. It is a series of ultrasound bursts. Reference [152] gives additional comments on the matter. In Figure 39(a), the frequency is lower than in Figure 39(b). It follows that the duration occupied by the burst (pulse), that is to say $t1$ is greater than $t2$, the time occupied by a burst emitted with a probe higher frequency. This is due to the fact that a burst is formed by the same number of cycles (number of peaks of

oscillation per burst). It is noted that between two bursts, there are long silences (intervals of time without emission).
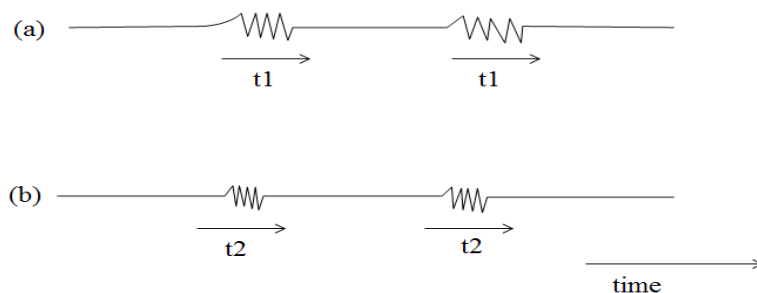
Figure 39: Schematic representation of the generation of ultrasonic bursts according to the frequency of the probes.

The periods of silence are used to receive the echoes. However, the resolution of the image is based on two major points: the length of the burst and the lateral resolution. The length of the burst which will determine the axial resolution is defined as the ability to differentiate objects along the path of the wave. The number of waves per pulse is identical regardless of the frequency of the probe. On the other hand, the length of the burst generated decreases when the frequency increases and the wavelength decreases. For shorter wavelengths, better axial resolution is obtained. To improve the axial resolution, a high frequency is necessary. But since the penetration is inversely proportional to the frequency, it is the depth to be studied which guides the choice of the probe frequency. The lateral resolution characterizes the ability to discriminate two adjacent reflectors, but located at the same depth. It depends on the diameter of the ultrasound beam which varies with the frequency of the probe and the distance between the points to be viewed from the probe.

The results presented in Figures 37 and 38 can be linked to what is described above. Indeed, one can solve the problem of the reduction of the length of the bursts for echography and that of the wavelength for large frequencies for the ultrasounds applications. This appears in Figure 37 where one finds that the wave frequency and burst length increases (6 peaks or oscillations for the blue curve) for $I_b = 2.0$ (Figure 38(c) and 38(d)) while for $I_b = 1.5$ (Figure 37(a) and 37(b), black curves), one observes only 3 peaks. From the results presented in Figure 39, one can expect that by monitoring the PZT with an oscillator capable of bursting mechanical vibrations, one may obtain for large frequencies, not only a good axial resolution, but also an increase in the depth to be explored. Indeed as demonstrated above, the period of appearance of bursting wave can be monitored by varying I_b. This is also the case for the wave length which depends on I_b. In accordance with the principle of ultrasound generation,

the red burst (Figure 37(d)) is longer than the blue (Figure 38(b)). Therefore, with the device presented in Fig. 36, increasing the parameter I_b, the frequency of vibration of the waves is not only increased but also their lengths (length of the burst). With these results, it is expected that for large frequencies, strong penetrations and a good axial and lateral resolution can be obtained. We would like to mention that the Hindmarsh-Rose oscillator can be simulated using the classical electronic circuits (analog or discrete components). And importantly, it can be simulated using microcontrollers, thus providing a good signal generator to monitor the piezoelectric beam with amplification if necessary.

3.6 Self-sustained energy harvesting from micro beam under fluid flow

3.6.2 Model of energy harvester and equations

3.6.2.1 The physical structure and modeling

The physical model is a very small beam mounted as a suspension bridge. The beam is subjected to forces produced by a fluid or air flow. The flow is transversal to the beam direction as it is represented in (Figure 40). Piezoelectric layers are fixed at both ends of the beam so that the beam deformations led to the piezoelectric material deformation. Consequently, electricity can be generated. The piezoelectric layers are materialized by P in the figure (in yellow). The beam had a length L, width b, and thickness h. The load of resistance R_C is connected to the piezoelectric layers. The blue lines maintain the beam in suspension. These cables are present here because the model of harvesting energy is based on the existing bridge model.
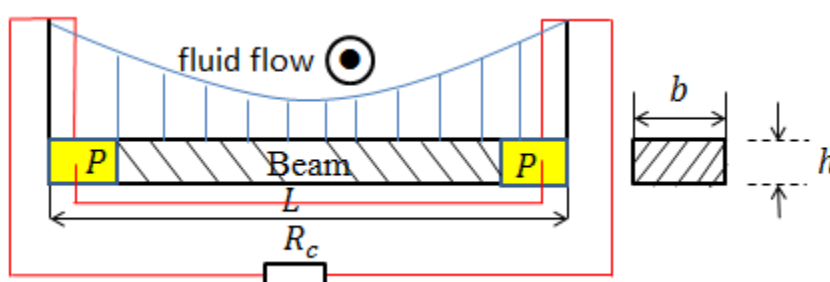
Figure 40: Schematic diagram of the harvester system. P-piezoelectric element, load resistance.

As represented in Figure 40, the fluid flows transversally to the direction of the beam. When the fluid flow pressure acts continuously on the beam, it happens that for some fluid flow characteristics, the beam undergoes self-sustained vibrations as is demonstrated below.

These self-sustained vibrations lead to the self-sustained production of electrical energy because of the self-sustained deformations of the piezoelectric layers.

Following mechanical laws and piezoelectric conversion mechanisms, it can be established, as in References [153-155], that the vibration of the electromechanical system in Figure 40 is described by the following set of partial differential equations:

$$\begin{cases} \rho A \dfrac{\partial^2 w}{\partial t^2} + \lambda \dfrac{\partial w}{\partial t} + EI \dfrac{\partial^4 w}{\partial X^4} + \dfrac{EA}{2} \dfrac{\partial^2 w}{\partial X^2} \int_0^L \left(\dfrac{\partial w}{\partial X} \right)^2 dX - K_0 v(t) f(X) = \overline{F}(t) \\[2mm] C_p \dfrac{dv(t)}{dt} + \dfrac{v(t)}{R_c} = -K_1 \int_{x=0}^L \dfrac{\partial^3 w}{\partial X^2 \partial t} f(X) dX \\[2mm] i(t) = -K_1 \int_0^L \dfrac{\partial^3 w}{\partial X^2 \partial t} dX - C_p \dfrac{dv(t)}{dt} \end{cases} \tag{3.44}$$

with the following boundary conditions

$$w(0,\ t) = w(L,\ t) = 0 \ \text{and} \ \frac{\partial^2 w(0,\ t)}{\partial X^2} = \frac{\partial^2 w(L,\ t)}{\partial X^2} = 0 \tag{3.45}$$

$w(X,t)$ is transversal deformation of the beam in the direction of fluid flow. It is a function of time t and the spatial coordinate X along the beam. E is the Young modulus; A is the beam cross section; ρ is the beam mass density; λ is the viscous damping; K_0 and K_1 are the piezoelectric coupling terms; C_p is the equivalent capacitance of the piezoelectric element; R_c is the resistive load; $v(t)$ is voltage generated by the piezoelectric element; and $i(t)$ the current trough the resistive load. $f(X) = H(X) - H(X - X_1) + H(X - X_2) - H(X - L)$ is the spatial function used to specify that the piezoelectric patches are localized in the regions $0 \prec X \prec X_1$ and $X_2 \prec X \prec L$, where $H(\bullet)$ is the Heaviside step function. Finally, $\overline{F}$ is the general fluid-induced forcing function per unit length of beam [156].

In a more complete model, the fluid-induced forcing function for the interaction of the fluid flow with the micro-beam is given as follows [156]:

$$\overline{F} = \frac{1}{2} \rho U^2 \left[\left(Y_1 - \frac{Y_2}{UD} \left(\frac{\partial^2 w}{\partial X^2} \right)^2 \right) \frac{1}{D} \frac{\partial w}{\partial t} + J_1 \frac{\partial^2 w}{\partial X^2} + J_2 \left(\frac{\partial^2 w}{\partial X^2} \right)^3 \right] \tag{3.46}$$

where Y_1 is a linear aeroelastic damping term, Y_2 is a nonlinear aeroelastic damping term, J_1 is a linear aeroelastic stiffness term, J_2 is a nonlinear aeroelastic stiffness term. In essence, Y_1 and Y_2 represent the self-excitation and self-limitation characteristics of the response. J_1

represents the shift in the mechanical response frequency from the zero-fluid frequency. The set of Equation (3.64) can thus be rewritten as follows:

$$\begin{cases} \rho A \dfrac{\partial^2 w}{\partial t^2} + \lambda \dfrac{\partial w}{\partial t} + EI \dfrac{\partial^4 w}{\partial X^4} + \dfrac{EA}{2} \dfrac{\partial^2 w}{\partial X^2} \displaystyle\int_0^L \left(\dfrac{\partial w}{\partial X} \right)^2 dX - K_0 v(t) f(X) = \\[3mm] \dfrac{1}{2} \rho U^2 \left[\left(Y_1 - \dfrac{Y_2}{UD} \left(\dfrac{\partial^2 w}{\partial X^2} \right)^2 \right) \dfrac{1}{D} \dfrac{\partial w}{\partial t} + J_1 \dfrac{\partial^2 w}{\partial X^2} + J_2 \left(\dfrac{\partial^2 w}{\partial X^2} \right)^3 + \dfrac{1}{2} C_L \sin(\omega t) \right] \\[3mm] C_p \dfrac{dv(t)}{dt} + \dfrac{v(t)}{R_c} = -K_1 \displaystyle\int_{x=0}^L \dfrac{\partial^3 w}{\partial X^2 \partial t} f(X) dX \\[3mm] i(t) = -K_1 \displaystyle\int_0^L \dfrac{\partial^3 w}{\partial X^2 \partial t} dX - C_p \dfrac{dv(t)}{dt} \end{cases} \quad (3.47)$$

Let us mention the introduction of the temporal excitation of frequency ω, which accounts for the fluid force coefficient of the transverse direction through the C_L coefficient, which is seen as the lifting coefficient.

In order to put the equations in a dimensionless form, we use the following quantities:

$$w(X,t) = h y(x, \tau), \quad \chi = \dfrac{v}{v_0}, \quad x = \dfrac{X}{l}, \quad i_r = \dfrac{i}{i_0}, \quad \tau = \dfrac{t}{T}$$

where h is the thickness of the beam and $T = \sqrt{\dfrac{\rho L^4 A}{EI}}$ is the beam natural period. The quantities i_0 and v_0 are, respectively, $i_0 = 1$ A and $v_0 = 1$ V.

The system of equations in dimensionless form is, thus, as follows:

$$\begin{cases} \dfrac{\partial^4 y(x,\tau)}{\partial x^4} + \dfrac{\partial^2 y(x,\tau)}{\partial \tau^2} + \alpha_{11} \dfrac{\partial y(x,\tau)}{\partial \tau} + \alpha_{22} \dfrac{\partial^2 y(x,\tau)}{\partial x^2} \displaystyle\int_0^1 \left(\dfrac{\partial y(x,\tau)}{\partial x} \right)^2 dx - \alpha_{33} \chi(\tau) f(x) = \\[3mm] \varepsilon_0 U^2 \left[\left(Y_1 - \dfrac{\varepsilon_{0n}}{U} \left(\dfrac{\partial^2 y(x,\tau)}{\partial x^2} \right)^2 \right) \dfrac{\partial y(x,\tau)}{\partial \tau} + \beta_{11} U^2 \dfrac{\partial^2 y(x,\tau)}{\partial x^2} + \beta_{22} U^2 \left(\dfrac{\partial^2 y(x,\tau)}{\partial x^2} \right)^3 + f_1 U^2 \sin(\Omega \tau) \right] \\[3mm] \dfrac{d\chi(\tau)}{d\tau} + \gamma_1 \chi(\tau) = \gamma_2 \displaystyle\int_0^1 \dfrac{\partial^3 y(x,\tau)}{\partial x^2 \partial \tau} f(x) dx \\[3mm] i_r(\tau) = \sigma_{11} \displaystyle\int_0^1 \dfrac{\partial^3 w}{\partial x^2 \partial \tau} f(x) dx + \sigma_2 \dfrac{d\chi(\tau)}{d\tau} \end{cases} \quad (3.48)$$

$$\alpha_1 = \dfrac{\lambda T}{\rho A}, \alpha_{22} = \dfrac{ET^2 h^2}{\rho L^3}, \alpha_{33} = \dfrac{K_0 v_0 T^2}{\rho A h}, \varepsilon_{0n} = \dfrac{Y_2 h^2}{Y_1 D L^2}$$

With $\beta_{11} = \dfrac{J_1 \rho_f T^2}{2 \rho A L^2}, \beta_{22} = \dfrac{J_2 \rho_f T^2}{2 \rho A L^6}, \gamma_1 = \dfrac{T}{C_p R_c}, \gamma_{22} = \dfrac{-K_1 h_b}{C_p v_0 L^2}$

$$\sigma_{11} = \dfrac{-K_1 h_b}{i_0 L^2 T}, \sigma_2 = \dfrac{-v_0 C_p}{i_0 T}, f_{0n} = \dfrac{C_L \rho_f T^2}{2 \rho A h}, \varepsilon_0 = \dfrac{\rho_f T}{2 \rho A D}$$

3.6.2.2 Modal equations

The approximate solution of Equation (5) can be obtained through the Galerkin decomposition method by writing

$$y(x,\tau) = \sum_{n=0} \varphi_n(\tau)\sin(n\pi x) \tag{3.49}$$

where $\varphi_n(\tau)$ are the amplitudes of vibration and $\sin(n\pi x)$ are modal functions solutions of the beam linear natural equation with the associated boundary conditions. The Galerkin decomposition method can be truncated to the fundamental mode of vibration under some specific conditions (e.g., nearness of the mode frequency and the excitation frequency or the condition that almost all the energy is inside the single mode considered). Thus, in the modeling set of equations, equation (5) is transformed into the following equations where we consider only one mode with $\varphi = \varphi_n$.

$$\begin{cases} \dfrac{d^2\varphi}{d\tau^2} - \varepsilon_1\left(1 - \varepsilon\varphi^2\right)\dfrac{d\varphi}{d\tau} + \left(\alpha_4 - \beta_1\right)\varphi - \alpha_3\chi + (\alpha_2 - \beta_2)\varphi^3 = f\sin(\Omega\tau) \\[2mm] \dfrac{d\chi}{\partial\tau} + \gamma_1\chi = \gamma_2\dfrac{d\varphi}{d\tau} \\[2mm] i_r(\tau) = \sigma_1\dfrac{d\varphi}{d\tau} + \sigma_2\dfrac{d\chi(\tau)}{d\tau} \end{cases} \tag{3.50}$$

Where the new constants are defined as follows:

$$\alpha_2 = \frac{4n\pi}{3}\left[(-1)^n - 1\right]\alpha_{22}, \alpha_3 = \frac{1}{n\pi}\left[(-1)^{n+1} + 1\right]\alpha_{33}, \alpha_4 = n^3\pi^3\left[(-1)^{n+1} + 1\right], \varepsilon = \frac{3n^4\pi^4\varepsilon_{0n}}{4U\left(\alpha_1 - \varepsilon_0 Y_1\right)}, \varepsilon_1 = \alpha_1 - \varepsilon_0 Y_1$$

$$\beta_1 = -n^2\pi^2\beta_{11}U^2, \beta_2 = \frac{-n^6\pi^6\beta_{22}}{2}U^2, \gamma_2 = \frac{n^2\pi^2}{2}\gamma_{22}, \sigma_1 = \frac{n^2\pi^2}{2}\sigma_{11}, f = \frac{\left[(-1)^{n+1} + 1\right]f_1}{n\pi}U^2$$

Looking at the first equation of the set of Equation (3.60), it appears as the Van der Pol-like equation, which presents a nonlinear damping varying alternatively from positive to negative value in one cycle, thus leading to self-oscillations (this is possible when ε and ε_1 are positive; the case is considered here. As it also appears in the expressions of the dimensionless coefficients, the flow velocity affects many coefficients and will be considered as one of the main control parameters.

3.6.3   The self- sustained energy harvester

In the absence of the vortex-shedding part of the fluid force (the temporal sinusoidal term), the first equation of system (3.60) is a Van der Pol-Duffing oscillator, which has many applications in science and engineering, as is the case of the Rayleigh oscillator [157-158]. It generates sinusoidal oscillations for low values of the coefficient ε_1 and relaxation

oscillations for large values of this coefficient. In Figure 41, we have plotted some representatives of time traces of the deflection, voltage, and current for two values of the fluid flow velocity (meaning two different values of ε_1). One finds that when U is small, the voltage, the current, and the displacement present shapes close to sinusoidal function. However, when U becomes large, relaxation oscillations appear for displacement while the current and voltage present bursting dynamics characterized by sharp and rapid variation of their values. Let us mention that the results presented here and in the rest of the work come from the numerical simulation of the set of Equation (3.71) using the fourth-order Runge–Kutta method.
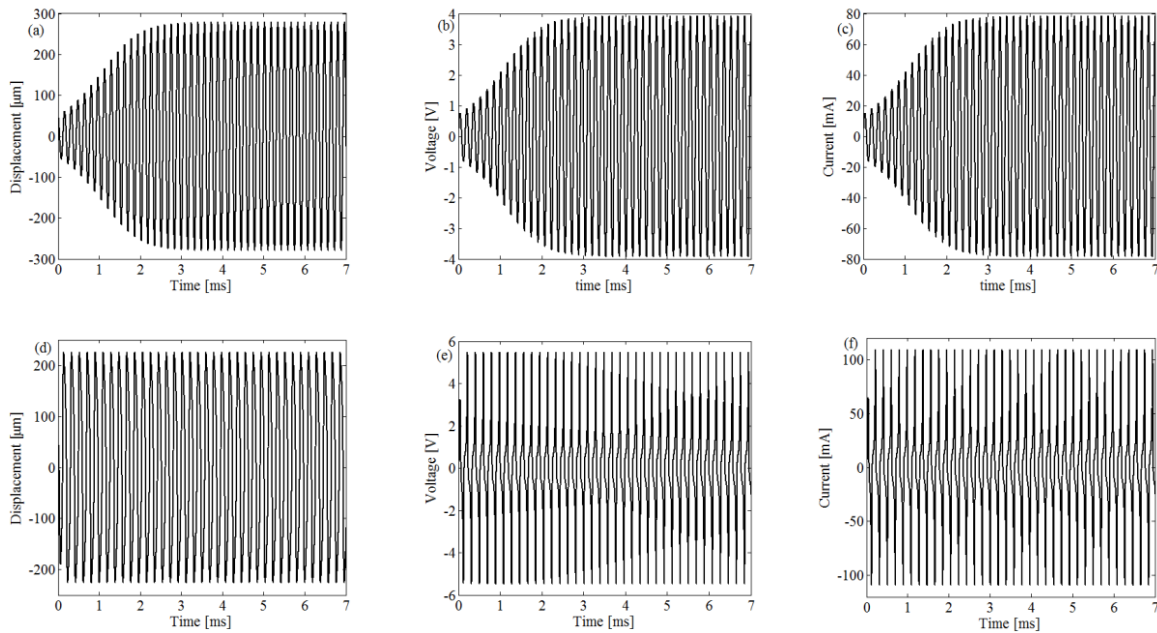
Figure 41: Time variation of the displacement, voltage, and current for two values of the flow velocity. (**a-c**) for $U = 0.25 \ m/s$ and (**d-f**) for $U = 14.5$ m/s with $R_c = 50 \ \Omega$.

3.6.3.1 Variation of the electric power in the resistive load

The power in the load is defined as

$$p = R_c i^2 \tag{3.51}$$

This expression eats can be rewritten as follows

$$P = R_c i_0^2 i_r^2 \tag{3.52}$$

The variation of the maximal power in the load versus the flow velocity and versus the resistance is plotted in Figure 3.42. One notes that the power increased with the flow velocity and the load resistance. Power of about 0.6411 W is found in Figure 42.
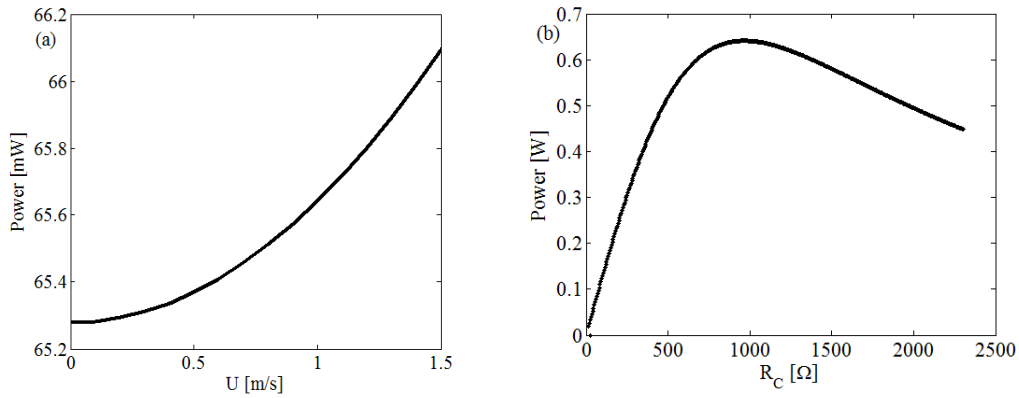
Figure 42: Electric power versus: (a the velocity of the fluid (U) for $R_c = 50\,\Omega$ and (**b**) the load resistance (R_c) for $U = 0.5\,m/s$ with the parameter of Table 8.

Table 8: Geometric, material, and electro-mechanical parameters of the beam and of the piezoelectric patch [138,160].

Coefficients	Values	Coefficients	Values
Length L (mm)	100	E (GPa)	169
Width b (mm)	20	D (mm)	25
Thickness h (µm)	20	C_L (mm)	Variable
Damping λ (Ns/m)	400	ρ (kg/m^3)	7500
Density ρ_f (kg/m^3)	1000	D_{31}	-190×10^{-12}
Velocity $U(m/s)$	Variable	Load resistance $R_c(\Omega)$	Variable
Patch X_1 (mm)	15	Patch X_1 (mm)	15

a- *Analytical Approach*

For some ranges of U, we found that some coefficients of the coupled differential equations are very small. For instance, for $U = 0.25\,m/s$, numerical values of the parameters of Equation (3.71) are:

$\alpha_2 - \beta_2 = 4.715 \times 10^{-2}$, $\alpha_3 = 2.0398 \times 10^{-5}$, $\alpha_4 - \beta_1 = 62.08$, $\gamma_1 = 40.682$, $\gamma_2 = -75.71$,

$\sigma_1 = -1.78 \times 10^{-2}$, $\sigma_2 = -2.35 \times 10^{-4}$.

Since α_3 is very small (coupling coefficient to χ), the first equation is not highly influenced by the other two equations. All the same, the coefficient of the cubic term in the first equation is small. Consequently the first equation can be solved solely with the cubic term discarded, as its coefficient is also very small. From the classical averaging method, this first equation approximated solution (in the absence of the sinusoidal excitation term) is:

$$\varphi = \frac{2}{\sqrt{\varepsilon}} \cos \omega_0 \tau \qquad (3.53)$$

with $w_0^2 = \alpha_4 - \beta_1$

Inserting Equation (3.63) in the two other equations of the set (3.60), one finally obtains that the dimensionless current is given as:

$$i_r = C \sin \omega_0 \tau + D \cos \omega_0 \tau \qquad (3.54)$$

with $C = -\dfrac{2\sigma_1 \omega_0}{\sqrt{\varepsilon}} - A\sigma_2 \omega_0$ and $D = B\sigma_2 \omega_0$

where $A = \dfrac{2\omega_0^2 \gamma_2}{\sqrt{\varepsilon}\left(\omega_0^2 + \gamma_1^2\right)}$ and $B = \dfrac{-2\omega_0 \gamma_1 \gamma_2}{\sqrt{\varepsilon}\left(\omega_0^2 + \gamma_1^2\right)}$

These relations between the coefficients A, B, C, and D permit us to write the analytical expression of the maximal electric power as:

$$P_{max} = R_c i_0^2 (C^2 + D^2).$$

From the mathematical approach, one can find that the power increases with the load resistance up to the maximum value $P_{max} = 0.6411 \, W$ corresponding at $R_c = 980 \, \Omega$ before decreasing for $R_c \succ 980 \, \Omega$. This explains what is presented in Figure 43, where one finds an optimal point of the electric power versus R_c, both from the analytical development and from the numerical simulation of the set of Equation (3.50).
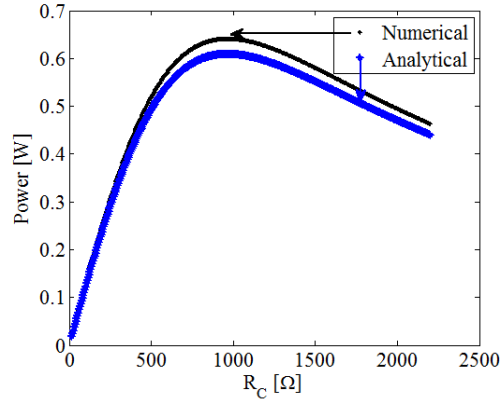
Figure 43: Electrical power versus the load resistance (results from the analytical development and that of the numerical simulation).

3.6.4 Influence of the fluid force coefficient on the energy harvesting

3.6.4.1 Bifurcation diagram and Chaos

Generally, the fluid force coefficient ($f\cos(\omega\tau)$) in the transverse direction is neglected because it is generally smaller than the aerodynamic lift caused by the motion of the body [160]. In this section, this perturbation is considered.

With the presence of the periodic excitation, one expects different types of dynamical behaviors, which can be seen from the bifurcation diagram obtained after solving Equation (3.70) numerically. The bifurcation diagram helps to delimit domains of a control parameter corresponding to different types of dynamical behaviors, such as periodic and chaotic behaviors. The bifurcation diagram is accompanied by the variation of the Lyapunov exponents spectra or that of the largest Lyapunov exponent.

Figure 44 presents the bifurcation diagram (Figure 44(a)) with the corresponding maximal Lyapunov exponent (Figure 44(b)), considering the voltage as the variable and C_L as the control parameter. One finds that when C_L varied, the system moved from a state of regular motion to reach chaotic states. Indeed, as C_L increased from $0.01\,mm$ to $1.05\,mm$, regular motion persisted. Chaos appeared for $C_L \in [1.06\,mm; 2.19\,mm[\cup [3.99\,mm; 4.44\,mm[\cup [4.47\,mm; 5.04\,mm[$. Period-5 orbit appeared for $C_L \in [2.19\,mm; 3.99\,mm[\cup [4.44\,mm; 4.77\,mm[$ while period-3 orbit took place for $C_L \in [5.04\,mm; 13.55\,mm[$. Finally, period-1 orbit was present for $C_L \in [13.55\,mm; 15.00\,mm[$. These transitions were confirmed by the variation of the maximal Lyapunov exponent (Figure 44(b)). A positive value of maximal Lyapunov

corresponded to the chaotic states and the negative value of maximal Lyapunov to the periodic states.
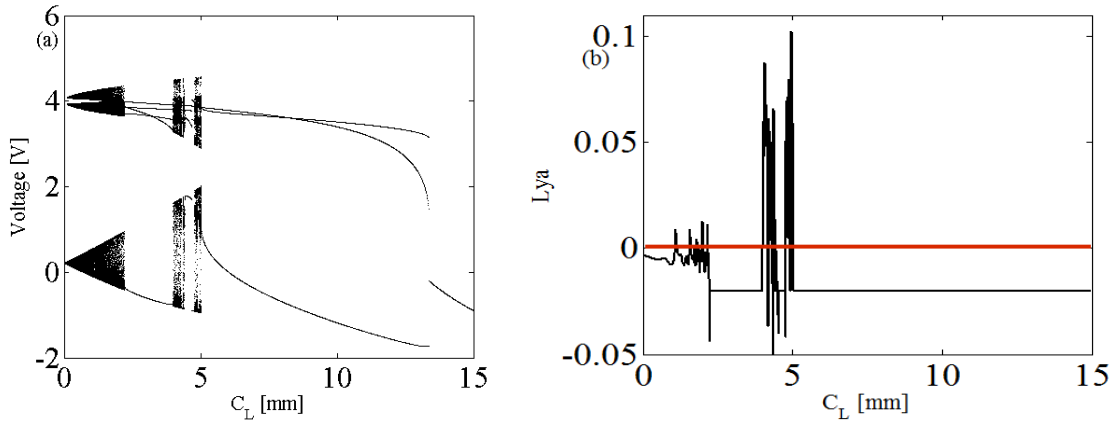
Figure 44: Bifurcation diagram (a) and Lyapunov exponent (b) versus CL, the amplitude of the fluid force coefficient for $U = 25 \ m/s$, $f = 200 \ kHz$ and $R_c = 50 \ \Omega$.

Figure 45 presents two chaotic states. Figure 45 (a), (d) present the phase portraits of the beam displacement and velocity for $C_L = 2.18 \ mm$ and $C_L = 4.12 \ mm$, respectively. The corresponding time variation of the voltage and current, respectively, appear in Figure 45 (b), (c) for $C_L = 2.18 \ mm$ and Figure 45 (e), (f) for $C_L = 4.12 \ mm$.
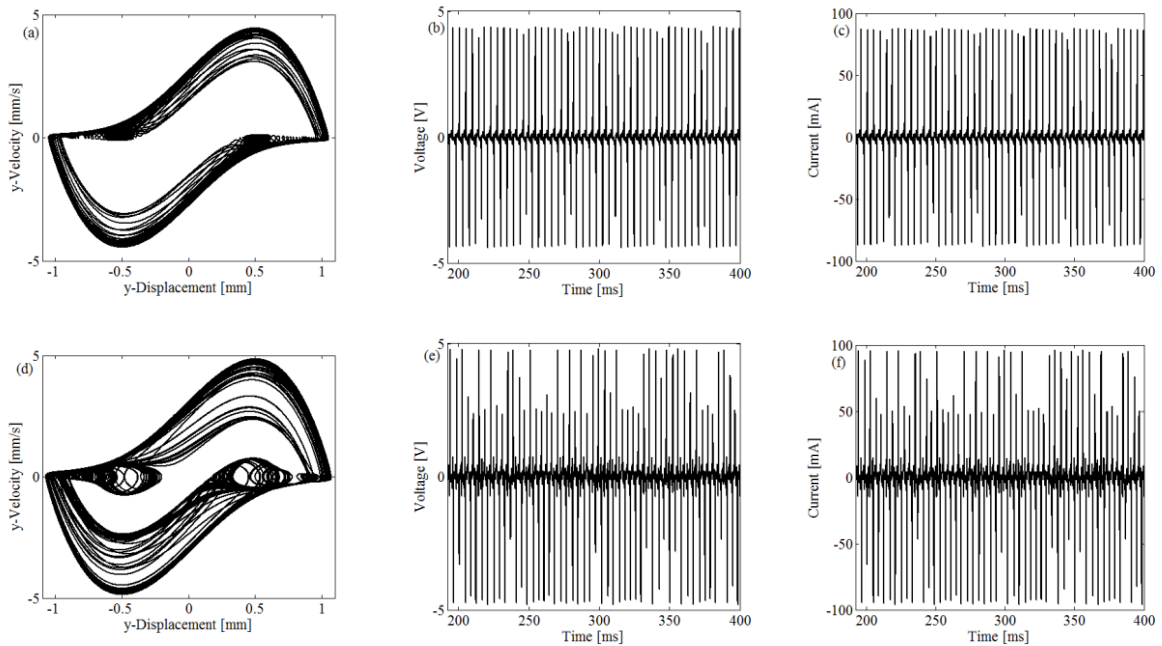
Figure 45: Phase portraits of the beam displacement and temporal trace of the voltage and current with the parameters of Figure 4 with $U = 25\ m/s$, $R_c = 50\ \Omega$, $C_L = 2.18\ mm$, for (**a**-**c**) and $C_L = 4.12\ mm$ for (**d**-**f**).

3.6.4.2 Variation of the Electric Power Versus the Frequency of the External Excitation

Figure 46 shows the evolution of the electric power versus the frequency for some values of the resistance. It first increased with the frequency and attained the maximal value at frequency $f = 75\ \text{k}Hz$. Then it decreased as the frequency increased and attained a relative minimal value before increasing to reach another peak from which it decreased slowly with the frequency. The maximal value increased with the value of the resistance. It was about $0.22\ W$ for $R_c = 200\ \Omega$.
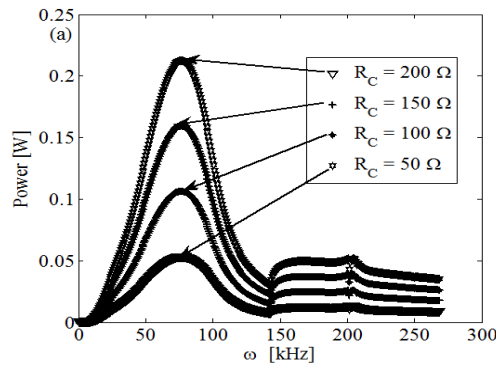
Figure 46: Variation of the maximal value of the electrical power versus the frequency of the external excitation.

3.7   Conclusion

In this chapter, the results of our work have been presented and discussed. We have carried out a theoretical and experimental characterization of the piezoelectric plate. We have also shown that, by making an appropriate choice of the geometric parameters of the piezoelectric micro beam, which is excited by a sinusoidal excited nonlinear oscillator, one can generate mechanical vibrations having periodic, bursting oscillations and chaotic shapes. At the end, we have studied the problem of self-sustained harvesting energy from fluid flow acting on a suspension beam (based on the model of a real bridge) having two piezoelectric patches at both ends.

General conclusion

The main purposes of this thesis were: (1): the use of experimental and theoretical approaches to characterize piezoelectric structures and use vibration modes of the piezoelectric plate and the direct simulation of the PDEs to justify qualitatively the resonance peaks from the experimental curve and use mathematical formalisms, numerical methods and experimental procedure based on analog circuits; (2): the study of a piezoelectric plate based self-excited oscillator; (3): the analysis of the piezoelectric micro beam powered by a circuit with a nonlinear components, which can generate mechanical vibrations having periodic, bursting oscillations and chaotic shapes; (4): based on the model of a real bridge, the modeling and analysis of a micro beam having two piezoelectric patches in both ends produce self-sustained energy harvester for fluid flow. The influence of fluid force coefficient has been study.

Summary of the main results

Firstly, after obtaining the experimental curve of the impedance of a piezoelectric plate versus the frequency of a voltage delivered by a low frequency generator, an equivalent electric circuit for a piezoelectric plate has been proposed. This electric equivalent is constituted of an assembly of resonant branches in parallel; the number of resonant branches depending on the range of frequencies. Using the modal approach and appropriate mathematical techniques, we have justified the appearance of different branches in the electric equivalent of the piezoelectric plate by the appearance of vibrations modes exhibited by the piezoelectric plate when it is submitted to the action of a sinusoidal voltage.

Secondly, inserting a nonlinear resistance in series with the three branches electric equivalent of the piezoelectric plate, we have been able to demonstrate the generation of self-sustained electrical oscillations whose signal shape moves from the periodic sinusoidal oscillations to relaxation oscillations as in the case of the Van der Pol oscillator. The theoretical results have been confirmed by an experimental circuit implementation; thus leading to a self-sustained electrical oscillator whose one component is the piezoelectric plate. Since the piezoelectric oscillator is also an electromechanical system delivering mechanical deformation, we have established theoretically the generation of mechanical deformation by transforming the partial differential equation describing the piezoelectric plate vibration into a set of ordinary differential equations (each differential equation corresponding to a vibration mode). To complete this last, we have simulate directly the PDEs. Low amplitude periodic deformations have been obtained, meaning that the self-sustained piezoelectric plate can serve as a periodic actuator.

Thirdly, we have shown that by making an appropriate choice of the geometric parameters of the piezoelectric micro beam with a nonlinear electrical component and a sinusoidal voltage source, mechanical vibrations having periodic and chaotic shapes can be generated. These vibrations are at the origin of ultrasounds which can be used, as explained in the thesis, to improve the efficiency of ultrasonic nebulizers.. This is presumed having in mind recent scientific results which indicate that chaotic vibrations improve the efficiency of activities such as mixing, sieving and shaking.

By exciting the piezoelectric micro beam by an electronic signal delivered by a generator mimicking the behavior of the Hindmarsh-Rose oscillator, one finds that the generation of bursting patterns for different values of the control parameter. We anticipate that these special ultrasonic waves can resolve some drawbacks of the classical echography device: image resolution and high penetration.

Finally, we have considered the problem of harvesting energy from fluid flow acting on a suspended beam having two piezoelectric patches at both ends. The modal approximation has led to a set of coupled differential equations, one of which is the Van der Pol oscillator. Both the analytical and numerical solutions of the differential equations have been conducted, and the shapes of voltages and current have been displayed, indicating sinusoidal form, bursting-like shape with sharp peaks and chaotic shapes. The electric power in the load has been estimated versus the flow rate, the value of the load resistance, and the frequency of the external component of the fluid flow.

Future works

In this thesis, some interesting results have been obtained and have opened interesting perspectives for future investigations. The future works concern specially:

1. For the characterization of the piezoelectric plate, the quantitative agreement has not been obtained between the resonant peaks obtained through the vibration modes approach and the experiment. This was explained by the lack of the values of all the physical parameters of the piezoelectric plate. But it can also be due to the mathematical model describing the piezoelectric plate. These issues constituted questions for future investigations.

2. For the study of the vibrations of the plate as actuator, an extension of this study can be the experimental investigation.

3. For the study of piezoelectric micro-beam powered by nonlinear electrical oscillator for the production of periodic oscillations, chaotic shapes and patterns of bursting

oscillations for applications in engineering and medicine, experiments are needed for the confirmation of these theoretical findings.

4. For the study of the vibrations of a micro beam as energy harvester, this analysis can be complemented by experimental investigation using wind tunnel set-up.

APPENDIX 1: Expressions of different parameters of the three RLC branches model.

Using the same development as above in the two branches, one arrives at the following relations

$$R_2 = Z_{\min 2} \tag{A1.1}$$

$$C_2 = \frac{\left(\dfrac{f_{P2}{}^2}{f_{S2}{}^2} - 1 \right)}{2\pi f_{P2} \sqrt{Z_{\max 2} \cdot Z_{\min 2}}} \tag{A1.2}$$

$$L_2 = \frac{f_{P2}}{f_{P2}{}^2 - f_{S2}{}^2} \cdot \frac{\sqrt{Z_{\max 2} \cdot Z_{\min 2}}}{2\pi} \tag{A1.3}$$

APPENDIX 2: Contribution of piezoelectric layer

In this appendix, we take into account the effect of the piezoelectric layer, we consider the device presented in Figure 28 and rewrite Eq. (3.25) in the form Eq. (A2.1).

$$\rho_{total}b\frac{\partial^2 w}{\partial t^2}+\lambda\frac{\partial w}{\partial t}+\frac{\partial^2 M(X,t)}{\partial X^2}=0 \tag{A2.1}$$

Where $w(X,t)$ is the transverse deflection of the beam relative to its base, $\rho_{total}=\left(\rho h_s+\rho_p h_p\right)$, with ρ_p, the density of the piezoelectric element, of thickness h_p and $M(X,t)$ the internal bending moment of the beam.

The internal moment can be obtained by integrating the first moment of the stress distribution at a cross section over the cross sectional area. The piezoelectric constitutive relations give the stress-strain and electric field relations and they are expressed for the substructure and the PZT layers as

$$\begin{cases} T_1^s = E_s S_1^s \\ T_1^p = E_p\left(S_1^p + d_{31}E_3\right) \end{cases} \tag{A2.2}$$

Where T_1^S and T_1^P represent respectively the stress in the structure and the PZT. S_1^S and S_1^P are respectively the strain in the structure and the PZT, E_S et E_P the Young modulus of the structure and the PZT ; $d_{31}=-190.0\times10^{-12}$ m/V, the piezoelectric constant. s and p for structure and PZT respectively. 1 and 3 for x and y axis (where 1 is the direction of axial strain and 3 is the direction of polarization) respectively and E_3 is the electrical field in the PZT du to the generated voltage.

With Eq. (A2.2), constitutive relation can be writing as:

$$T_1 = T_1^s + T_1^P = ES_1^s + E_p\left(S_1^p + d_{31}E_3\right) \tag{A2.3}$$

With T_1 the sum of stress in the structure and the PZT

By definition, the forces resulting from bending or moments of stresses $M(X,t)$ are written:

$$M(X,t)=\int_{ha}^{hb}T_1^s\,ydy+\int_{hb}^{hc}T_1^p\,ydy \tag{A2.4}$$

Where b is the width of the beam, h_a is the position of the bottom of the substructure layer from the neutral axis, h_b is the position of the bottom of the PZT layer therefore, top of the substructure layer from the neutral axis, and h_c is the position of the top of the PZT layer from

the neutral axis (see fig 2.1). Expression the bending strain in terms of radius of curvature [161] we have:

$$M(X,t) = -\int_{ha}^{hb} E_S \frac{\partial^2 w}{\partial X^2} y^2 dy - \int_{hb}^{hc} E_P \frac{\partial^2 w}{\partial X^2} y^2 dy + \int_{hb}^{hc} v(t) E_P \frac{d_{31}}{h_p} y dy \qquad \text{(A2.5)}$$

where the uniform electric field as a function of voltage $v(t)$ across the piezoelectric element and the thickness h_p is defined by the relation($E_3(t) = -v(t)/h_p$).
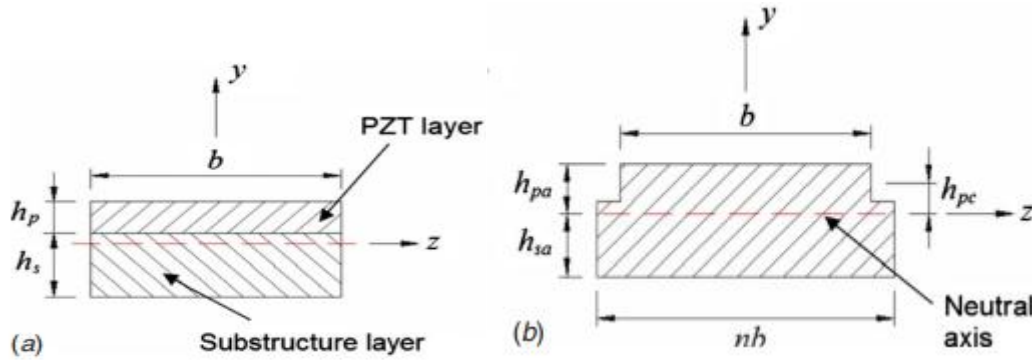
Figure 2.1: Cross section transformed

The goal here is to transform the cross section of the PZT assembly and the substructure (Figure 2.1(a)) to obtain a common cross section for both (Figure 2.1(b)). The transformed cross section depends only on the ratio of the two Young modules, namely $n = \dfrac{E_S}{E_P}$. The new section will be larger than the first if $E_S \succ E_P$ and smaller for $E_S \prec E_P$.

In the specific case of this work, the transformed section increases because $E_S \succ E_P$. Once this Young's modulus ratio has been made, we multiply it to the width of the old section, hence the width of the new section defined by $n \times b$ as observed in Figure 2.1. We thus obtain the following expressions for three different heights appearing in Figure 15:

$$h_{pa} = \frac{h_p^2 + 2nh_p h_s + nh_s^2}{2(h_p + nh_s)} \; ; h_{sa} = \frac{h_p^2 + 2h_p h_s + nh_s^2}{2(h_p + nh_s)} \; ; \; h_{pc} = \frac{nh_s(h_p + nh_s)}{2(h_p + nh_s)}$$

This allows us to give the expressions of the different heights appearing in Eq. 3.30 in the form:

$h_a = -h_{sa}$; (which is always negative)

$h_b = h_{pa} - h_p$; (which positive or negative)

$h_c = h_{pa}$; (which is always positive)

Where h_a is the distance from the bottom of the position of the substructure to the neutral axis.

h_b is the distance from the bottom of the position of the piezoelectric element (therefore from the top of the substructure) to the neutral axis.

h_c is the distance from the top of the piezoelectric element to the neutral axis. By evaluating Eq. 4, we obtain the expression of the moment in the form (A2.6)

$$M(X,t) = E'I \frac{\partial^2 w}{\partial X^2} + \vartheta v(t) \tag{A2.6}$$

Where $E'I = -\left(\dfrac{E_S \left(h_b^3 - h_a^3\right) + E_p \left(h_c^3 - h_b^3\right)}{3} \right)$ and $\vartheta = -\dfrac{E_p d_{31}}{2h_p}\left(h_c^2 - h_b^2\right)$

Considering that the electrodes and the piezoelectric element completely cover the lower surface of the beam, it is necessary to rewrite Eq. A2.6 as follows:

$$M(X,t) = E'I \frac{\partial^2 w}{\partial X^2} + \vartheta v(t)\left[H(X) - H(X-a)\right] \tag{A2.7}$$

Where $H(\bullet)$ is the Heaviside function. We have

$$\rho_{total} b \frac{\partial^2 w}{\partial t^2} + \lambda \frac{\partial w}{\partial t} + E'I \frac{\partial^4 w}{\partial X^4} = -\vartheta \left(\frac{d\delta(X)}{dX} - \frac{d\delta(X-a)}{dX} \right) v(t) \tag{A2.8}$$

With the following boundary conditions:

$$w(0,t) = 0, \frac{\partial w}{\partial X}(0,t) = 0, \frac{\partial^2 w}{\partial X^2}(L,t) = 0, \frac{\partial^3 w}{\partial X^3}(L,t) = 0 \tag{A2.9}$$

Eq. (A2.8) is the equation of the mechanical part with the piezoelectric coupling.

In order to establish the equation of the electrical part, we consider the following constitutive equations

$$D_3 = d_{31}T_1 + \varepsilon_{33}^T E_3 \tag{A2.10}$$

Where D_3 is the electric displacement and $\varepsilon_{33}^T = 15.93 \times 10^{-9}$ F/m the permittivity at constant stress. If we rearrange Eq. (A2.2) to express the stress T_1 depending on the deformation S_1 and the Young's modulus of the piezoelectric element E_p, and by reporting in Eq. (A2.10), the component of the permittivity becomes $\varepsilon_{33}^S = \varepsilon_{33}^T - d_{31}^2 E_3$ [162]. After replacing the electric field as a function of the voltage across the piezoelectric element and the thickness h_p of the piezoelectric element, we get:

$$D_3 = d_{31}E_p S_1 - \varepsilon_{33}^S \frac{v(t)}{h_p} \tag{A2.11}$$

The deformation S_1 of the piezoelectric element can be expressed as a function of the distance h_{pc} between the center of the piezoelectric element (according to the thickness) and the neutral axis of the beam according to the cross section modified to the expression:

$$S_1(X,t) = -h_{pc}\frac{\partial^2 w}{\partial X^2} \tag{A2.12}$$

Therefore Eq. (A2.12) becomes:

$$D_3 = -d_{31}E_p h_{pc}\frac{\partial^2 w}{\partial X^2} - \varepsilon_{33}^S \frac{v(t)}{h_p} \tag{A2.13}$$

Where ε_{33}^S la permittivity at the constant stress and h_p thickness of PZT. Note that $v(t)$ is the voltage generated by the PZT.

If we call E_0, the total electric field in the piezoelectric plate, then it is linked to the electric displacement by the relation $D_3 = \varepsilon_0 E_0$ where ε_0 represents the permittivity of the vacuum. However, if we apply a voltage $V(t)$ across the PZT, knowing that $E_0 = \dfrac{V(t)}{h_p}$, the relation (A3.13) becomes:

$$D_3 = \varepsilon_0 \frac{U(t)}{h_p} \tag{A2.14}$$

By equalizing Eq. (A2.13) and Eq. (A2.14), we obtain

$$-d_{31}E_p h_{pc}\frac{\partial^2 w}{\partial X^2} - \varepsilon_{33}^S \frac{v(t)}{h_p} = \varepsilon_0 \frac{U(t)}{h_p} \tag{A2.15}$$

Having a load resistance R in series with the PZT, a coil, a nonlinear capacitor and the external source $U(t)$, this amounts to writing Eq. (A2.15) as follows:

$$L\frac{di}{dt} + Ri + V_C(q) - \frac{\varepsilon_{33}^S}{\varepsilon_0}v(t) - \frac{d_{31}E_p h_{pc}h_p}{\varepsilon_0}\frac{\partial^2 w}{\partial X^2} = u_0 \sin\omega t \tag{A2.16}$$

where $V_C(q) = \alpha q + \beta q^3$ the voltage through the nonlinear capacitor, and α, β the positive parameter.The PZT being in series with the electrical components, we can write,

$i(t) = \dfrac{dq}{dt} = -C_p \dfrac{dv(t)}{dt}$ where $C_p = \dfrac{\varepsilon_{33}^S bl}{h_p}$, the capacitor of the PZT element.

Bibliography

[1]   G.H. Gautschi, Piezoelectric Sensorics: Force, Strain, Pressure, Acceleration and Acoustic Emission Sensors, Materials and Amplifiers, pringer, (2002).

[2]   J. Curie, P. Curie Development, via compression, of electric polarization in hemihedral crystals with inclined faces, Bulletin de la Société Minérologique de France. (3), 90–93, (1880).

[3]   D.A. Skoog, F.J. Holler, and S.R. Crouch, Principles of Instrumental Analysis, 6th edition, Brooks and Cole, (2006).

[4]   *G*. Lippmann, Principle of the conservation of electricity. (24): 145. *Archived* from the original on 2016-02-08, (1881).

[5]   V. Woldemar Lehrbuch der Kristallphysik. Berlin: B. G. Teubner. Archived from the original on 2014-04-21, (1910).

[6]   M. V. Tchakui and P. Woafo, Dynamics of three unidirectionally coupled autonomous Duffing oscillators and application to inchworm piezoelectric motors: Effects of the coupling coefficient and delay, Chaos (26), 113108, (2016).

[7]   K. Jamroziak, M. Kosobudzki, Determining the torsional natural frequency of underframe of off-road vehicle with use of the procedure of operational modal analysis, Journal of Vibro engineering,(14), 472-476, (2012).

[8]   A. Buchacz, A Wróbel, Modelling and study of the piezoelectric effect influence on the characteristics of mechatronic systems, Silesian University of Technology Publishing House, Gliwice, (in Polish), (2010).

[9]   E. Rusinski, S. Dragan, P. Moczko, D. Pietrusiak, Implementation of experimental method of determining modal characteristics of surface mining machinery in the modernization of the excavating unit, archives of civil and mechanical engineering, 471-476, (2012).

[10]   C. H. Park,on the circuit model of piezoceramics, Journal of Intelligent Material Systems and Structures, (12), 7, 515–522, (2001).

[11]   J. Kim, B. L. Grisso, J. K. Kim, D. S. Ha, and D. J. Inman,Electrical modeling of piezoelectric ceramics for analysis and evaluation of sensory systems, in Sensors Applications Symposium, SAS. IEEE. IET, 122–127, (2008).

[12]   S. Sherrit, H. D. Wiederick, B. K. Mukherjee and M. Sayer, An accurate equivalent circuit for the unloaded piezoelectric vibrator in the thickness mode,J.Phys.D: AppliedPhysics 30(16), 2354-2363, (1997).

[13]   X. Liu, Y. Civet, Y. Perriard, Equivalent piezoelectric actuator circuits and comparison, in

IEEE/ASME, Int. Conf. on Advanced Intelligent Mechatronics (AIM), Besançon, France, July 8-11, (2014).

[14] B. Nogarede, C.Henaux, J. F.Rouchon, F.Léonard: Matériaux électro-actifs et génie biomédical : étude d'une prothèse de la main actionnée par une motorisation piézoélectrique. France, MGE, Lille, (2000).

[15] D.N., Wild.: Neurosonology pioneers. Ultrasound Med Biol. (14), 541-561, (1988).

[16] H. M., Mansour, P.B., Myrdal, Younis U, et al.: Chapter 11: Pulmonary drug delivery. In: Hillery AM and Park K (eds) Drug Delivery: Fundamentals and Applications, 2nd ed. London: CRC Press/Taylor & Francis, Inc., pp. 249–277, (2016).

[17] S. K., De and N. R. Aluru,: Complex Oscillations and Chaos in Electrostatic Micro-electromechanical Systems under Super-harmonic Excitations, Phys. Rev. Lett., (94), 204101, (2005).

[18] J. F., Rhoads, S. W., Shaw and K. L., Turner: The Nonlinear Response of Resonant Microbeam Systems With Purely-Parametric Electrostatic Actuation. J. Micromech. Microeng., (16), 890–899, (2006).

[19] R. Ivatury, H. Sugerman J.: Chest radiograph or computed tomography in the intensive care unit. Crit. Care Med., (28), 3-9, (2000).

[20] D. Lichtenstein A.: Mise au point Echographie pleuro-pulmonaire, Lung ultrasound, Réanimation, (12), 19 – 29, (2003).

[21] F. H., Williams: The Roentgen rays in medicine and surgery. New York: Macmillan, (1901).

[22] G. N., Hounsfield: Computerized transverse axial scanning. Brit J Radiol, (46), 16– 22 (1973).

[23] H. T., Winer-Muram *et al*: Pneumonia and ARDS in patients receiving mechanical ventilation: diagnostic accuracy of chest radiography. Radiology, (188), 79–85, (1993).

[24] R. R., Ivatury, H. J. Sugerman: Chest radiograph or computed tomography in the intensive care unit. Crit. Care Med. (28), 3-9, (2000).

[25] A. Dénier: Les ultrasons, leur application au diagnostic. Presse Méd., (22), 7–8, (1946).

[26] J. J. Wild, J. M., Reid: Diagnostic use of ultrasound. Br J Phys Med., 248-257, (1956).

[27] I. Prigogine, R. Lefever: Symmetry breaking instabilities in dissipative systems-II. J Chem. Phys., (48), 695–700, (1968).

[28] H. A. Sodano, D.J. Inman, G. A. Park review of power harvesting from vibration using piezoelectric materials. Shock Vib Dig (36), 197–205, (2004).

[29] E. Lefeuvre, A. Badel, A. Benayad, L. Lebrun, C. Richard, D. Guyomar: A comparison

between several approaches of piezoelectric energy harvesting. J Phys IV (128), 177–186, (2005).

[30] S. R. Anton, H. A. Sodano A review of power harvesting using piezoelectric materials (2003–2006). Smart Mater Struct (16), R1–R21, (2007).

[31] S. P. Pellegrini, N. Tolou, M. Schenk, J.L. Herder Bistable vibration energy harvesters: a review journal of intelligent material systems and structures. J Intell Mater Syst Struct (24), 1303–1312, (2012).

[32] R. L. Harne, K. W. Wang., A review of the recent research on vibration energy harvesting via bistable systems. Smart Mater Struct (22), 023001, (2013).

[33] S. Roundy, P.K. Wright, J. , Rabaey,A study of low level vibra-tions as a power source for wireless sensor nodes. Com-put.Commun. (26),1131-1144, (2003).

[34] S. Roundy, On the eectiveness of vibration-based energy harvesting. J.Intell.Mater.Struct (16), 809-823, (2005).

[35] D.S. Clair, A.Bibo Sennakesavababu V R. A scalable concept for micro power generator using flow-induced self-excited oscillators.Appl. Phys. Lett. (96), 144103, (2010).

[36] A. Bibo, R. Masana, A. King, G.Li, M. Daqaq Electromag-netic ferrofluid-based energy harvester. Phys. Lett. A (376), 2163-2166, (2012).

[37] A. Erturk Piezoelectric energy harvesting for civil infrastructure system applications: Moving loads and surface strain fluctua-tions. Intel J. Mat. Syst. Str. (22), 1959-1973, (2011).

[38] A. Erturk , Vieira WGR, J.C. De Marqui, D.J Inman. On the energy harvesting potential of piezoaeroelastic systems. Appl. Phys. Lett. (96), 184103, (2010).

[39] M. Lallart , S. Pruvost, D. Guyomar Electrostatic energy harvest-ing enhancement using variable equivalent permittivity. Phys. Lett. A. (375), 3921-3924, (2011).

[40] B. Mann, N., Sims Energy harvesting from the nonlinear oscilla-tions of magnetic Levitation. J. Sound Vibration. (319), 515-530, (2009).

[41] S. Li, J.Yuan , H. Lipson, Ambient wind energy harvesting using cross-flow fluttering. J. Appl. Phys.(109), 026104, (2011).

[42] M. Jeff, E.D. Barry, L.R. Jeffrey, L.T. Kimberly. Exploiting nonlinearity to provide broadband energy harvesting ASME International conference in dynamic system and control, (2009).

[43] M. Tian-Wei, Hui Z, Ning-Shou X. A novel parametrically ex-cited non-linear energy harvester. Mech. Syst. Signal. Pr. (28), 323-332, (2012).

[44] C.A. Kitio Kwuimy, G.Litak, M.Borowiec, M.Nataraj, Performance of a piezoelectric energy harvester driven by air fow. Appl. Phys. Lett. 100(2), 024103-3, (2012).

[45] E. Halvorsen Fundamental issues in nonlinear wideband-vibration energy harvesting. Phys. Rev. (87), 042129 (1-6), (2013).

[46] L .Zuo,Pei-Sheng Zhang. Energy harvesting, ride comfort and road handling of regenerative vehicle suspensions. J. Vibrat. Acoustics (135), 011002 (1-8), (2013).

[47] S. McGarry , C.Knight . The potential for harvesting energy from the movement of

trees. Sensors (11), 9275-9299, (2011).

[48]   S. McGarry, C., Knight, Development and successful applica-tion of a tree movement energy harvesting device, to power a wireless sensor node. Sensors (12), 12110-12125, (2012).

[49]   C. N. Dueyou Buckjohn, M. Siewe Siewe, I. S. Mokem Fokou, C. Tchawoua and T. C. Kofane, Investigating bifurcations and chaos in magnetopiezoelastic vibrating energy harvesters using Melnikov theory, Phys. Scr.88015006 (9pp), (2013).

[50]   G. T. Oumbé Tékam, E. B. Tchawou Tchuisseu, C. A. Kitio Kwuimy, P. Woafo, Analysis of an electromechanical energy harvester system with geometric and ferroresonant nonlinearities, Nonlinear Dyn, (2013).

[51]   A. Erturk, J. Homann, D J. Inman A piezomagnetoelastic struc-ture for broadband vibration energy harvesting. Appl. Phys.Lett. (94), 254102, (2009).

[52]   S. C. Stanton, C. C. McGehee, BP., Mann Nonlinear dynamics for broadband energy harvesting: Investigation of a bistable piezoelectric inertial generator Physica D (239), 640-653, (2010).

[53]   F.Cottone, F. Gammaitoni, H. Vocca , M. Ferrari, V.Ferrari, Piezo-electric buckled beams for random vibration energy harvest-ing. Smart.Mater.Struct. 21,035021, (2012).

[54]   L. Van Blarigan, L. Danzl, L. Moehlis, A broadband vibrational energy harvester. Appl. Phys. Lett. (100), 253904, (2012).

[55]   E. B. Tchawou Tchuisseu and P. Woafo, Harvesting energy using a magnetic mass and a sliding behavior. Nonlinear Engineering, (2014).

[56]   A. Erturk and D. J. Inman, Broadband piezoelectric power generation on high-energy orbits of the bistable Duffing oscillator with electromechanical coupling. *J. Sound Vib.*, *330*, 2339, (2011).

[57]   E. Simiu, R. H. Scanlan, Wind affects on structures, Wiley, New York, (1986).

[58]   R.C., Battista, P. feil, Reduction of vortex-induced oscillations of Rio-Niteroi Bridge by dynamic control devices. Journal of Wind Engineering & Industrial Aerodynamics 84 (3), 273–288, (2000).

[59]   B.V.Der Pol, V.D. Mark, The heartbeat considered as a relaxation oscillation, and an electrical model of the heart Philos. Mag. (6),763-775, (1928).

[60]   D.W .Storti, R.H.Rand. Dynamics of two strongly coupled relax-ation oscillators, SIAM J. Appl. Math. (46), 56-67, (1986).

[61]   B. Braaksma, Grasman. Critical dynamics of the Bonhoeer van der Pol quation and its chaotic response to periodic stimula-tion. Physica D (68), 265-280, (1993).

[62]   K. V. Dyke, The piezo-electric resonator and its equivalent network, Proceedings of the Institute of Radio Engineers, (16),742–764, (1928).

[63]   W.P. Maaon, "An Electromechanical Representation of a Piezoelectric Crystal Used as a Transducer," Proc. IRE, (23), 1252-1263, (1935)

[64]   J.C. Maxwell, A Treatise on Electricity & MaQnetism, 3rd Ed., 1891; New York: Dover, See particularly pp. 228 and 431, (1954).

[65]   W. Thomson (Lord Kelvin), Baltimore Lectures on Molecular Dynamics and the Wave Theory of Light. London: Cambridge University Press. Lectures given at The Johns

Hopkins University, Baltimore, MD, See particularly Lect. I, Wed., Oct. 1 (pp.12-13), Lect. IX, Wed., Oct. 8 (pp.104-105), Lect. X, Thurs., Oct. 9 (pp. 118-119), (1884).

[66] R. D. Mindlin and M.G. Salvadori, "Analogies," in Handbook of Experimental Stress Analysis, (M. Hetenyi, ed.) New York: Wiley, Lect. XI, Fri., Oct. 10 (pp.126-129). Chap. 16, pp. 700-827, (1950).

[67] W.P. Mason, "Electrical and Mechanical Analogies," Bell System Tech. J., Vol. 20, 11o. 4, pp. 405-414, (1943).

[68] Oksasoglou A.andVavrim D.,IEEE Trans. Circuits Syst, 41, 669, (1994).

[69] Fotsin H., "Phénomènes cohérents et incohérents dans le microphone à condensateur et dans les circuits électroniques à Diode Varicap", Thèse de Doctorat de 3eme cycle, Laboratoire d'électronique, Université de Yaoundé I, Cameroun, (1999).

[70] J. C. Chedjou, P. Woafo and S. Domngang, Journal of Vibrations and Acoustics, (123), 170 (2001).

[71] J. C. Chedjou, "Etude de la dynamique régulière et chaotique du système couplé oscillateur de Van der Pol-Oscillateur de Duffing" Thèse de Doctorat de 3ème cycle, Laboratoire d'électronique, Université de Yaoundé I, Cameroun (1999).

[72] B. Nana *et al*: Dynamics of a RLC series circuit with hysteretic iron-core inductor, Chaos, Solitons and Fractals (106), 184–192, (2018).

[73] J. H. Chan *et al* Nonlinear transformed model for circuit simulation. IEEE Trans Computer-Aided Des. (4) 76–82, (1991)

[74] Y. Kouomou Chembo and P. Woafo, Stability and Chaos Control in Electrostatic Transducers Physica Scripta (62), 255, (2000).

[75] T. J. Royston and B. H. Houston, Modeling and measurement of nonlinear dynamic behavior in piezoelectric ceramics with application to 1-3 composites, Journal of the acoustical Society of America (104), 2814-2827, (1998).

[76] M. Zhao and B. Balachandran, Actuator nonlinearities in interior acoustics control, in in Procedings of the Smart Structures Conference, SPE, III, March (2000).

[77] J. Sirochi and I. Chopra, Fundamental behavior of piezoceramic sheet actuators, Journal of intelligent Material Systems and Structures (11), 47-61.

[78] J. E. Garcia *et al*, Nonlinear behavior in a piezoelectric resonator. A method of analysis, IEEE Transactions on Ultrasonics, Ferroelectrics, and Frequency Control (47), 921-928, (2000).

[79] Y.H. Zhou, H. S. Tzou: Active control of nonlinear piezo-electric circular shallow spherical shells. Int. J. Solids Struct. (37), 1663–1677, (2000).

[80]   D. Sun, L. Tong, D. Wang: An incremental algorithm for static shape control of smart structures with nonlin-ear piezoelectric actuators. Int. J. Solids Struct. (41), 2277–2292, (2004).

[81]   V. Wagner, U. Hagedorn, Piezo-beam systems sub-jected to weak electric field: Experiments and modeling of non-linearities. J. Sound Vib. (256), 861–872, (2002).

[82]   M.K. Samal *et al,* A finite element model for nonlinear bihaviour of piezoceramics under weak electric fields. Finite Elements Anal. Des. (41), 1464–1480, (2005).

[83]   D. A. Saravanos *et al*, Layerwise mechanics and finite element for the dynamic analysis of piezoelectric composite plates. Int. J. Solids Struct. (34), 359–378, (1997)

[84]   H.S. Tzou and C.I. Tseng, Distributed piezoelectric sen-sor/actuator design for dynamic measurement/control of distributed parameter systems: A piezoelectric finite ele-ment approach. J. Sound Vib. (138), 500–505, (1990).

[85]   S.Y. Wang *et al*: Dynamic stability analysis of finite element modeling of piezoelectric com-posite plates. Int. J. Solids Struct. (41), 745–764 (2004).

[86]   S. Y. Wang, A finite element model for the static and dy-namic analysis of a piezoelectric bimorph. Int. J. Solids Struct. (41), 4075–4096, (2004).

[87]   V.Y. Taffoti Yolong, P. Woafo, The complete synchronization condition in a network of piezoelectric micro-beams, Nonlinear Dynamics, (57), 261-274, (2009).

[88]   P. R. Nwagoum Tuwa and P. Woafo, "Suppression of the noise-induced effects in an electrostatic micro-plate using an adaptive back-stepping sliding mode control," International Society of Automation Transactions., (72), pp. 100–109, (2018).

[89]   E.M. Sekouri, *et al* Modeling of a circular plate with piezoelectric actuators. Mechatronics (14), 1007–1020, (2004).

[90]   L. H. Tang and Y. W. Yang, a nonlinear piezoelectric energy harvester with magnetic oscillator. Appl. Phys. Lett.(101), 094102, (2012).

[91]   K. Q. Fan, Z. F. Ming, C. H. Xu, and F. B. Chao, Flow aeroacoustic damping using coupled mechanical–electrical impedance in lined pipeline Chin. Phys. B (22), 104502, (2013).

[92]   Z. L. Wang and J. Song, Science Piezoelectric Nanogenerators Based on Zinc Oxide Nanowire Arrays, 312, 242, (2006).

[93]   G. Cheng, Z.-H. Lin, L. Lin, Z.-L. Du, and Z. L. Wang, pulsed nanogenerator with Huge instantaneous Output Power Density ACS Nano (7), 7383 (2013).

[94]   S. Priya, J., Advances in energy harvesting using low profile piezoelectric transducers

Electroceram, (19), 167, (2007).

[95]   W. J. Su and J. Zu, An innovative tri-directional broadband piezoelectric energy harvester Appl. Phys. Lett. (103), 203901, (2013).

[96]   S. X. Zhou, J. Y. Cao, A. Erturk, and J. Lin, Enhanced broadband piezoelectric energy harvesting using rotatable magnets Appl. Phys. Lett.(102), 173901, (2013).

[97]   I.-H. Kim, H.-J. Jung, B. M. Lee, and S.-J. Jang, Broadband energy-harvesting using a two degree-of-freedom vibrating body Appl. Phys. Lett.(98), 214102, (2011).

[98]   Y. Hu and Y. Xu, A wideband vibration energy harvester based on a folded asymmetric gapped cantilever Appl. Phys. Lett.(104), 053902, (2014).

[99]   K. Q. Fan, C. H. Xu, W. D. Wang, and Y. Fang, Broadband energy harvesting via magnetic coupling between two movable magnets Chin. Phys. B (23), 084501, (2014).

[100] A. Erturk, P. A. Tarazaga J. R. Farmer, and D. J. Inman, Effect of strain nodes and electrode configuration on piezoelectric energy harvesting from cantilevered beams Journal of Vibration and Acoustics, February, (131) 011010-1, (2009).

[101] S. C. Stanton, C. C. McGehee, and B. P., Nonlinear dynamics for broadband energy harvesting: Investigation of a bistable piezoelectric inertial generator Mann,Physica D (239), 640, (2010).

[102] W.J.Su,J.Zu,andY.Zhu, Design and development of a broadband magnet-induced dual-cantilever piezoelectric energy harvester J. Intell. Mater. Syst. Struct. (25), 430 (2014).

[103] F. Cottone, H. Vocca, and L. Gammaitoni, Nonlinear Energy Harvesting, PRL, Physical Review Letters (102), 080601, (2009).

[104] F. Kangqi, *et al*, A nonlinear piezoelectric energy harvester for various mechanical motions, Applied Physics Letters (106), 223902, (2015).

[105] S. Baglio, F. Maiorca and C. Trigona Sens. Actuators, A, (202), 176, (2013).

[106] A. Erturk, D. J. Inman, A distributed parameter ectromechanical model for cantilevered piezoelectric energy harvesters. J Sound Vib., 2008, (130) 041002-1, (2008).

[107] D. Barton, S.G.Burrow, L.R. Clare, Energy harvesting from vibrations with a nonlinear oscillator. J. Vib Acoust (132), 021009, (2010).

[108] J. Cao *et al* Chaos in the fractionally damped broadband piezoelectric energy generator. Nonlinear Dyn (80), 1705–1719, (2014).

[109] A. Syta *et al* Experimental analysis of the dynamic response of energy harvesting devices based on bistable laminated plates. Meccanica (50), 1961– 1970, (2015).

[110] M. Lallart *et al*, Coupling mechanical and electrical nonlinearities: The effect of synchronized discharging on tristable energy harvesters. Applied Energy, (266), 114516

(2020)

[111] B. K. Shravankumar and G. Anup, Geometrically Non-Linear Bending
Analysis of Piezoelectric Fiber-Reinforced Composite (MFC/AFC) Cross-Ply Plate Under
Hygrothermal Environment, Journal of Thermal Stresses, (36), 1255-1282, (2013).

[112] S.B. kerur and G.Anup, Active vibration control of composite plate using AFC
actuator & PVDF sensor, International Journal of Structural Stability and Dynamics Vol.
(11), 237255, (2011).

[113] R. Weber, Piezo Motor Based Medical Devices, Medical Design Technology, April (2009)

[114] S.B. kerur and G. Anup, Active control of geometrically Nonlinear transient
response of smart laminated plate integrated with AFC actuator & PVDF sensor,
Journal Of Intelligent Material Systems And Structures, (22) —July 2011.

[115] S.B. kerur and G. Anup, Active vibration control of composite plate using AFC
actuator and PVDF sensor, (2011).

[116] K. Khordishi, Active vibration control of circular plate coupled with piezoelectric layers
excited by plane sound wave, (2014).

[117] Z. Gao, Active Monitoring and vibration control of smart structure aircraft base on
FBG sensor and PZT actuator, (2016).

[118] H. Sharavari Active Vibration control of smart structure using PZT patches,2013.

[119] S.B. kerur and G. Anup, Active vibration control of composite plate using AFC actuator
and PVDF sensor, (2011).

[120] B.R. Nana Nbendjo and P. Woafo, Active control with delay of horseshoes chaos
using piezoelectric absorber on a buckled beam under parametric excitation, Chaos,
Solitons and Fractals (32), 73–79, (2007).

[121] B.R. Nana Nbendjo, Amplitude control on hinged–hinged beam using piezoelectric
absorber: Analytical and numerical explanation, International Journal of Non-Linear
Mechanics (44), 704–708, (2009).

[122] V. Vidur Gundage and P. R. Sonawane, Active Vibration Control of Cantilever Beam
Using Piezoelectric Patches, (2006).

[123] B. Fabio Botta *et al* Optimal Placement of Piezoelectric Plates to Control Multimode
Vibrations of a Beam, (2013).

[124] S. K., De and N. R. Aluru: Complex Oscillations and Chaos in Electrostatic
Microelectromechanical Systems Under Superharmonic Excitations, Phys. Rev. Lett.,
(94) 204101 (2005).

[125] J. F. Rhoads, S. W. Shaw, and K. L. Turner: The Nonlinear Response Resonant

Microbeam Systems With Purely-Parametric Electrostatic Actuation. J. Micromech. Microeng. (16), 890–899, (2006).

[126] P. R. Nwagoum Tuwa and P. Woafo, "Micro-Plate Piezoelectric Energy Harvester for Pulsating Arterial Pressure," J. Mech. Med. Biol., (16) , p. 1650073, (2016).

[127] E.J. Routh, A treatise on the stability of a given state of motion: particularly steady motion, (1877).

[128] A. Hurwitz, On the condition under which an equation has only roots with negative real parts, (65), (1895).

[129] M.L. Saunders and G. Birkho, Algebra (3rd ed.), American Mathematical So-ciety., (626), (1999).

[130] N. J. Kasdin, "Runge-Kutta Algorithm for the Numerical Integration of Stochastic Differential Equations," J. Guid. Control. Dyn., (18), pp. 114–120, Jan. (1995).

[131] G. Teschl, "Ordinary differential equations and dynamical systems," Baylor.Edu, (140), (2012).

[132] M. Conti and C. Turchetti, "Approximate identity neural networks for analog synthesis of nonlinear dynamical systems," IEEE Trans. Circuits Syst. I Fundam. Theory Appl., (41), 841–858, (1994)

[133] P. Shivashankar, S.B. Kandagal, Characterization of elastic and electromechanical nonlinearities piezoceramic plate actuators from vibrations of a piezoelectric beam, Mech. Syst. Signal Process, (116), 624–640, (2019).

[134] L. Graney and A. A. Richardson, "The numerical solution of nonlinear partial differential equations by the method of lines," *J. Comput. Appl. Math.*, (7), 229–236, (1981).

[135] B. P. Ndemanou, J. Metsebo, B. R. N. Nbendjo, and P. Woafo, "Dynamics and magneto-rheological control of vibration of cantilever Timoshenko beam under earthquake loads," *Nonlinear Dyn.*, (78), 163–171, (2014).

[136] O. Mass, T. Order, and S. Schemes, Numerical methods for partial differential equations, (33), New York, NY: Academic Press, (1977).

[137] W. F. Ames, Numerical Methods for Partial Differential Equations. Academic Press, (1992).

[138] G.B. Mbou Soh, Y.J. Monkam, P.R. Nwagoum Tuwa, R. Tchitnga and P. Woafo Study of a piezoelectric plate based self-sustained electric and electromechanical oscillator, Mechanics Research Communications (105). 103504, (2020).

[139] T. K. Caughey, and M. E. J. O'Kelly, Classical Normal Modes in Damped Linear Dynamic Systems. ASME J. Appl. Mech., (3), 583–588, (1965)

[140] C. A. Kitio Kwuimy and P. Woafo : Dynamics, chaos and synchronization of self-sustained electromechanical systems with clamped-free flexible arm, *Nonlin . Dyn . (*53), 201–213, (2007).

[141] S. D. Senturia, N. Asuru, J. White, Simulating the behavior of MEMS devices, Computational methods and needs, *I EEE Comput. S ci. En gn. g.*, (4), 30–43, (1997)

[142] P. R. Nwagoum Tuwa and P. Woafo, "Suppression of the noise-induced effects in an electrostatic micro-plate using an adaptive back-stepping sliding mode control," International Society of Automation Transactions., (72), 100–109, 2018.

[143] B. Nana *et al*, Dynamics of a RLC series circuit with hysteretic iron-core inductor, Chaos, Solitons and Fractals (106), 184–192, (2018)

[144] J. H. Chan *et al,* Nonlinear transformer model for circuit simulation. IEEE Trans Computer-Aided Des. (4), 76–82, (1991)

[145] J. M. Ottino, F. J. Muzzio, M. Tjahjadi, Chaos, symmetry and self-similarity: exploiting order and disorder in mixing processes. Science, (257); 754-760, (1992)

[146] Zhe L.: Chaotic vibration mixing. Mech. Mach. Theory, (30), 613-618, (1995)

[147] K. T. Chau, S. Ye, Y. Gao, Application of chaotic motion motors to industrial mixing processes, in IEEE-1A, 1874-1880, (2004)

[148] D. A. Sarti and W. F. Sample, Diagnostic Ultrasound: text and cases. Springer, Dordrecht, (2012)

[149] D. U. Simo , T. L. Abobda and P. Woafo, Dynamical Behavior of a Capacitive Microelectromechanical System Powered by a Hindmarsh–Rose Electronic Oscillator. J. Comp. Nonl. Dyn., (11), 1-7, (2016)

[150] S. R. Thepi D. U. Simo and P. Woafo, Generation of pulse-like and bursting-like oscillations from nonlinear systems using embedded technologies and applications to excite mechanical arms. Commun Nonlinear Sci., (69), 343–359, (2019)

[151] Hindmarsh J.L., Rose R.M.: A model of neuronal bursting using three coupled first order differential equations. Proc. R. So. Lond. Ser. B., (221), 87–102, (1984)

[152] Saddik G.: Ultrasound Imaging System. University of California, Los Angeles (UCLA), CA Department of Bioengineering. (63), Accessed February,(2016).

[153] S. Roundy, On the ectiveness of vibration-based energy harvesting. J. Intell. Mater. Struct, (16), 809-823, (2005).

[154] A. H., Nayfeh and D.T. Mook, Nonlinear Oscillations Wiley, New York, (1979).

[155] C. A. Kitio Kwuimy, B. R. Nana Nbendjo and P. Woafo, "Optimization of Electromechanical Control of Beam Dynamics: Analytical Method and Finite Differences

Simulation," Journal of Sound and Vibration, (298), 180-193, (2006).

[156] M. Siewe Siewe, bifurcations and chaos in self -excited systems with three -w ell potential oscillator, Laboratory of Mechanics, Faculty of Science, University of Yaounde I, Ph. D Thesis, (2006).

[157] W. Szemplin, ska-Stupnicka, Rudowski J.; Neimark. Bifurcation, almost- periodicity and chaos in the forced Van der Pol–Duffing system in the neighbourhood of the principal resonance, Physics Letters A, (192), 201–206, (1994).

[158] A. Venkatesan, M. Lakshamanan, Bifurcation and chaos in the double-well Duffing–Van der Pol oscillator: numerical and analytical studies, Physical Review E (56), 6321–6330, (1997)

[159] A., Erturk, and D. J., Inman, "An Experimentally Validated Bimorph Cantilever Model for Piezoelectric Energy Harvesting From Base Excitations," Smart Mater. Struct., in review, (2008)

[160] R.D. Gabbai, BenaroyaH. An overview of modeling and experiments of vortex-induced vibration of circular cylinders *J. Sound Vib.*, (282), 575616, (2005).

[161] S. Timoshenko, and D. H. Young, Elements of Strength of Materials, Van Nostrand Reinhold, New York, (1968).

[162] IEEE Standard on Piezoelectricity, IEEE, New York, (1987).

List of publications

1- G.B. Mbou Soh, Y.J. Monkam, P.R. Nwagoum Tuwa, R. Tchitnga and P. Woafo Study of a piezoelectric plate based self-sustained electric and electromechanical oscillator, Mechanics Research Communications (105), 103504, (2020).